THESIS

INTEGRATION OF AN UNMANNED AIRCRAFT SYSTEM AND GROUND-BASED REMOTE SENSING TO ESTIMATE SPATIALLY DISTRIBUTED CROP EVAPOTRANSPIRATION AND SOIL WATER DEFICIT THROUGHOUT THE VEGETATION SOIL ROOT ZONE

Submitted by

Jeffrey Calvin Hathaway

Department of Civil and Environmental Engineering

In partial fulfilment of the requirements

For the Degree of Master of Science

Colorado State University

Fort Collins, Colorado

Spring 2016

Master’s Committee:

Advisor: José L. Chávez

Jeffrey D. Niemann
Anura P. Jayasumana
Huihui Zhang

ABSTRACT

INTEGRATION OF AN UNMANNED AIRCRAFT SYSTEM AND GROUND-BASED REMOTE SENSING TO ESTIMATE SPATIALLY DISTRIBUTED CROP EVAPOTRANSPIRATION AND SOIL WATER DEFICIT THROUGHOUT THE VEGETATION SOIL ROOT ZONE

Irrigation is the largest consumer of fresh water and produces over 40% of the world's food and fiber supply. As the world's population continues to grow rapidly, the increased demands on fresh water will force the agricultural community to improve the efficiency and productivity of irrigation systems, while reducing overall water usage. In order to address the requirements of increased efficiency and productivity in agricultural water use, the agricultural community has begun to focus on the development of precision agriculture (PA) irrigation management systems for use with irrigated agriculture. Remote sensing (RS) is at the forefront of the PA movement, allowing the estimation of spatially distributed crop water requirements on a large-scale basis. Techniques using ground, aerial and space-borne RS platforms have been developed to estimate actual crop evapotranspiration (ET_a) and soil water deficit (SWD) for use in PA irrigation management systems. The ability to monitor the ET_a and SWD allows irrigators to manage their irrigation to increase efficiency and decrease overall water use while maintaining crop yields goals. Historically, remote sensing data, such as spectral reflectance and thermal infrared (TIR) imagery, were provided by ground or space-borne RS platforms, like NASA's Landsat 8 satellites. Though these methods are effective at estimating ET_a over large areas, their lack of spatial and temporal resolution limit their effectiveness for application in PA irrigation management systems. In order to address the required spatial and temporal resolutions required for PA systems, Colorado State University (CSU) developed an unmanned aircraft system (UAS) RS platform capable of collecting high spatial and temporal resolution data in the TIR, near-infrared (NIR), red and green bands of the electromagnetic spectrum. During the summer of 2015, CSU conducted four flights over corn at the Agriculture Research Development and Education Center (ARDEC), near Fort Collins, CO, with the Tempest UAS RS platform in order to collect thermal and multispectral imagery. The RS data collected over the ARDEC test location were used in three studies. The first was the comparison of the raw RS data to the ground-based RS data collected during the RS overpasses. The second study used the Tempest RS data to estimate the ET_a using four methods: two methods based on the surface energy balance (Two-Source Energy Balance (TSEB) and the Surface Aerodynamic Temperature (SAT)), one method based on the TIR imagery (Crop Water Stress Index (CWSI)), and one method based on the spectral reflectance imagery (reflectance-based crop coefficients (k_{cbrf})) and reference ET. Remote sensing derived ET_a estimates were compared to ET_a derived using neutron probe soil moisture sensors. The third study utilized the RS derived ET_a and the Hybrid Soil Water Balance method to estimate the SWD for comparison with the neutron probe derived SWD. Results showed that the Tempest RS data was in good agreement with the ground-based data as demonstrate by the low RMSE of the raw data, ET_a and SWD calculations (TIR = 5.68 ^oC, NIR = 5.26 % reflectance, red = 3.51 % reflectance, green = 7.31 % reflectance, TSEB ET_a = 0.89 mm/d, Hybrid SWD = 16.19 mm/m). The accuracy of the results of the Tempest UAS RS platform suggests that UAS RS platforms have the potential to increase the accuracy of ET_a and SWD estimation for use in the application of a PA irrigation management system.

ACKNOWLEDGEMENTS

Funding for this study was provided by the Colorado Water Conservation Board - Colorado Water Institute, Borland Hydrology Fund (CEE Department), Colorado Agricultural Experiment Station and Colorado State University Extension, and the USDA Natural Resources Conservation Agency – Conservation and Innovation Grants. Additionally, the United States Army provided funding for my tuition.

I would like to thank my advisor, Dr. José L. Chávez, for allowing me the opportunity to participate on his research team. Drs. Jeffrey Niemann, Anura Jayasumana and Huihui Zhang for agreeing to be my committee members. The staff at ARDEC, Mark Collins and Christopher Fryrear for their patients, assistance and technical expertise.

My loving wife, Courtney, I could not have done it without you. My children, Cooper and Ella for having the patients and understanding to allow me to complete my studies, and the ability make the best of situations.

TABLE OF CONTENTS

LIST OF TABLES

CHAPTER 1

CHAPTER 2

CHAPTER 3

APPENDIX 1

APPENDIX 4

LIST OF FIGURES

CHAPTER 1

CHAPTER 2

CHAPTER 3

APPENDIX 1

APPENDIX 2

APPENDIX 3

APPENDIX 4

LIST OF ACRONYMS AND SYMBOLS

AD	Analysis and Decision Making Process
ARDEC	Agricultural Research and Development and Education Center
ASCE-EWRI ET_{ref}	American Society of Civil Engineers Environmental and Water Resources Standardized Evapotranspiration
ASTER	Advance Space-borne Thermal and Reflections Radiometer
AVHRR	Advanced Very High Resolution Radiometer
AVRC	Arkansas Valley Research Center
CEE	Department of Civil and Environmental Engineering
CFR	Code of Federal Regulations
COA	Certificate of Approval or Waiver
COAGMET	Colorado Agricultural Meteorological Network
CP	Center Pivot Pressurized Sprinkler System
Cp_a	Specific Heat of Dry Air (J kg^{-1} K^{-1})
CSU	Colorado State University
CWSI	Crop Water Stress Index
d	Zero-plane Displacement Height (m)
D_i	Soil Water Deficit at the end of Day i (mm)
D_{i-1}	Soil Water Deficit at the end of Day i-1 (mm)
DP	Deep Percolation (mm)
D_r	Root Zone Depletion (mm)
e_a	Actual Vapor Pressure (kPa)
EF	Evaporative Fraction
e_s	Saturation Vapor Pressure (kPa)
ET	Evapotranspiration (mm h^{-1} or mm d^{-1})
ET_a	Actual Crop Evapotranspiration (mm h^{-1} or mm d^{-1})
ET_p	Potential Crop Evapotranspiration (mm h^{-1} or mm d^{-1})
ET_rF	Reference ET Fraction
FAA	Federal Aviation Administration
FAO	Food and Agriculture Organization of the United Nations
f_c	Vegetation Fractional Cover
f_g	Fraction of Vegetation that is Green
G	Soil Heat Flux (W m^{-2})
GIS	Geographic Information System
GPS	Global Positioning System
GW	Ground Water Capillary Rise (mm)
H	Sensible Heat Flux (W m^{-2})
H_c	Canopy Sensible Heat Flux (W m^{-2})
H_s	Soil Sensible Heat Flux (W m^{-2})
H_t	Total Sensible Heat Flux (W m^{-2})
Hybrid	Hybrid SWD Method
I_n	Net Irrigation (mm)
k	Von Karman Constant

k_c	Crop Coefficients
$k_{c\,max}$	Maximum Value of k_c
k_{cb}	Basal Crop Coefficient
K_{cbrf}	Reflectance-based Crop Coefficients
k_e	Soil Evaporative Coefficient
k_r	Evaporative Reduction Coefficient
k_s	Stress Coefficient
LAI	Leaf Area Index
LE	Latent Heat Flux (W m^{-2})
LE_c	Canopy Latent Heat Flux (W m^{-2})
LE_s	Soil Latent Heat Flux (W m^{-2})
LE_t	Total Latent Heat Flux (W m^{-2})
LIRF	Limited Irrigation Research Facility
LM	Linear move pressurized Sprinkler System
L_{mo}	Monin-Obukhov Atmospheric Stability Length Scale (m)
LOE	Line of Effort
MBE	Mean Bias Error
METRIC	Mapping Evapotranspiration at High Resolution with Internal Calibration
MODIS	Moderate Resolution Imaging Spectroradiometer
NAS	National Airspace
NASA	National Aeronautics and Space Administration
NDVI	Normalized Difference Vegetation Index
NIR	Near-Infrared
NOAA	National Oceanic and Atmospheric Administration
NP	Neutron Probe Soil Moisture Sensor
NWCG	Northern Water Community Gardens
OSAVI	Optimized Soil Adjusted Vegetation Index
	PA Precision Agriculture
P_n	Net Precipitation (mm)
R/C	Radio Controlled
r_{ah}	Aerodynamic Resistance to Heat Transfer (s m^{-1})
RAW	Readily Available Water (mm/m)
RMSE	Root Mean Square Error
R_n	Net Radiation (W m^{-2})
R_{n_c}	Net Radiation of the Canopy (W m^{-2})
R_{n_s}	Net Radiation of the Soil (W m^{-2})
r_s	Resistance to Heat Flow just above the Soil (s m^{-1})
R_s	Incoming Short Wave Radiation (W m^{-2})
RS	Remote Sensing
RTK	Real Time Kinematic
R_z	Root Zone (m)
SAT	Surface Aerodynamic Temperature
SEB	Surface Energy Balance
SEBAL	Surface Energy Balance for Land
SRO	Surface Run Off (mm)
SS-VRI	Site Specific Variable Rate Irrigation

SWB	Soil Water Balance
SWC	Soil Water Content (mm)
SWD	Soil Water Deficit (mm)
SWS	Soil Water Sensors
T	Student T-Test
T_a	Air Temperature (^oC)
TAW	Total Available Water (mm)
T_c	Canopy Temperature (^oC)
TIR	Thermal Infrared
T_o	Surface Aerodynamic Temperature (^oC)
T_s	Soil Temperature (^oC)
TSEB	Two-Source Energy Balance
T_{SFC}	Radiometric Surface Temperature (^oC)
u	Wind Speed (m s^{-1})
u_*	Friction Velocity (m s^{-1})
u_2	Wind Speed at 2 m (m s^{-1})
UAS	Unmanned Aircraft System
USU	Utah State University
VI	Vegetation Index
VIS	Visible Spectrum
VPD	Vapor Pressure Difference
VPG	Vapor Pressure Gradient
Z_m	Height of the Wind Speed Measurement (m)
Z_{oh}	Roughness Length for Heat Transfer (m)
A	Surface Albedo
α_t	Significant Level of T-Test
γ	Psychrometric Constant (kPa $^oC^{-1}$)
Δ	Slope of the Saturation Vapor Pressure – Temperature Relationship (kPa $^oC^{-1}$)
ε_a	Emissivity of the Air
ε_s	Emissivity of the Surface
Θ_{FC}	Volumetric Soil Water Content at Field Capacity (mm m^{-1})
Θi	Volumetric Soil Water Content at time i (mm m^{-1})
Θ_{WP}	Volumetric Soil Water Content at Field Wilting Point (mm m^{-1})
λ_v	Latent Heat of Vaporization (J kg^{-1})
ρ_a	Density of the Air (kg m^{-3})
ρ_w	Density of Water (kg m^{-3})
σ	Stefan-Boltzmann Constant (W m^{-2} K^{-4})
ψ_h	Stability Correction Factor for Atmospheric Heat Transfer
Ω	Clumping Factor

CHAPTER 1: INTRODUCTION

1.1. Water Requirements – Overview

The world's fresh water supply is a limited natural resource that is at the center of competition between agricultural, domestic, industrial, recreational and environmental demands. At the end of 2015, the world's population was approximately 7.3 billion people with an estimated growth rate of 1.18% annually (United Nations, 2015). By 2025, industrial and domestic consumption will increase by 150% and 180% respectively (Shiklomanov, 1993). The water demand caused by the global population growth is compounded by the ever-decreasing ground water availability and water quality, increasing environmental regulations, degradation of agricultural land associated with poor management practices, and domestic and industrial development (Evans et al., 2013).

In addition to the increase in global fresh water demands, changing global weather patterns associated with climate change have the capability to decrease the overall water availability through changing precipitation patterns, increased surface temperatures and long-term droughts (Walthall et al., 2012). In order to meet the increasing agricultural demand, as well as the rapidly increasing non-agricultural consumption, the agricultural community is under pressure to develop and implement irrigation systems, and crop water requirement estimation technology that increase production, while decreasing overall land and water use (Evans et al., 2013).

1.2. Irrigation Requirements

Irrigation is the world’s largest consumer of fresh water, accounting for 67% of the total freshwater withdrawal and 86% of consumptive use (UNEP, 2008). By 2025, using current practices, agricultural water use will increase by 130% (Shiklomanov, 1993). Currently, approximately 17% of the worlds cultivated farmland is irrigated. That irrigated land un-proportionally produces 40% of the world’s food and fiber supply [Postel, 1999]. As the demand on fresh water and agricultural land continues to rapidly increase, the percentage of irrigated farmland must increase, as well as the efficiency and productivity of the irrigation technology and systems [Postel 1999; Evans et al., 2013]. Irrigation will continue, even grow in importance, to be a critical aspect of the global agricultural system. In order to address the requirements of increased efficiency and productivity in agriculture water use, the agricultural community has begun to focus on the development of Precision Agriculture (PA) systems for use with irrigated agriculture.

1.3. Precision Agriculture (PA)

Precision Agriculture, as defined by the United States Department of Agriculture (USDA), Natural Resources Conservations Service (NRCS) is:

> “A management system that is information and technology based, is site specific and uses one or more of the following sources of data: soils, crops, nutrients, pest, moisture or yield for optimum profitability, sustainability and protection of the environment [McLoud et al., 2007].”

The overall goal of PA is the optimization of inputs for agricultural production according to the capability of the land and available resources. This means using a systematic approach to develop an agricultural system that optimizes output, i.e. efficiency and productivity, by taking into account the physical, social, environmental and economic aspects of the overall system [McLoud et al., 2007].

Five basic components make up a PA system: Background data, a record keeping system, analysis and decision (AD) making process, required equipment, and an evaluation and revision process [McLoud et al., 2007].

Background data consists of geo-referenced, spatially distributed data about the agricultural location. These data include information about soil properties, water table location, water quality and historical environmental conditions [McLoud et al., 2007].

The record keeping systems consist of a well-organized record of all actions, both natural and man-made, that affect the agricultural system, such as precipitation, applied irrigation and agro-chemicals. Keeping a soil water balance for a growing season is an example of the required record keeping associated with a PA system. The record keeping system is important to the overall PA system because records become background data for future system development [McLoud et al., 2007].

The analysis and decision making process is the critical step in PA. The first duty of the AD process is data collection through remote sensing (RS) or physical measurements. Examples of the types of data are multispectral imagery from RS platforms and root zone soil water content (SWC) derived from soil water sensors (SWS). The purpose of data analysis is to provide inputs, such as SWD and crop water stress, to the decision making process [McLoud et al., 2007]. The decision making process, taking into account all of the inputs and factors, determines recommendations for system applications to achieve the goals of optimized inputs and outputs of the system [McLoud et al., 2007]. An example of the AD system is conducting SWC monitoring with RS for input into Site-Specific Variable Rate Irrigation (SS-VRI) systems.

PA systems require specialized equipment to implement the recommendations developed using the AD system. The specialized equipment includes infrastructure, personnel and software required to implement the recommendations [McLoud et al., 2007]. For example, a SS-VRI requires an irrigation system capable of spatially varying irrigation depths, software capable of controlling the irrigation system based on the inputs from the AD process, and operators trained in the operation of the equipment and software. If there is a deficit in any aspect of the infrastructure, personnel or software, the PA system will not operate at the desired level [McLoud et al., 2007].

The final aspect of the PA system is continual evaluation and revision of the overall system. Continual evaluation of the PA systems inputs and outputs allow further revision of the system to increase efficiency and productivity [McLoud et al., 2007].

Implementing PA systems are a critical step towards addressing the increasing demand on our fresh water resources. The site-specific aspects of PA, such as using SS-VRI technology to spatially and temporally optimize irrigation applications based on the crop water requirements, provides for increases in water use efficiency and productivity while maintaining crop yield goals [Evans et al., 2013].

1.4. Site Specific Variable Rate Irrigation (SS-VRI)

Site-Specific Variable Rate Irrigation is an integral part of implementing a PA system on irrigated farmland. It is possible to obtain upwards of a 26% reduction in overall water usage using PA and SS-VRI [Evans et al., 2012]. The main goal of SS-VRI systems is the ability to spatially and temporally vary water application depths across a field to address specific soil, crop and/ or other conditions [Evans et al., 2013]. The systems use spatially distributed crop water requirement data to spatially and temporally vary water application across an agricultural field. The spatially distributed crop water requirements are derived using either ground-based measurements or remote sensing, which will be discussed later in the paper [Evans et al., 2013].

The most common SS-VRI systems are based on self-propelled, pressurized center pivot (CP) and linear move (LM) sprinkler irrigation systems. The CP and LM systems are easily adapted to SS-VRI systems due to their current high level of automation, their easily controllable water delivery devices, and cover a large area with a single lateral pipe. SS-VRI systems operate using either speed (sector) controlled application or management zones application [Evans et al., 2013].

Speed controlled SS-VRI systems vary irrigation application depths based on the travel speed of the irrigation system, as demonstrated by Figure 1.1. The rate of application remains constant along the entire system, while the speed is adjusted to achieve the desired water application depth [Evans et al., 2013]. Beginning in the 1980's, irrigation system manufacturers began to introduce systems that would allow the operators to control the speed of CPs. Recent developments of CP systems allow the pivot travel speed to be adjusted in $1^{o} – 10^{o}$ intervals, greatly increasing the efficiency of the speed controlled SS-VRI systems [Evans et al., 2013]. The benefit to using speed controlled SS-VRI is the lower costs associated with the infrastructure, operation, and data input requirements. The drawback to using a speed control SS-VRI is the lower overall efficiency due to the lower controllability of the system when compared to the zone controlled SS-VRI. The lower level of efficiency is based on that a majority of fields do not vary linearly, with respect to SWC, across the effective range of the system. Even with the drawbacks associated with the systems, the speed controlled SS-VRI is the most common SS-VRI system in use today due to the associated costs ($25-$125/ha) and the availability of the technology [Evan et al., 2013].

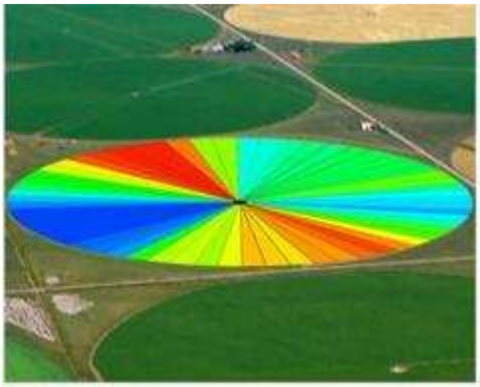

Figure 1.1. Speed Controlled SS-VRI Prescription using Valley VRI Speed Control Software [Valley VRI Speed Control Prescription, Valley Irrigation, Omaha, NE]

Zone management controlled SS-VRI systems vary irrigation application depths based on spatially distributed irrigation management zones, as seen in Figure 1.2. The application rates of individual or groups of sprinkler heads are varied to achieve the necessary application amount [Evans et al., 2013]. A vast majority of the zone control SS-VRI systems utilize pulse modulation to vary the application rate based on the management zones specifications. The zone controlled SS-VRI systems are more efficient and allow for greater productivity, due to their ability to precisely apply water based on the spatially distributed crop water requirements. The drawbacks to using a zone controlled SS-VRI system are the associated costs of the system ($215-$570/ha) and the lack of readily available commercial equipment and training [Evans et al., 2013].

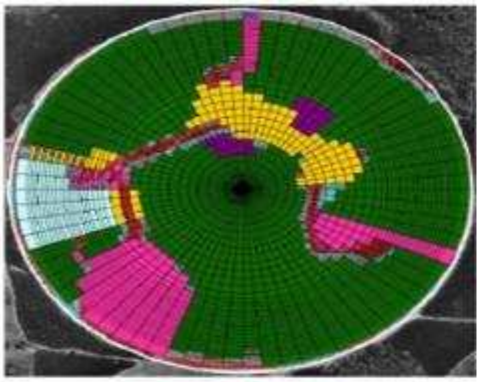

Figure 1.2. Zone Controlled SS-VRI Prescription using Valley VRI Speed Control Software [Valley VRI Speed Control Prescription, Valley Irrigation, Omaha, NE]

1.5. Spatially Distributed Soil Water Content (SWC)

Precision Agriculture and SS-VRI systems require site specific, spatially distributed root zone (R_z) SWC information as an input into the analysis and decision making process [Petetropoulos, 2014]. In the context of this paper, SWC is the water contained in the soil root zone that can be utilized for evapotranspiration (ET). SWC originates from rainfall (precipitation), irrigation, and/or capillary rise from ground water. The SWC can be further characterized as surface SWC (0-5 cm) and root zone SWC (5 cm to maximum depth of water extraction by roots) [Hillel 1998, Seneviratne et al., 2010]. The highly variable, spatially distributed nature of SWC is a result of multiple intertwined systems including soil characteristics, topography, plant biophysical properties, meteorological and irrigation conditions. In order to develop the required SWC data, one of three general processes are utilized [Petetropoulos, 2014].

1.5.1. Physically Based Soil Water Content

The first method utilizes physical measurements of the *in-situ* root zone SWC. The SWC is measured using the Gravimetric Soil Water Content Method (accepted standard of measurement), and soil water sensors, such as the Neutron Scattering (NP), Frequency Domain

Reflectometry / Capacitance (FDR), Time Domain Reflectometry (TDR), Resistance and Tensiometers [Petetropoulos, 2014]. The physically based methods are the most accurate, but have multiple drawbacks associated with their use. The area of most concern is the lack of spatially distributed SWC data. This is due to the time consuming and labor intensive nature of physically based SWC estimation [Finn, 2011]. The physically derived SWC are point measurements that are used to interpolate the spatially distributed SWC based on known physical and environmental conditions. The vertical and horizontal variability of soils and crop characteristics make it difficult to interpolate the point measurements across an entire field [Hoffman et al., 2007].

The Gravimetric, NP and FDR will be discussed in detail in a Chapter 2. For the general discussion in this section, the gravimetric SWC is the ratio of the mass (kg) of water present in a soil (M_w) sample to the dry mass (kg) of the soil sample (M_s) [Black, 1965]:

$$\theta_m = \frac{M_w}{M_s} \tag{1.1}$$

The θ_m is then converted to the volumetric SWC (θ_v, m m^{-1}) using the soil bulk density (ρ_b, g cm^{-3}) and water density (ρ_w, g cm^{-3}) [Black, 1965]:

$$\theta_v = \theta_m \times \frac{\rho_b}{\rho_w} \tag{1.2}$$

1.5.2. Meteorological and Crop Coefficient based Soil Water Content

The second method utilizes a root zone soil water balance, such as the Food and Agriculture Organization (FAO) Irrigation and Drainage Paper Number 56 Soil Water Balance Approach [Allen et al., 1998] to track SWC and depletion in the root zone [Neale et al., 2012].

The FAO 56 SWB will be addressed in detail in Chapter 2. The losses or crop water usage, are estimated by using the American Society of Civil Engineers (ASCE) Environmental and Water Resources (EWRI) standardized evapotranspiration (ET_{ref}) and crop coefficients (k_c), to derive the actual crop ET (ET_a). Evapotranspiration is the loss of water from the surface to the atmosphere by the combined process of evaporation from any surface or bare soil, and transpiration from vegetation [Allen et al., 1998]. ET varies both spatially and seasonally, based on vegetative characteristics, soil water status and meteorological conditions [Allen et al., 1998]. ET is affected by factors including solar radiation, wind speed, vapor pressure deficit, and air temperature [Li et al., 2009]. The crop coefficients are crop specific and vary with climate, water availability, and crop characteristics. Crop coefficients (k_c) are defined as the ratio of the crop ET to the ASCE-EWRI ET_{ref} [ASCE-EWRI, 2005].

$$k_c = \frac{ET_a}{ET_{ref}} \tag{1.3}$$

There are two forms of crop coefficients, the mean k_c and the dual k_c. The mean k_c is calculated, including surface wetting events (e.g. irrigation), as the long-term average of the crop ET to the ET_{ref}. The dual k_c is estimated using the mean basal k_{cb}, the stress coefficient (k_s) and the soil evaporation coefficient (k_e) [Neale et al., 2012]. The mean k_c is used for long term planning, while the dual k_c is used for irrigation scheduling [Hoffman et al., 2007]. The actual crop evapotranspiration (ET_a) is calculated using the dual crop coefficient (k_c), weather data, crop information and the reference evapotranspiration (ET_{ref}):

$$ET_a = (k_{cb} \times k_s + k_e) \times ET_{ref} \tag{1.4}$$

where the ET_{ref} (mm d^{-1}) is calculated using the ASCE-EWRI approach [Allen et al., 1998 or ASCE-EWRI, 2005; respectively].

$$ET_{ref} = \frac{0.408\Delta(R_n - G) + \gamma \frac{900}{T+273} u_2 (e_s - e_a)}{\Delta + \gamma(1 + 0.34u_2)} \tag{1.5}$$

ET_{ref} is the reference evapotranspiration, (mm d^{-1} or mm h^{-1}); R_n is the net radiation, (MJ m^{-2} d^{-1} or MJ m^{-2} h^{-1}); G is the soil heat flux, (MJ m^{-2} d^{-1} or MJ m^{-2} h^{-1}); (e_s - e_a) represents the vapor pressure deficit of the air, (kPa); e_s is saturation vapor pressure of the air, (kPa); e_a is the actual vapor pressure of the air, (kPa); Δ is the slope of the saturation vapor pressure temperature relationship, (kPa $^oC^{-1}$); γ is the psychrometric constant, (kPa $^oC^{-1}$); u_2 is the wind speed at 2 m height (m s^{-1}); T is the mean daily air temperature at 2 m height (^oC)[ASCE-EWRI, 2005].

The FAO-56 SWB approach starts with a given soil water profile at field capacity (θ_{FC}, mm m^{-1}). Field capacity is generally defined as the amount of water held in the soil after excess water has drained away and the rate of downward drainage has decreased. Once the SWB begins, the daily allowable depletion (or SWD), and root zone SWC are tracked by accounting for the losses (ET_a, surface runoff (SRO), and deep percolation (DP)) and the gains of the system (net irrigation (I_n), net precipitation (P_n) and ground water capillary rise (GW)) [Hoffmann et al., 2007]. The FAO 56 SWB will be describe in detail in Chapter 2.

While using the FAO 56 SWB is an effective, cost efficient method for estimating crop soil water requirements, there are several factors that affect the accuracy of the results [Petetropoulos, 2014]. The first factor is the requirement of high quality meteorological data for the calculation of the reference ET at the field location. The second factor is the uncertainty of the calculations of the crop coefficients for the site specific conditions related to soil water availability, crop biophysical characteristics (homogenous canopy cover, etc.), environmental conditions, and other non-water related stresses [Hoffmann et al., 2007].

1.5.3. Remote Sensing of Soil Water Content

The third method of estimating root zone SWC is through the use of remote sensing [Gowda et al., 2009a]. Remote sensing is the art and science of identifying, observing and measuring the radiation of different electromagnetic wavelengths reflected or emitted from an object without coming into direct contact [Petetropoulos, 2014]. While high resolution multispectral remote sensing is a relatively new field, remote sensing has been utilized for over 160 years. Beginning with primitive cameras tethered to balloons during the 1840's to today's satellite-based, high resolution, multispectral platforms, remote sensing has been used to document and explain the world around us [NASA Landsat]. The theory of remote sensing is based on comparing the wavelength specific reflective properties of different surfaces, and the emitted thermal radiation of all objects [Petetropoulos, 2014].

1.5.3.1 Electromagnetic Spectrum

Recently, RS has focused on using space-borne, aerial and ground-based multispectral imaging to map land cover and attributes [Petetropoulos, 2014]. RS focuses primarily on estimating ET_a and crop vegetation indices (VI) [Finn, 2014]. The primary bands of the electromagnetic spectrum that have been studied, in regards to SWC, are the visible (VIS) (blue: 0.45-0.49 µm, green: 0.49 – 0.57 µm, red: 0.62-0.75 µm), and near-infrared (NIR: 0.75-0.90 µm) to derive vegetation indices and spectral reflectance-based crop coefficients; and thermal infrared (TIR: 3.5-20 µm) to derive surface temperatures and surface energy fluxes [Petetropoulos, 2014].

1.5.3.2. Satellite Remote Sensing Platforms

Historically, the focus of remote sensing research revolved around the use of satellite-based platforms. There are multiple satellite-based remote sensing platforms in earth's orbit, such as the National Aeronautics and Space Administration's (NASA) Advanced Space-borne Thermal Emissions and Reflection Radiometer (ASTER), Moderate Resolution Imaging Spectroradiometer (MODIS), and the National Oceanic and Atmospheric Administration (NOAA) Advanced Very High Resolution Radiometer (AVHRR). The most commonly used satellite-based remote sensing platform is the NASA Landsat series satellites [Petropoulos, 2014]. The Landsat satellites have maintained continuous multispectral and thermal imagery coverage of the earth's surface since July 1978 [NASA Landsat].

Satellite remote sensing platforms form the basis for many of the current SWC algorithms, due to their inexpensive, free in the case of Landsat, spatially distributed and readily available multispectral imagery [Petetropoulos, 2014]. However, there are major drawbacks to using satellite remote sensing data for precision agriculture applications. The spatial resolution of the Landsat series satellites (Table 1.1) is approximately 30 m for the VIS and NIR bands while approximately 100 m for the TIR bands [NASA Landsat]. The relatively low spatial resolution of the data prohibits the development of management zones of less than 30 m by 30 m for use in SS-VRI systems. The optimal spatial resolution for use in a zone management SS-VRI system is based on the area of influence for the individual sprinklers in order to develop efficient zones for each sprinkler head [Evans et al., 2013]. The lack of ability to produce more accurate management zones greatly reduces the effectiveness of a zone management SS-VRI system utilizing satellite-based RS. All of the SWC algorithms require imagery under clear sky conditions (no cloud cover) for accurate estimation of SWC [Petetropoulos, 2014]. Satellite platforms have a fixed overpass temporal resolution, 16 days for Landsat, which can cause multiple issues due to spatially and temporally variable meteorological conditions. With the fixed overpass temporal resolution, weather condition, such as cloud cover or atmospheric haze, can render the data unsuitable for use with SWC algorithms [Petetropoulos, 2014]. In order to use the satellite-based remote sensing in SWC algorithms, the actual ET between overpasses must be interpolated from the RS data of the current and previous overpasses [Li et al., 2009]. In semi-arid (or arid) environments, or limited irrigation systems, the large temporal resolution does not allow the required accuracy to independently manage a precision irrigation system. In the case of changing meteorological conditions between overpasses, the errors associated with interpolating SWC between overpasses greatly increases [Neale et al., 2012]. Additionally, satellite remote sensing data must be corrected for the atmospheric conditions (water content, particulate concentration, etc.) during the overpass [Hadjimitsis et al., 2004]. The drawbacks of the satellite platforms led researchers and the agricultural community to develop airborne multispectral remote sensing platforms that are more responsive to meteorological conditions and irrigation manager’s needs [Petetropoulos, 2014].

Table 1.1. NASA Landsat 8 Characteristics [NASA Landsat, 2015]

Remote Sensing Satellites				
Platform	**Band**	**Wavelength (Micrometers)**	**Spatial Resolution (Meters)**	**Temporal Resolution (Days)**
LANDSAT 8	1 - Costal Aerosol	0.43-0.45	30	16
	2 - Blue	0.45-0.51	30	
	3 - Green	0.53-0.59	30	
	4 - Red	0.64-0.67	30	
	5 - NIR	0.85-0.88	30	
	6 - SWIR 1	1.57-1.65	30	
	7 - SWIR 2	2.11-2.29	30	
	8 - Panchromatic	0.50-0.68	15	
	9 - Cirrus	1.36-1.38	30	
	10 - TIR 1	10.60-11.19	100 (30)	
	11 - TIR 2	11.50-12.51	100 (30)	
ASTER	1 -Green1	0.52-0.60	15	16
	2 - Red 2	0.63-0.69	15	
	3 - NIR 3	0.76-0.86	15	
	4 - SWIR 1	1.60-1.70	30	
	5 - SWIR 2	2.145-2.185	30	
	6 - SWIR 3	2.1858-2.225	30	
	7 - SWIR 4	2.235-2.285	30	
	8 - SWIR 5	2.295-2.365	30	
	9 - SWIR 6	2.360-2.430	30	
	10 - TIR 1	8.125-8.475	90	
	11 - TIR 2	8.475-8.825	90	
	12 - TIR 3	8.925-9.275	90	
	13 - TIR 4	10.25-10.95	90	
	14 - TIR 5	10.95-11.65	90	

1.5.3.3. Airborne Remote Sensing Platforms

The development of airborne remote sensing platforms were primarily driven by their inherent payload and operational flexibility. Airborne remote sensing platforms range in design from small Unmanned Aircraft Systems (sUAS) to multi-engine jets capable of high altitude flights. The flexibility of airborne remote sensing platform's payloads afford operators the ability to customize the data collected to fit the analytical needs of the end user. For SWC estimation, airborne remote sensing platforms attempt to mimic the Landsat multispectral collection capabilities of red, NIR and TIR bands [Chávez et al., 2009]. Colorado State University (CSU) and Utah State University (USU) are currently conducting research with sUAS and manned aircraft remote sensing platforms that collect optical imagery of the red, and green bands, as well as in the NIR and TIR bands of the electromagnetic spectrum. The CSU Tempest and USU manned aircraft have a spatial (pixel) resolution of approximately 0.06/0.12 m (Tempest – VIS NIR / TIR) and 0.5/1.8 m (USU– VIS NIR / TIR) respectively [Chávez et al., 2012]. The operational flexibility of airborne remote sensing platforms allow the rapid deployment of the platforms in response to changing weather conditions and/or data requirements. The ability to adjust the timing and frequency of overpasses with the airborne systems are a significant advantage over the satellite remote sensing platforms. Not only can data collection occur when the opportunity presents itself on cloudy days, but also the ability to fly more frequently allows for greater SWC estimation accuracy when using RS algorithms and SWBs. The ability to vary flight characteristics of an airborne remote sensing platform are another benefit over satellite platforms. By adjusting the flight parameters (e.g., flight speed and altitude), the spatial resolution of the imagery can be adjusted to meet the information requirements of precision agricultural irrigation system. Additionally, based on the lower operating altitude of the aerial platforms, the amount of atmospheric correction is reduced. Therefore, reducing the error associated with the atmospheric corrections with the use of the multispectral imagery [Chávez et al., 2008].

The airborne remote sensing platforms are not without drawbacks. Like satellite platforms, airborne systems must collect data during clear sky conditions. Even though their flight schedules are adaptable, this is still a requirement for most of the algorithms. Processing data from airborne remote sensing platforms is time consuming and requires in-depth technical knowledge by the operators [Gowda et al., 2008]. Satellite platforms cover large areas with a single image, 33,300 km^2 (185 km swath) for the Landsat [NASA Landsat, 2015], while the airborne platforms cover much smaller areas, 0.0049 km^2 (78 m swath) for the CSU Tempest UAS operating at 121 m AGL. The smaller image footprint requires a greater amount of image pre-processing, calibration, and a significant increase in the amount of required digital storage. One of the largest drawbacks to airborne remote sensing platforms are the costs associated with their operation. While there is an abundant amount of free data from satellite remote sensing platforms, vast majorities of airborne remotes sensing platforms are commercially purchased products or the equipment must be purchased by the operators [Petropoulos, 2014]. For example, the USU remote sensing aircraft cost approximately $3,666.67 per flight during the CSU Summer 2015 campaign and the overall purchase and development cost of the CSU Tempest is over $100,000. The price of the airborne systems will decrease as the technology becomes more wide spread, but there will still be a significant investment for their operations.

1.5.3.4. Ground-based Remote Sensing

Ground-based remote sensing, with regards to SWC, have two main goals, estimation of SWC, and the validation and calibration of the aerial and space-borne remote sensing platforms' raw data [Petropoulos, 2014]. Ground-based remote sensing platforms are deployed in a variety of methods, such as installation at fixed locations, hand-held or equipment (e.g. tractors) mounted sensors. The sensors are used to collect point data, such as an infrared thermometer or a multispectral radiometer (multi-band), or can collect spectral imagery with equipment similar to the aerial systems [Petropoulos, 2014]. The advantage of using ground-based remote sensing platforms are their capability to continuously collect data for use in the estimation of SWC. Another advantage to using ground remote sensing systems are their use in validating and calibrating data collected using aerial platforms. By calibrating the aerial data with the ground data, a site-specific calibration can be developed for the aerial system, greatly reducing the amount of error from the aerial system [Chávez et al., 2012].

As with the other RS systems, ground-based systems have their own drawbacks. The largest issue is that the data are not spatially distributed. This requires interpolation from known points throughout the field, similarly to the physical methods of estimating SWC. The collection of ground-based remote sensing data are very labor and knowledge intensive, as well as, time consuming due to the installation and operating requirements [Petropoulos, 2014].

There are multiple ways to acquire remote sensing data, all of which have their strengths and weaknesses. The advantage of remote sensing is the ability to combine data from multiple sources, both physical and remote sensing, to develop the most accurate estimation of spatially distributed SWC [Petetropoulos, 2014].

1.5.3.5. Remote Sensing SWC Algorithms

The ability to derive the SWC for the entire root zone profile is still in its infancy, beginning in earnest in the 1970's with the launch of the Landsat 1 satellite [Petropoulos, 2014]. There are many different models that estimate the surface SWC and then extrapolate the SWC for the remainder of the root zone soil profile [Li et al., 2009]. A majority of the RS SWC models derive the SWC based on the estimation of intermediate processes, such as the instantaneous ET_a. The RS derived instantaneous ET_a is calculated using one of multiple available algorithms based on the surface energy balance (SEB) methods, reflectance-based crop coefficient methods, thermal-based Crop Water Stress Index (CWSI) or many other methods [Gonzalez-Bugo et al., 2009]. A description of the SEBAL, METRIC and Triangle Methods can be found in Appendix 2. Though effective, in order to exclusively use these models for irrigation scheduling in a precision agriculture system, the RS data would have to be available on nearly a daily basis [Neale et al., 2005]. For this reason, the most applicable derivation of SWC for PA utilizes a hybrid ET model, originally proposed by Neale et al. The model for estimating SWC proposed by Neale et al. (2012) integrates RS derived ET_a and reflectance-based crop coefficients with the FAO-56 SWB approach [Neale et al., 2012]. The Hybrid SWC model uses the SWB approach to continuously estimate the SWC between RS overpasses. Data collected from RS overpasses are then used to develop the reflectance-based crop coefficients, as well as RS derived ET_a. They hybrid model was designed using the TSEB, but other, parameter appropriate RS algorithms for ET_a can be used. The RS derived ET_a is assimilated into the FAO 56 SWB ET_a, which yields a more accurate estimation of the ET_a [Neale et al., 2012]. The reflectance-based crop coefficient and updated ET_a are then used to update the SWD and finally SWC in the crop root zone [Neale et al., 2005]. The hybrid model is based on the assumption that reflectance-based crop coefficients and ET derived through RS methods, are more accurate than traditional methods of estimating ET and tabulated basal crop coefficients [Neale et al., 2012]. The hybrid model increases the accuracy of the FAO-56 SWB in two ways. The first way is by updating the spatially distributed SWD in the soil water balance. The second advantage is the adjustment of the spatially distributed crop coefficients based on actual growth and crop health conditions, used in the SWB [Neale et al., 2012].

1.5.3.5.1. Surface Energy Balance (SEB) Estimation of actual ET

The SEB methods are the most commonly used methods of estimating ET_a with RS data. The SEBs has its origins in the early work of Sone and Horton (1974) and Verma (1976) and their work with the Landsat RS data. The SEB operate under the principle of the conservation of energy and calculate the latent heat flux (LE) as the residual of the surface energy balance (Figure 1.3) [Petropoulos, 2014].

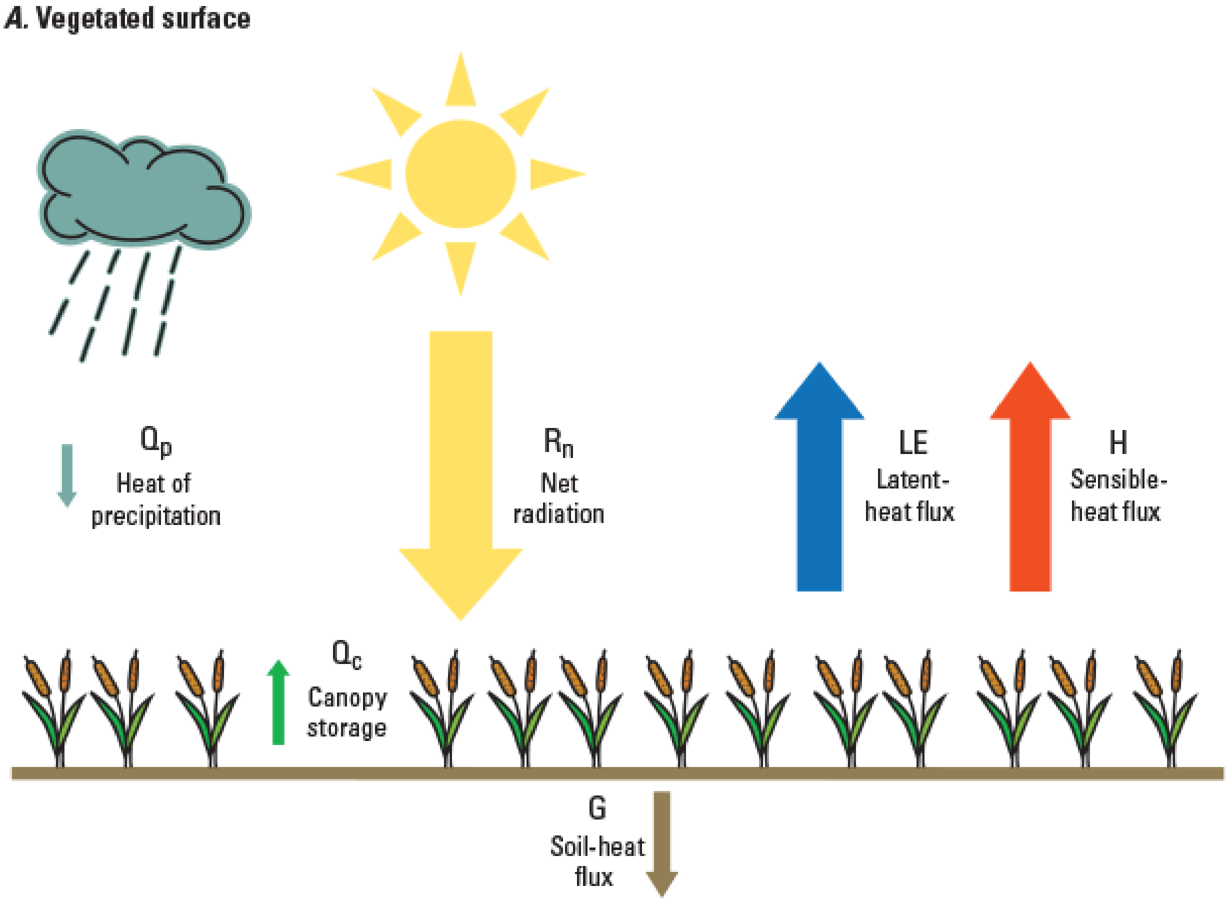

Figure 1.3. Surface Energy Balance (adapted from Petropoulos, 2014)

The derivation of the spatially distributed (each pixel of the RS image) ET_a uses the spatially distributed radiometric surface temperature and multispectral RS imagery, by calculating the LE as the residual of the surface energy balance equation:

$$LE = Rn - G - H \tag{1.6}$$

where LE is the latent heat flux (W m^{-2}), R_n is the net radiation (W m^{-2}), G is the soil heat flux (W m^{-2}), and H is the sensible heat flux (W m^{-2}) [Moran et al., 1994; Kustas and Norman, 1996; Gillies et al.,1997; Bastiaanssen et al., 1998]. In SEB methods, the R_n and G are accurately estimated using the SEBs models, while the H is calculated using multiple methods [Chávez et al., 2010]. The R_n is calculated as the sum of the incoming and outgoing long and short wave radiation budget, with inputs from remote sensing derived VIS, NIR and TIR, and physical/meteorological variables. [Monteith, 1973]. The G is calculated as a function of R_n, TIR RS data and VI's [Bastiaanssen et al., 1998].

In all of the SEB models the methods of calculating H are different, but all revolve around a measure of the difference (dT) in aerodynamic surface temperature (T_o, K) (or radiometric surface temperature (T_{sfc}, K)) and air temperature (T_a, K), and the aerodynamic resistance to heat transfer (r_{ah}, s m^{-1}) [Gowda et al,. 2007].

The main advantage of using the SEB methods is that by using the thermal RS imagery, ET_a can be calculated without prior knowledge of the soil profile characteristics [Neale et al., 2012]. The SEB methods can calculate the components as a single source (soil and canopy combined) or as a two-source (soil and canopy partition into separate components) energy balance [Li et al., 2009].

The main drawback of the SEB methods of estimating ET_a is the requirement of high resolution physical and RS data. For application in a precision agriculture system, RS data must have the spatial resolution to derive SWC that matches the PA capabilities. Additionally, the SEB methods require high quality meteorological data for the site [Gonzalez-Dugo, 2008].

1.5.3.5.1.1. Single Source Energy Balance Methods

The single source energy balance methods are based on the difference of the T_o (or T_{sfc} as an estimation of T_o) and T_a or between the temperatures of the dry and wet limits derived from ground-based meteorological and RS data [Li et al, 2009]. The direct temperature-based single source SEBs calculate H as a function of the T_o (or T_{sfc}) and the T_a. While the dry and wet limit based single source methods assume ET boundary condition based on the model's definition of maximum ("hot or dry") and minimum ("cold or wet") surface temperatures. The minimum temperature is correlated with the maximum potential ET (ET_p) and the maximum temperature is correlated with low or 0 ET [Li et al., 2009]. The wet and dry boundary conditions are based on individual pixels from the RS imagery. The Surface Energy Balance Index (SEBI) developed by Menenti and Choudury, was the predecessor to the current single source models such as the Surface Energy Balance for Land (SEBAL) (see Appendix 2 for a description of the SEBAL method), Mapping Evapotranspiration at High Resolution with Internal Calibration (METRIC) (see Appendix 2 for a description of the METRIC method) and the Surface Aerodynamic Temperature (SAT) models. The major differences between the models are how each calculate the sensible heat flux (H) and how they define the "hot" and "cold" boundary conditions or pixels. The single source models are suited for locations with homogenous canopy covers, but lose accuracy over non-homogenous canopy covers due to calculating the components of the SEB as the combination of both the soil and canopy contributions [Li et al., 2009, Normal et al., 1995].

The SAT method is a single source SEB model, but unlike the SEBAL or METRIC models, it does not use a linear relationship (dT) of the boundary conditions to calculate the difference in aerodynamic surface (T_o) and air temperatures (T_a). Instead, the aerodynamic temperature is calculated, pixel by pixel, as a function of the radiometric surface temperature (T_{sfc}), air temperature, Leaf Area Index (LAI) and wind speed (u) [Chávez et al., 2010]. For precision agriculture application, the SAT method is suited to high resolution, aerial-based RS data. The SAT model produces spatially distributed ET_a that are not limited by artificially enforced boundary conditions. The SAT model was developed to address the overestimation of H when using the radiometric surface temperature (T_{sfc}) rather than the aerodynamic surface temperature (T_o) [Chávez et al., 2010]. Over homogeneous surfaces, T_s and T_o are generally equal, but over heterogeneous surfaces the values vary [Wenbin et al., 2004]. The over estimation of H is due to T_{sfc} generally being greater than T_o for unstable atmospheric conditions, and variance of the values over heterogeneous surfaces. The over estimation of H lead to an under estimation of LE and consequently ET_a [Chávez et al., 2010].

The SAT model is best suited for crop specific applications with UAS based remote sensing. Chávez et al. (2005), as well as others (Mahrt and Vickers (2004), etc.) have developed crop specific estimations of T_o. In order for more wide spread application of the SAT method, a generalized model of T_o needs to be developed [Chávez et al., 2010]. Additionally, crops under significant stress present a challenge to the SAT model due to the large variance between the T_o and T_s [Chávez et al., 2010]. The SAT Model will be discussed in detail in Chapter 2 utilizing data from the CSU Tempest UAS RS platform.

1.5.3.5.1.2. Two Source Energy Balance (TSEB)

In order to address the issues of the single source SEB methods when dealing with heterogeneous canopy covers and elevated crop stress levels, the TSEB was developed by Norman et al. 1995. The TSEB method [Norman et al., 1995] approaches the SEB by estimating the fluxes for the vegetation and soil background separately. Depending on the model, the resistances are either modelled in parallel or series. The TSEB parallel resistances methods assume that the contribution of the canopy and the soil layers to the total sensible heat fluxes (H) depend on the difference in temperature of each of the layers (T_{sfc}) and the atmosphere (T_a). This is helpful when deriving ET_a over heterogeneous surfaces because it does not require site-specific calibration to account for varying biophysical conditions. This allows for a more accurate estimation of the overall systems sensible heat flux (H), based on the composite canopy and soil values. [Hipps and Kustas, 2001]. The vegetation is separated from the soil using vegetation fractional cover (f_c), which is derived from vegetation indices and LAI. The TSEB model utilizes RS derived radiometric surface temperature (T_{sfc}), and multispectral imagery (NIR, red, green, and blue), as well as ground measured metrological data. Of the SEB models, the TSEB is one of the most data intensive and technically complicated models and requires high resolution spatially distributed RS and meteorological data. Since the development of the TSEB methods, it has been the subject of many studies utilizing airborne and satellite-based remote sensing [Sellers et al., 1992; Kustas et al., 2012; Chávez et al., 2009; etc.]. The current TSEB research focuses on using aerial-based remote sensing platforms, which have high spatial and temporal resolutions, for use with PA systems. The TSEB Model will be discussed in detail in Chapter 2 utilizing data from the CSU Tempest UAS RS platform.

1.5.3.5.2. Reflectance-based Crop Coefficients (k_{cbrf})

The reflectance-based crop coefficient methods are based on the meteorological and crop coefficient based method discussed previously. They differ in the method of ascertaining the crop coefficient (k_{cb}). The reflectance-based crop coefficients (k_{cbrf}) are calculated using RS data of two or more bands of the electromagnetic spectrum, such as red and NIR [Neale et al., 1989]. The multispectral imagery are used to calculate vegetation indices, such as the Normalized

Difference Vegetation Index (NDVI). The NDVI is the ratio of the NIR and red bands. The VI is then linearly related to the reflectance-based crop coefficient [Gonzalez-Dugo and Mateos, 2008]. To estimate the other components (k_e) of the dual crop coefficient, a soil water balance is utilized. The reflectance-based crop coefficient is then used to calculate the ET_a using a form of Eq. (1.3). The reflectance-based crop coefficient method allows for the adjustment of the crop coefficients based on the spatial variation of soil characteristics, crop health, growths stage and water availability (i.e. water stress), instead of using the idealized conditions based on the growth stage and ET_{ref} [Neale et al., 2012]. The method only requires the NIR and red RS images and is a simple empirical model. The benefit of the model is that it provides for an easy application for site-specific modeling of ET_a and SWC over a spatially distributed area for use in precision agriculture irrigation management programs [Neale et al., 2012]. The Reflectance-based Crop Coefficient Model will be discussed in detail in Chapter 2 utilizing data from the CSU Tempest UAS RS platform.

1.5.3.5.3. Thermal-based Crop Water Stress Index Method (CWSI)

The CWSI method [Idso et al., 1981] is similar to the reflectance-based crop coefficient model, in that the CWSI is used to derive ET_a from the reference ET. The CWSI varies from 0 (no stress) to 1 (maximum stress). The difference between the two models is that the CWSI utilizes the RS thermal imagery instead of the multispectral (red, NIR) imagery. The CWSI is derived from relating the difference (dT) in radiometric surface temperature (T_{sfc}) to the air temperature (T_a), similar to the SEBAL and METRIC models [Idso et al., 1981]. The method is based on the assumption that if there is sufficient water in the root zone, all available energy will be used by the plant for transpiration. Once all the water which the crop can easily extract (RAW) has been depleted from the root zone soil profile, available energy will cause heating of the canopy (Maes and Steppe, 2012). The CWSI is calculated as a ratio of the difference of dT and the lower limit boundary surface temperature (dT_{ll}) and the difference between the upper (dT_{ul}) and lower boundary surface temperature. Where dT_{ll} is the lower boundary surface temperature (non-water stress condition, atmospheric controlled ET) and is a function vapor pressure difference (VPD). The dT_{ul} is the upper boundary surface temperature (non-transpiring condition) and is a function of the vapor pressure gradient (VPG). The spatially distributed ET_a is calculated using the CWSI as a reduction coefficient for the potential ET (ET_p), calculated from the reference ET and the basal crop coefficient [Idso et al., 1981].

The CWSI method shows promise for use in UAS-based RS PA irrigation systems because of its potential to detect stress sooner than the reflectance-based crop coefficients [Idso et al., 1981]. The drawbacks to the model are that empirical models must be developed for specific crops, its inability to estimate bare soil ET_a, and the data requires collection after solar noon to be used without correction [Chávez et al., 2012, DeJonge et al., 2015]. The CWSI Model will be discussed in detail in Chapter 2 utilizing data from the CSU Tempest UAS RS platform.

1.5.3.6. Instantaneous LE to daily ET_a

The output of the SEB models are spatially distributed instantaneous LE, which are of very little use when implementing a precision agriculture irrigation management system. When using a SEB model to calculate ET_a, the instantaneous LE are converted to the instantaneous ET_a and extrapolated to the daily ET_a. The instantaneous ET_a is calculated using the following equation:

$$ET_a = \frac{3600 \times LE \times 1000}{\lambda_v \rho_w} \tag{1.7}$$

where λ_v is the latent heat of vaporization (J kg^{-1}), ρ_w is the density of water (approximately 1,000 kg m^{-3}) and ET_a is the actual hourly ET (mm h^{-1}) [Allen et al., 2007]. The extrapolation from the hourly ET_a to daily ET_a is accomplished using one of several methods. The two most common methods utilize the Evaporative Fraction (EF) or the Reference ET Fraction (ET_rF) [Allen et al., 2007].

1.5.3.6.1. Evaporative Fraction (EF)

The EF is calculated as the ratio of the energy fluxes at the time of the overpass. The EF method is based on the self-preservation theory of daytime fluxes, which states that the ratio between the LE and the available energy remains constant throughout the day [Bastiaanssen, 1998a, Shuttleworth et al., 1989].

$$EF_i = EF_d = \left(\frac{LE}{R_n - G}\right)_i \tag{1.8}$$

where EF_i is the instantaneous EF, and EF_d is the daily EF. The daily ET_a is then calculated using the EF and the assumption that G tends to 0 for the entire day [Bastiaanssen, 1998]:

$$ET_{a_d} = 86,400 \frac{EF \times R_{n_d}}{\lambda_v \rho_w} \tag{1.9}$$

The major drawback to the method is its dependence of all terms on the remote sensing data and preforms poorly in advective or arid environments [Allen et al., 2007]. To address this issue, the ET_rF method was developed using both RS derived ET_a and the ASCE- EWRI (2005) standardized reference ET.

1.5.3.6.2. Reference ET Fraction (ET_rF)

The ET_rF method estimates the pixel-by-pixel, daily actual ET of a RS image. It utilizes both the RS derived hourly ET_a and the ASCE-EWRI reference ET (ET_{ref}) to extrapolate the hourly ET_a to the daily ET_a [Allen et al., 2007]. The ET_rF is calculated using the following equation:

$$ET_rF = \frac{ET_{a_i}}{ET_{ref_i}} \tag{1.10}$$

And the daily ET_a is calculated utilizing the ET_rF as a crop coefficient and the daily ASCE-EWRI reference ET (ET_{ref}):

$$ET_{a_d} = ET_rF \times ET_{ref_d} \tag{1.11}$$

As with the EF method, the ET_rF is assumed as constant throughout the day [Allen et al., 2007].

1.6. Objectives

To meet the increasing demands on the global fresh water supply, all aspects of society must become more efficient in their water use. In the agricultural sector, the technology, ranging from SS-VRI systems to frequent, economical, high resolution, and spatially distributed RS derived irrigation planning models, have the potential to greatly reduce the overall water usage, while expanding the overall output to meet the increasing needs. The focus of the agricultural community, both operations and research, must focus on developing economical, applicable technology and systems that will provide incentive for large-scale implementation of the precision agriculture systems. The development of the SS-VRI, and other efficient PA systems, has created a need for high temporal and spatial resolution crop water requirement data. Ground-based measurements of crop water requirements are accurate, but are not an economically viable method for implementation in a spatially distributed PA system. On the other hand, the space-borne RS platforms are economically feasible, but lack the temporal and spatial (pixel) resolution required to independently provide the required inputs to a PA system. Development of airborne RS platforms, both manned and UAS, is prompted by the need to create a systematic approach that utilizes ground, aerial and space-borne data collection for implementation in PA systems. The systematic approach will create high resolution spatial and temporal SWD information for input into the PA systems. This will involve tracking the daily SWB (FAO-56 SWB) using ground measurements and ET models. The SWB will be updated using aerial RS. The systematic approach will provide responsive, efficient and economical, spatially distributed SWD information for the implementation of a PA system at the field level.

The overall goal of the study was to integrate an UAS and ground-based RS to estimate ET_a and SWD through the vegetation soil root zone over variable vegetation cover densities, in order to develop sustainable land management at the field level. The overall goal will be accomplished by comparing the performance of the Colorado State University (CSU), Department of Civil and Environmental Engineering (CEE) Tempest RS UAS platform vs. ground-based remote sensing data and physically measured SWD. The specific objectives are:

1. Evaluate the quality and relevance of data collected by the Tempest UAS RS platform when compared to data collected by ground-based methods.

2. Evaluate four RS ET_a algorithms (TSEB, SAT, CWSI, K_{cb}) using data collected by the Tempest UAS during the Summer 2015 RS campaigns at the primary test location, Agricultural Research Development and Education Center (ARDEC). The accuracy of each method will be computed using the mean biased error (MBE) and root mean squared

error (RSME) when compared with the physically measured ET_a calculated by a neutron probe (NP) soil water sensors. Identify the most appropriate ET_a algorithm for use in the SWD estimation.

3. Estimate the spatially distributed SWD of the test locations utilizing the most appropriate RS derived ET_a. The SWD will be estimated using the Hybrid SWB model develop by Neale et al. (2012).
4. Development and approval of the licensing, technology, and methodology associated with the CSU Tempest UAS.
5. Provide suggestions and recommendations for future CSU RS for agricultural research.

At the completion of the study, a practical procedure will be developed to provide estimates of the distributed SWD through the use of multispectral sensors integrated with the Tempest UAS. The ability to accurately and efficiently estimate the distributed SWD and ET_a will allow the increase of the overall efficiency at the end user level by providing timely data for site specific irrigation (i.e., water management), land management, in the form of trafficability (machinery transit), and the application of agro-chemicals as part of an integrated precision agricultural management program. Additionally, Colorado State University (CSU) will develop and implement a comprehensive UAS program that encompasses the operational approval process, flight crew certification, and operational planning at both the Department and University level. With an established UAS program, and loosening Federal Aviation Administration (FAA) regulations, Departments that are not historically focused on aeronautical research will be able to conduct research with UAS's.

CHAPTER 2: METHODS

The study focused on the evaluation of the Tempest UAS's ability to provide quality and relevant data as inputs for the RS models used to estimate ET_a and SWD at the field scale. Multispectral and thermal RS imagery and ground-based thermal and multispectral data were collected at the primary test location during the summer of 2015. The spatially distributed RS data was used to derive the spatially distributed ET_a and SWD of the test location. The ET_a and SWD were then evaluated using the measured NP and FAO-56 SWB derived ET_a and SWD. The primary test location, during the summer 2015 RS campaign, was the CSU Agricultural Research Development and Education Center (ARDEC – Fort Collins, CO).

The study was conducted over four phases. During the first phase (Phase 1 – UAS/Sensor Integration and Certification), the sensors were integrated with the UAS platform, and the certifications for UAS research operations at the test location was submitted and approved. The second phase (Phase 2 – Ground-based SWD Measurement) consisted of the ground-based data collection of the SWD and multispectral data at the test location. The collection of the RS data over ARDEC field 1070 occurred during the third phase (Phase 3 – Remote Sensing Campaign) of the study. Phases two and three occurred simultaneously in order to allow both spatial and temporal comparison of the data acquired from the test location. The fourth phase (Phase 4 – Data Analysis and Comparison) consisted of the analysis and comparisons of the data collected during phases two and three.

The following sections provide an overview of the study's details and experimental design. The first section describes the RS instrumentation and the development of the CSU Tempest UAS RS platform. The second section describes the test location, ground-based instrumentation and data collection. The third section discusses the CSU Tempest and the USU RS campaign, and the description of the RS data. The final section contains the methodology of the individual models utilized in deriving the ET_a and SWD, and the statistical analysis used in the evaluation and performance comparison.

2.1. UAS/Sensor Integration and Certification

The first phase of the study focused on the development and integration of the sensors with the Tempest, the pilot certification process and the approval of the flight authorizations for the Tempest. These tasks were completed by simultaneously focusing on two lines of effort (LOE). The first LOE focused on the preparation of the Tempest UAS for the RS campaign. The second LOE addressed the legal requirements of flying the Tempest in US national airspace.

2.1.1. Tempest UAS

The Tempest UAS (UASUSA, Inc., Longmont, CO, USA) (Figure 2.1) is a commercially purchased UAS platform based on a long range, fixed-wing, radio control (R/C) aircraft that was originally designed for flight operations in tornado-prone thunderstorms. The system is fully autonomous, with all flight and RS operations controlled through an on-board autopilot. The autonomous controls provide the stable platform required to collect high-resolution RS data.

Figure 2.1. Colorado State Universities Tempest UAS (Photo by CPT Jeffrey Hathaway)

The Tempest was a logical choice for adaptation into a high-resolution RS platform due to the inherent stability and efficiency of the design. The adaptability of the platform provides the required flexibility to adjust sensor payloads and flight parameters to meet the data collection needs. The specifications of the Tempest UAS are depicted in Table 2.1.

Table 2.1. Tempest UAS Performance Specifications [UASUSA, 2015]

Specifications	
Wingspan	127" (251 mm)
Wing Area	1016 sq in (0.65 sq m)
Empty Weight	10 lbs (4.54 kg)
Nominal GTOW	11 lbs (5 kg)
Maximum GTOW	20 lbs (9.07 kg)
Wing Loading	20.6 oz/sq ft
Length	61.375" (1524 mm)
Airfoil	MH-32
Center of Gravity	3.5" from leading edge of the wing (89mm)
Stall Speed	20 mph
Cruise Speed	50 mph
Max Speed	100 mph
Max Range	60 mi (52.14 NM)
Radio Range	10 mi (8.69 NM)
Flight Time	1.5 HR

The Tempest initially was integrated with five commercially available sensors, which was narrowed to three sensors based on the ability of the sensors to successfully integrate with the autopilot. The sensors were selected for their ability to collected multispectral and thermal imagery over the same bands as ground-based RS systems and the Landsat satellites. The specifications for the sensors' spectral and temporal resolution are described in Table 2.2 and Appendix 1. The final payload for the Tempest UAS included a multispectral (NIR, red, and green) camera [ADC SNAP, Tetracam Inc., Chatsworth, CA], a thermal infrared (TIR) camera [Tau 2 640, FLIR, Wilsonville, OR], and a digital camera (red, green, and blue) [SRL A6000 digital camera, Sony Global, Tokyo, Japan]. The CSU Tempest UAS is described in detail in Appendix 1.

Table 2.2. Tempest UAS Sensor Performance Specifications

Sensor	**nm**		**µm**		**Wavelength**	**130 m (AGL) Resolution**
FLIR TAU 2	7500	13,500	7.5	13.5	Thermal	11.76 cm
Tetracam SNAP ADC	520	920	0.52	0.92	green, red, NIR	6.5 cm
Sony A6000	390	780	0.39	0.78	Visible (RBG)	9.5 cm

2.1.2. CSU UAS Certification

The operation of the Tempest in the United States National Airspace (NAS) is tightly controlled by the Federal Aviation Administration (FAA). The authorizations required to conduct research are separated into two main categories: Pilot Certification and Aircraft Certification.

The CSU Tempest pilot certification programs are described in Appendix 1. The certification processes of the Tempest pilots are in accordance with FAA Notice 8900.1 and Title 14 of the Code of Federal Regulations (14 CFR). The certification process involves both formal and informal flight training, liability insurance, and a FAA Class 2 medical exam. The purpose of the CSU pilot certification program is to ensure the safety of the public and equipment associated with CSU UAS research operations. The flight training program, in preparation for the data collection flights, is a multi-staged program. The first stages of flight training are conducted using small scale R/C aircraft to develop the fundamental flight skills required to successfully fly the Tempest. The CSU program uses the Radian Parkzone R/C Aircraft [Radian PNP, Parkzone Inc., Champaign, IL] during the first stage of flight training and for refresher training during periods of low flight densities. The Radian uses throttle, rudder and elevators to provide basic flight controls. Upon completion of stage one, CSU pilots transition to the Radian

Pro R/C aircraft [Radian Pro PNP, Parkzone Inc., Champaign, IL]. In addition to throttle, rudder and elevator, the Radian Pro utilizes ailerons and flaps to provide realistic simulation of the Tempest flight controls. The specification and imagery for the Radian and Radian Pro are found in Table 2.3 and Figure 2.2. Once the Radian Pro flight controls have been mastered, the final stage of flight training is conducted on the Tempest UAS. The final stage includes training with the Tempest's manual flight controls, takeoff and landing procedures, and the SwiftPilot Autopilot.

Table 2.3. Radian and Radian Pro R/C Aircraft Specifications.

Radian and Radian Pro Specification	
	Radian and Radian Pro
Wingspan	78.5 in
Length	45.0 in
Flight Time	30 min
Weight	34.6 oz

Figure 2.2. Colorado State Universities Radian and Radian Pro R/C Aircraft [Parkzone.com]

The aircraft certification for the Tempest UAS is based on the FAA's Certificate of Approval or Waiver (COA). The COA process allows public entities (Government, State Universities, etc.) to conduct flights in the NAS. The COA is a process in which the FAA approves UAS to fly in specified location [FAA Notice 8900.1; 14 CRF]. The COA is the process that certifies that an incident at the approved location has the minimal probability of damage to personnel or property. To date, CSU has submitted three COAs, with five locations approved for flight operations.

2.2. Ground-based SWC Measurements

The second phase of the study focused on the collection of ground-based measurement of the SWC and RS data at the test location. Data collection was conducted throughout the 2015 growing season. The ground-based measurements were used for the comparison and evaluation of the Tempest RS derived data.

2.2.1. CSU ARDEC

The primary test location for the study was the CSU Agricultural Research Development and Education Center (40º 39.293' N 104º 59.848', Elevation – 1551 meters). ARDEC is an off campus agriculture research center, approximately 4 miles north of Fort Collins, CO. ARDEC is operated and maintained by the Colorado Agricultural Experiment Station and consists of 1,065 acres dedicated to agricultural research.

ARDEC field 1070 (Figure 2.3) consists of 2.79 acres irrigated with a pressurized lateral move sprinkler system. The test location is divided into twelve plots (23 m x 27.43 m) and 144 sub-plots (4.5 m x 4.5 m) as shown in Figure 2.3 and Figure 2.4.

Figure 2.3. CSU ARDEC Field 1070 layout during the summer 2015 Tempest UAS RS campaign.

The plots are divided into three irrigation treatments, with four replication of each treatment, as shown in Figure 2.3. The "Full" irrigation plots received one inch (I_n = 25.4 mm) of irrigation weekly to replicate the replacement of 100% of the ET_a. The "Limit" irrigation plots received one inch of irrigation weekly after the growth stage of the corn. The "Drought" plots received no irrigation during the growing season. Table 2.3 displays the irrigation schedule and amounts applied to the treatments during the 2015 growing season.

The plots were further divide into four columns (4.5 m x 27.43 m) that received four treatments, replicated four times, of various varieties of corn (P9697AM, P8954AM, P9675AM and P9305AM (annotated on Figure. 2.4). The sub-plots were subjected to five soil treatments (Control, Manure, Biochar and Manure, Biochar, and Null (bare soil)) replicated 12 times. A summary of the key dates for ARDEC 1070 are found in Table 2.4.

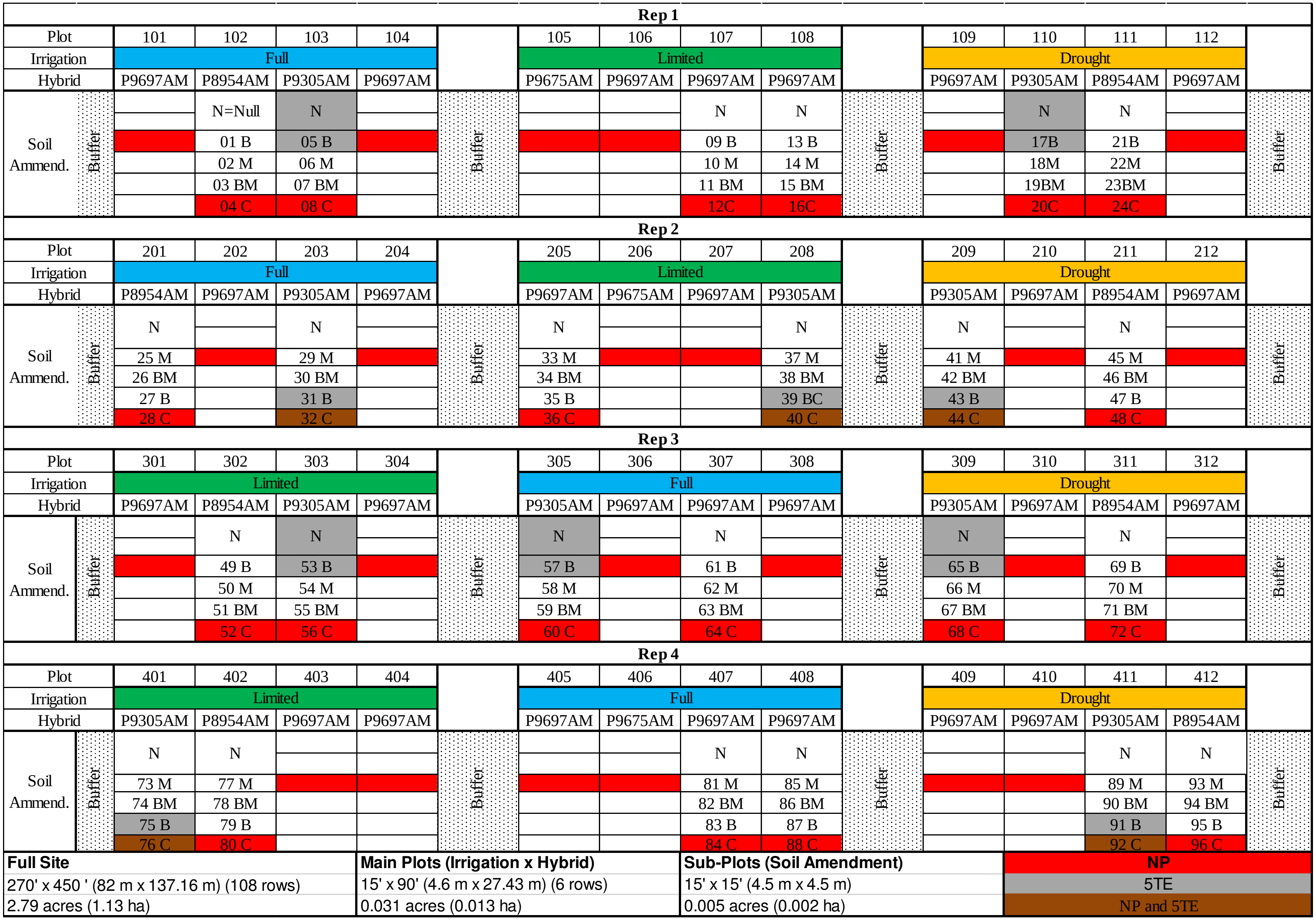

Rep 1																
Plot		101	102	103	104		105	106	107	108		109	110	111	112	
Irrigation		Full					Limited					Drought				
Hybrid		P9697AM	P8954AM	P9305AM	P9697AM		P9675AM	P9697AM	P9697AM	P9697AM		P9697AM	P9305AM	P8954AM	P9697AM	
Soil Ammend.	Buffer		N=Null	N		Buffer			N	N	Buffer		N	N		Buffer
		🟥	01 B	05 B	🟥		🟥	🟥	09 B	13 B		🟥	17B	21B	🟥	
			02 M	06 M					10 M	14 M			18M	22M		
			03 BM	07 BM					11 BM	15 BM			19BM	23BM		
			04 C	08 C					12C	16C			20C	24C		
Rep 2																
Plot		201	202	203	204		205	206	207	208		209	210	211	212	
Irrigation		Full					Limited					Drought				
Hybrid		P8954AM	P9697AM	P9305AM	P9697AM		P9697AM	P9675AM	P9697AM	P9305AM		P9305AM	P9697AM	P8954AM	P9697AM	
Soil Ammend.	Buffer	N		N		Buffer	N			N	Buffer	N		N		Buffer
		25 M	🟥	29 M	🟥		33 M	🟥	🟥	37 M		41 M	🟥	45 M	🟥	
		26 BM		30 BM			34 BM			38 BM		42 BM		46 BM		
		27 B		31 B			35 B			39 BC		43 B		47 B		
		28 C		32 C			36 C			40 C		44 C		48 C		
Rep 3																
Plot		301	302	303	304		305	306	307	308		309	310	311	312	
Irrigation		Limited					Full					Drought				
Hybrid		P9697AM	P8954AM	P9305AM	P9697AM		P9305AM	P9697AM	P9697AM	P9697AM		P9305AM	P9697AM	P8954AM	P9697AM	
Soil Ammend.	Buffer		N	N		Buffer	N		N		Buffer	N		N		Buffer
		🟥	49 B	53 B	🟥		57 B	🟥	61 B	🟥		65 B	🟥	69 B	🟥	
			50 M	54 M			58 M		62 M			66 M		70 M		
			51 BM	55 BM			59 BM		63 BM			67 BM		71 BM		
			52 C	56 C			60 C		64 C			68 C		72 C		
Rep 4																
Plot		401	402	403	404		405	406	407	408		409	410	411	412	
Irrigation		Limited					Full					Drought				
Hybrid		P9305AM	P8954AM	P9697AM	P9697AM		P9697AM	P9675AM	P9697AM	P9697AM		P9697AM	P9697AM	P9305AM	P8954AM	
Soil Ammend.	Buffer	N	N			Buffer			N	N	Buffer			N	N	Buffer
		73 M	77 M	🟥	🟥		🟥	🟥	81 M	85 M		🟥	🟥	89 M	93 M	
		74 BM	78 BM						82 BM	86 BM				90 BM	94 BM	
		75 B	79 B						83 B	87 B				91 B	95 B	
		76 C	80 C						84 C	88 C				92 C	96 C	

Full Site	**Main Plots (Irrigation x Hybrid)**	**Sub-Plots (Soil Ammendment)**	**NP**
270' x 450 ' (82 m x 137.16 m) (108 rows)	15' x 90' (4.6 m x 27.43 m) (6 rows)	15' x 15' (4.5 m x 4.5 m)	5TE
2.79 acres (1.13 ha)	0.031 acres (0.013 ha)	0.005 acres (0.002 ha)	NP and 5TE

Figure 2.4. CSU ARDEC 2015 Treatments and Instrumentation

Table 2.4. ARDEC field 1070 2015 Key Dates

Event	Date	Full Irrigation (mm)	Limited Irrigation (mm)	Drought (mm)
Planting	15 May 2015	-	-	-
Emergence	31 May 2015	-	-	-
Tassel	21 July 2015	-	-	-
Irrigation 1	16 July 2015	25.4	-	25.4
Irrigation 2	23 July 2015	25.4	-	-
Irrigation 3	31 July 2015	25.4	25.4	-
Irrigation 4	06 August 2015	25.4	25.4	-
Irrigation 5	14 August 2015	25.4	25.4	-
Irrigation 6	20 August 2015	25.4	25.4	-
Irrigation 7	28 August 2015	25.4	25.4	-
Irrigation 8	03 September 2015	25.4	25.4	-
Irrigation 9	11 September 2015	25.4	25.4	-
Irrigation 10	18 September 2015	25.4	25.4	-

2.2.2. Instrumentation and Data Collection

During the summer 2015 growing season, the physical conditions at ARDEC 1070 were monitored utilizing soil water sensors, gravimetric sampling, Colorado Agricultural Meteorological Network (COAGMET) weather station and ground-based RS. The ground-based data collected from ARDEC field 1070 were used in comparison with the Tempest UAS derived RS raw data, ET_a and SWD.

2.2.2.1. SWC and SWD Data Collection

The SWC was primarily measured throughout the season using the following sensors: neutron moisture meter (NP) (503DR AM-241, CPNInstrotek, Concord, CA) and a Capacitance (5ET, Decagon Devices Inc., Pullman, WA) SWS. The SWC from the SWSs were used to track the SWB of the irrigation treatment on the daily and seasonal basis. In order to increase the accuracy of the SWS, site specific calibration of the SWS were developed using the gravimetric SWC as described in Chapter 1.

Weekly SWC was measured using forty-eight NP access tubes dispersed throughout the twelve plots. In each plot, NP access tubes were place in four of the control subplots. The NP layout of ARDEC 1070 is shown in Figure 2.4. NP measurements were taken to a depth of 152 cm at an interval of 30.48 cm. For this study, the maximum root zone depth was assumed to be 152 cm. According to Huisman et al. (2003), the accuracy range for NPs are typically between 0.01 and 0.024 mm/m when calibrated using gravimetric SWC [Huisman et al., 2003]. The NP data collection corresponded with aerial RS campaign dates. The SWC was used to estimate the SWD used in the comparisons with the Tempest derived SWD.

Hourly SWC was measured using forty Decagon 5TE capacitance SWSs. The 5TE SWSs were installed in twenty locations throughout the ARDEC 1070 study site (as shown in Figure 2.4). The sensors were installed in pairs, at depths of fifteen and forty-five cm. The 5TE SWS measured the SWC at one hour intervals throughout the growing season. The published accuracy range of the 5TE is between 0.01 and 0.03 mm/m when calibrated using the gravimetric SWC [5TE Manual].

Site-specific calibrations for the NP and 5TE SWS were developed using the Gravimetric SWC method as described by Varble et al. (2011). The gravimetric sampling was conducted twice during the 2015 growing season [Varble et al., 2011]. During each sampling session, six samples were taken to a depth of 150 cm. Half of the samples were taken in the fully irrigated treatments and the other half were taken in the drought treatments. The gravimetric method has an accuracy between 0.01 and 0.024 mm/m (approximately 0.3% of volumetric SWC) [Topp et al., 2002].

The meteorological data, used for the FAO-56 SWB was obtained from the on-site COAGMET weather station (CSU ARDEC – FTCO3, 105° N 40.6525° W, Elevation 1551 m, www.coagmet.com). The COAGMET Station is approximately 288 meters to the south east of ARDEC 1070 and provides hourly meteorological data for the ARDEC complex. The available ground-based data for ARDEC field 1070 are described in Table 2.5.

Table 2.5. ARDEC 1070 Ground Data Collection Dates for comparison with Tempest UAS RS

Date	Multispectral	Thermal	Neutron Probe	Gravimetric Sampling	5TE
22 Jul 2015	X	X	X		X
27 Jul 2015			X	X	X
30 Jul 2015	X	X	X		X
13 Aug 2015	X	X	X	X	X
19 Aug 2015	X	X			X
20 Aug 2015			X		X
10 Sep 15	X	X	X		X

2.2.2.2. Remote Sensing Data Collections

Ground-based RS data collection at ARDEC 1070 were conducted utilizing the following sensors: multispectral sensor (MSR5, CROPSCAN Inc., Rochester, MN) and an infrared thermometer (IRT) (SI-212, Apogee Instruments Inc., Santa Monica, CA). The spectral reflectance (%) was measured using the MSR5, while the surface temperature (T_{sfc}) was calculated using the IRT (^{o}C).

The MSR5 is a Landsat equivalent, hand held radiometer (multispectral) that measures the incoming and reflected irradiance flux of the blue (450-520 nm), green (520-600 nm), red (630-690 nm), NIR (760-900 nm) and TIR (1550-1750 nm) bands of the electromagnetic spectrum [MSR 5 Manual]. The IRT is a hand-held infrared thermometer that is integrated with the MSR5 system (nadir looking) and collects over the TIR (800-1400 nm) band [IRT Manual]. The spectral reflectance and surface temperature measurements were taken weekly, under mostly clear sky conditions, corresponding with the Tempest UAS and USU RS campaigns.

Data collection with the MSR5 and IRT occurred over multiple surfaces for comparison with the aerial RS data. The first surface was the white lambertian reference target (Spectralon 24” x 24” White Target, Labsphere, North Sutton, NH). The second reference target was a black surface, comprised of flat black paint and plywood. Additionally, data collection occurred over at least 10 selected sub-plots and bare soil during every RS overpass for further comparison with the aerial RS data. The ground-based RS data collected throughout the sub-plots were taken over the NP access tube locations. Appendix 1 depicts the RS references targets.

2.2.2.3. ARDEC Survey

All measurement and site layout locations were verified using Real Time Kinematic (RTK) Global Positioning System (GPS) surveying methods. The RTK GPS Survey ensures that all locations are geo-referenced to an accuracy of 1 to 2 cm [Rydlund, 2012]. The study required the survey to ensure the correct locations of all measurements used in the comparison of the ground data and aerial RS data.

2.3. Aerial Remote Sensing Campaign

During the summer 2015 aerial RS campaign, CSU, in coordination with USU, conducted three manned RS flights and seven Tempest UAS RS flights over the primary and alternate test locations. The aerial RS flights were multi-disciplinary operations that involved ground and aerial activities. All aerial RS operations were conducted concurrently with ground-based data collection operations. The CSU Tempest conducted five RS flights at CSU ARDEC, one at CSU AVRC (18 September 2015) and one at NWCG (23 September 2015). The USU manned aircraft conducted three flights covering CSU ARDEC, USDA-ARS LIRF and NWCG. The USU flights were conducted in conjunction with the CSU Tempest for the ARDEC flights. The available data from the 2015 RS campaign are described in Table 2.6.

Table 2.6. CSU and USU Aerial Remote Sensing Flights and Data Available

Available Remote Sensing Data - CSU ARDEC Field 1070					
		Tempest		USU	
Date	Location	Multispectral	Thermal	Multispectral	Thermal
22-Jul-15	ARDEC	🟩 X	-	-	-
30-Jul-15	ARDEC	🟩 X	-	🟩 X	X
13-Aug-15	ARDEC	🟩 X	🟩 X	-	-
19-Aug-15	ARDEC	-	X	X	X
10-Sep-15	ARDEC	🟩 X	🟩 X	X	X
18-Sep-15	AVRC	X	X	-	-
23-Sep-15	NR	X	X	-	-
🟩 Data used in study					

The primary flight location was the ARDEC field 1070. The RS campaign included ground collection operations and flight operations. The flight team consisted of the primary and alternate pilots, who were responsible for the flight, airspace control and aerial RS data collection. The primary launch and recovery location was located on an alfalfa field approximately 800 meters to the west of ARDEC 1070. During the 2015 RS campaign, the CSU Tempest maintained a flight level of between 91 and 121 m and a flight speed between 17 and 19 meters per second (m s^{-1}) to ensure safe operations and maintain a spatial resolution of 12 cm or less. The USU manned aircraft maintained a flight level of 365 meters and maintained a spatial resolution of 0.5 meters (1.8 m for the TIR). Appendix 4 contains the Tempest and USU data.

In order to collect pertinent data, all flights occurred between 1000 and 1300 Mountain Standard Time (MST) and under mostly clear sky conditions.

The CSU Tempest UAS collected high resolution, spatially distributed multispectral imagery of the test location. The multispectral imagery (NIR, red and green) have a spatial (pixel) resolution of approximately 6.5 cm. The multispectral imagery was processed using the factory provided software (Pixelwrench2, Tetracam Inc., Chatsworth, CA) and was reported as spectral reflectance (%). The multispectral imagery are provided as a geo-referenced, false color image (RGB) of the NIR, red and green bands (red – NIR, green – red, blue – green) (Figure 2.5). The thermal (TIR) imagery have a spatial (pixel) resolution of approximately 11.76 cm. The thermal imagery were processed using the factory provided software (Thermalviewer, TeAx Technology UG, Wilnsdorf, Germany) and were reported as ^{o}C. The thermal imagery were provided as a geo-referenced, monochromatic images scaled between the maximum and minimum scene temperatures (Figure 2.6). The VIS (red, green, and blue) imagery have a spatial (pixel) resolution of approximately 9.5 cm. The VIS imagery were provided as a geo-referenced RGB image (Figure 2.7). All RS imagery were geo-referenced and processed using ERDAS Imagine 2015 geographic information system (GIS) software [ERDAS Imagine 2015, Hexagon Geospatial, Cape Town, South Africa]. The pre-preprocessed data were geo-rectified using the RTK surveyed ground control points and the ERDAS Imagine GIS software. At least ten ground reference points for each RS image in order to ensure proper alignment of all RS imagery and ground-based data. Mosaicking of the geo-rectified using the ERDAS Imagine GIS software. During the CSU Tempest RS overpasses, data collection occurred with approximately 70% image overlap, both horizontally and vertically, to ensure acceptable data was obtained of field 1070.

The USU manned aircraft acquired high resolution images in the VIS, NIR, and TIR bands of the electromagnetic spectrum. The USU RS payload consisted of three Kodak Megaplus digital frame cameras (green: 545-560 nm; red 665-680 nm; NIR: 795-809) (Eastman Kodak Company, Rochester, NY) and a thermal infrared camera (TIR: 800-1200 nm) (Inframetrics 760, Inframeterics, N. Billerica, MA). The VIS and NIR has a spatial (pixel) resolution of 0.5 m (Figure 2.8) and the TIR has a resolution of 1.8 m (Figure 2.9) at the 395 m AGL flight level [Chávez et al., 2012]. The USU data were processed using the ERDAS Imagine 2015 software. The USU data supplemented data missing from the Tempest UAS and to provide aerial RS imagery over the LIRF-ATM.

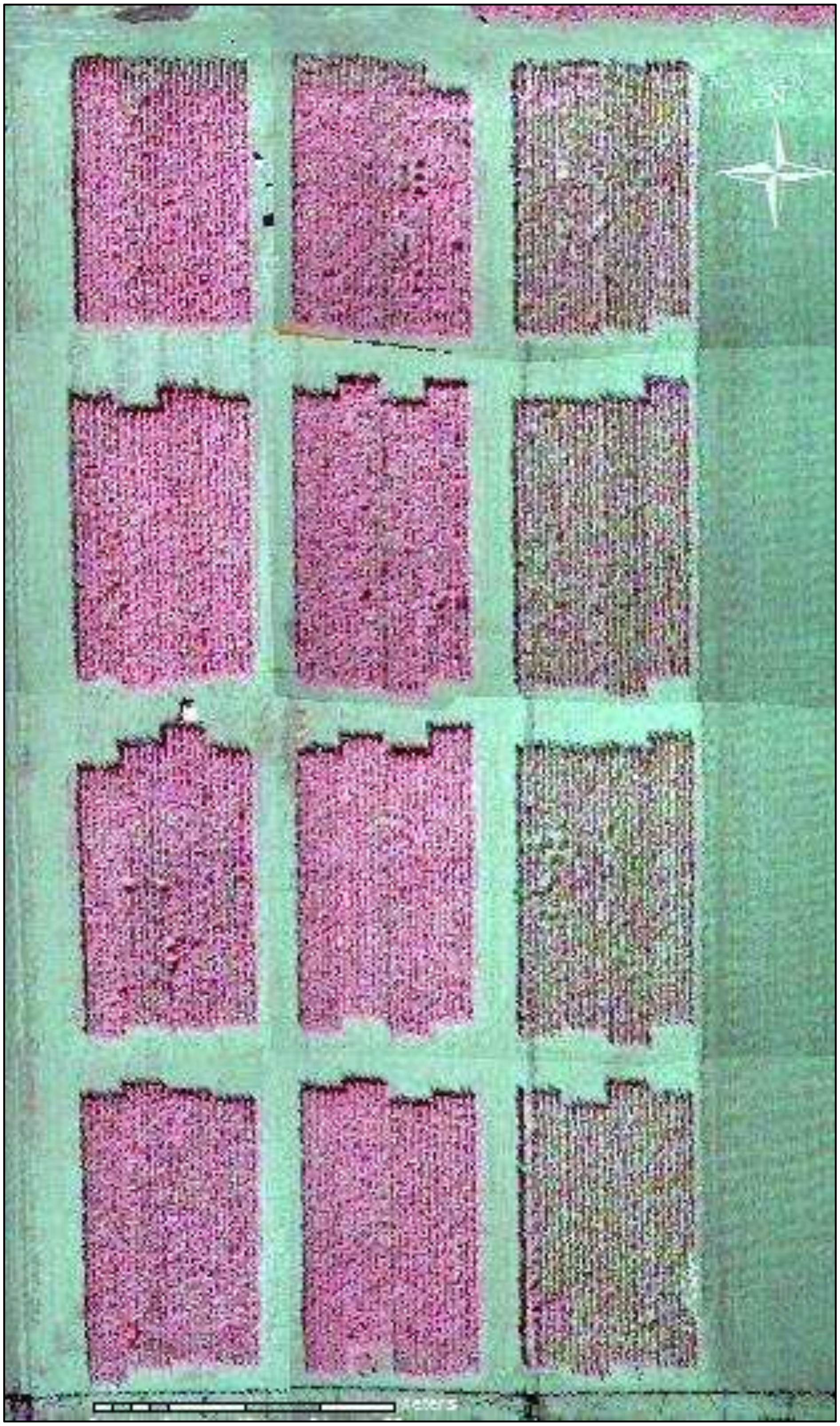

Figure 2.5. 10 September 2015 CSU Tempest false color multispectral (NIR, red, green) imagery (121 m AGL with a spatial resolution of 6.5 cm) of ARDEC Field 1070 using the Tetracam Snap ADC multispectral sensor.

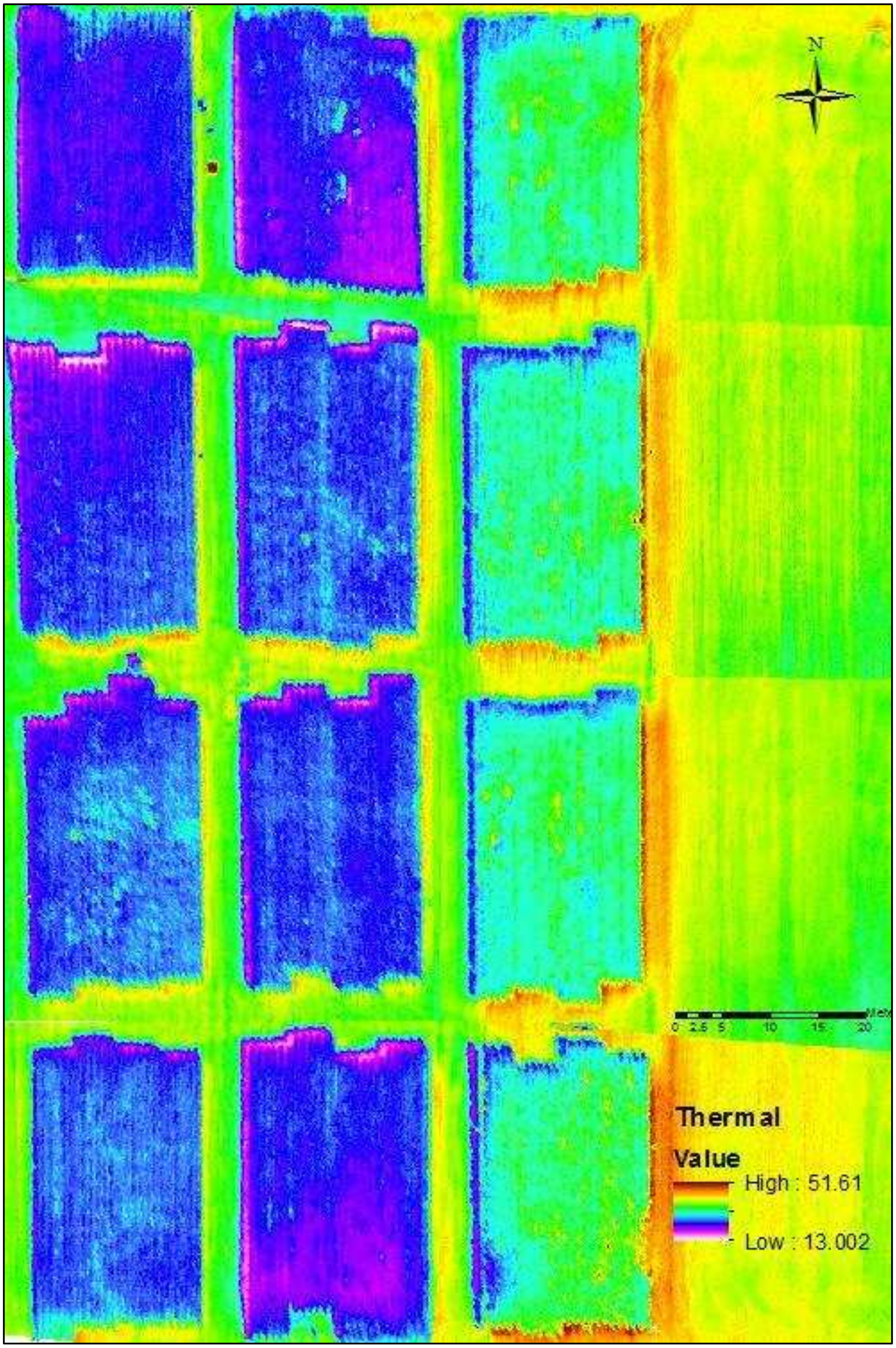

Figure 2.6. 10 September 2015 CSU Tempest false color TIR imagery (121 m AGL with a spatial resolution of 11.76 cm) of ARDEC field 1070 using the FLIR Tau 2 640 thermal sensor.

Figure 2.7. 13 August 2015 CSU Tempest visual (RGB) imagery (121 m AGL with a resolution of 9.5 cm) of ARDEC field 1070 using the Sony A600 SRL digital camera. The shadow is a result of non-optically calibrated data.

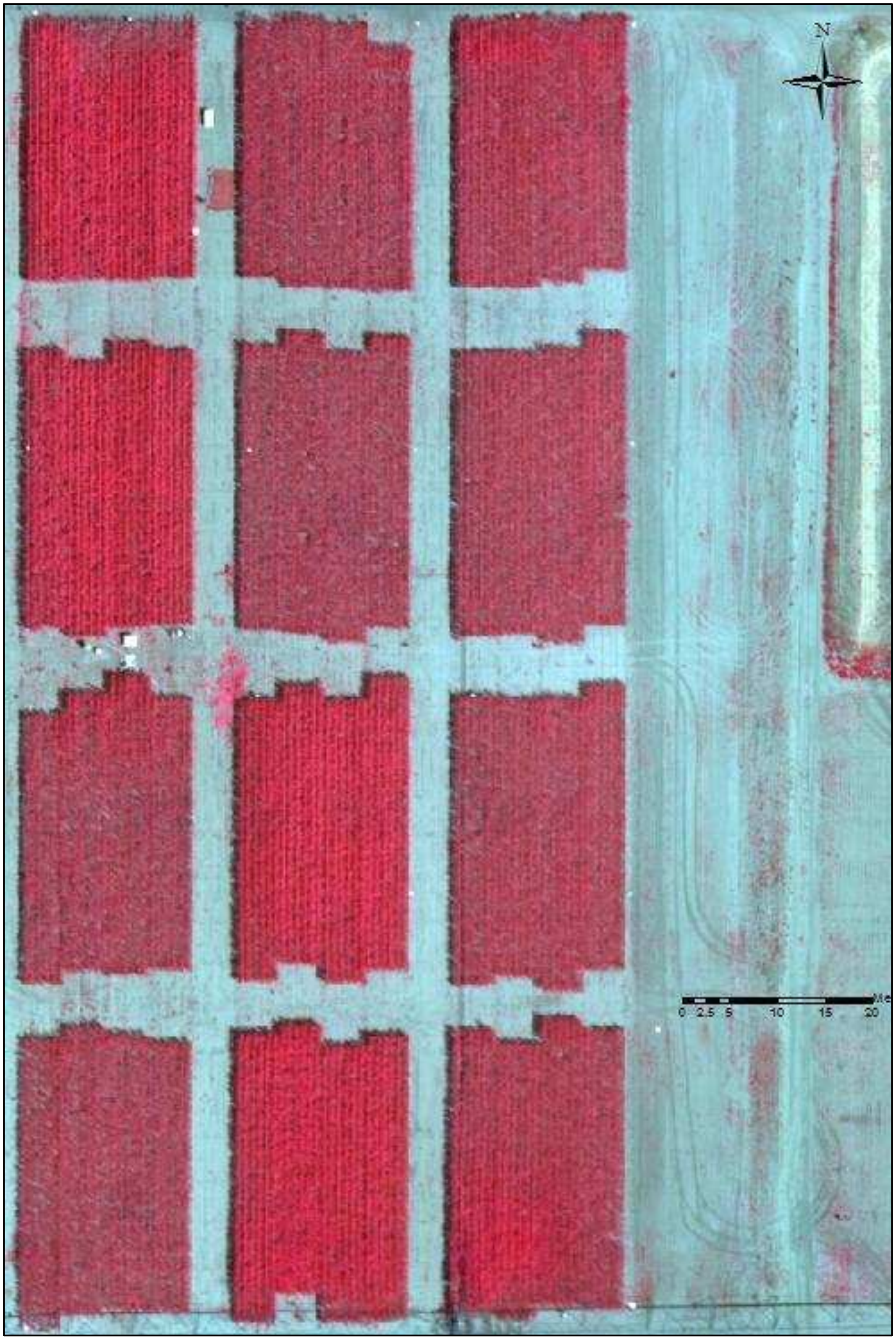

Figure 2.8. 30 July 2015 USU false color multispectral imagery (365 m AGL with a spatial resolution of 50 cm) of ARDEC Field 1070 using the Kodak Megaplus digital frame cameras.

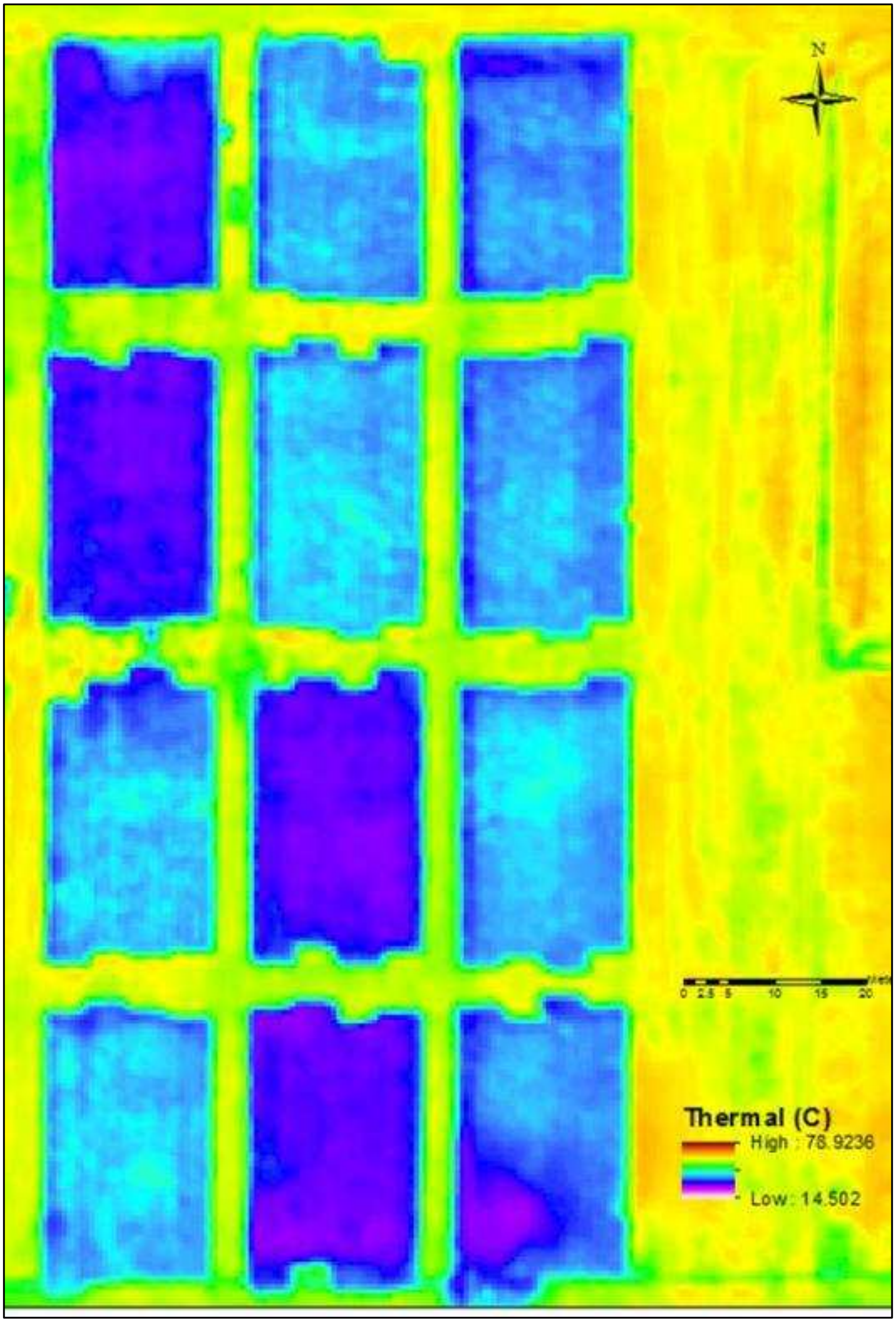

Figure 2.9. 10SEP15 2015 USU false color TIR Imagery (365 m AGL with a spatial resolution of 1.8 m) of ARDEC field 1070 using the Inframetrics 760 thermal sensor.

2.4. Data Analysis and Comparison Methodology

The data analysis and comparison of the study consists of two parts. The first analysis was between the raw multispectral and thermal data collected through the ground (MSR5 and IRT) RS and aerial (Tempest UAS) based remote sensing. The second part consisted of the comparison of the four aerial RS derived ET_a methods and Hybrid derived SWD to the NP and FAO-56 SWB derived ET_a and SWD. The RS derived SWD were derived using the most appropriate ET_a method utilizing the Hybrid model developed by Neale et al. 2012.

2.4.1. CSU Tempest UAS Raw RS Data

The Tempest raw RS data were directly compared to the data collected on the ground with the MSR5 multispectral scanner. During the overpasses, the ground team collected multiple data sets from each treatment, the white and black references, bare soil, grass and water. Due to the settings of the internal calibration of the sensors on the Tempest, the water, white and black references were not used for the evaluation. A minimum of ten locations, spread throughout the test site, were selected for use in the evaluation against the Tempest RS data.

2.4.2. ET_a Models

The study focused on deriving ET_a from aerial RS imagery (NIR, red, green and TIR). The multispectral (NIR, red and green) and thermal (TIR) imagery collected from the Tempest and USU manned aircraft were used to derive spatially distributed ET_a using four methods. The methods include both single and two-sourced surface energy balance models as well as reflectance and thermal-based models. All of the methods were developed for vegetative surfaces and do not accurately depict the ET of bare soil. The four methods of calculating ET_a are as follows:

1) Two-Source Energy Balance Method.

2) Surface Aerodynamic Temperature Method.

3) Crop Water Stress Index.

4) Reflectance-based Crop Coefficients.

The hourly ET_a (mm/h) calculated using each method were extrapolated to the daily ET_a (mm/d) using Eq. (1.10) and Eq. (1.11). The extrapolation method, ET_rF, remained constant across the methods to prevent additional error while comparing the methods. All of the models were processed using the ERDAS Imagine 2015 GIS software and models created in the Spatial Model Builder program.

2.4.2.1. Surface Energy Balance Methods

In the SEB methods (TSEB and SAT), the R_n are calculated as the sum of the incoming and outgoing long and short wave radiation, with inputs from VIS, NIR and TIR RS data, as well as physical and meteorological variables. [Monteith, 1973].

$$R_n = (1-\alpha)R_S + \varepsilon_a \sigma T_a^4 - \varepsilon_S \sigma T_{sfc}^4 \tag{2.1}$$

where α is the surface albedo, R_s is the incoming short wave radiation (W m^{-2}), ε_a is the emissivity of the air, σ is the Stefan-Boltzmann constant (5.67xE-08, W m^{-2} K^{-4}), T_a is the air temperature (K), ε_s is the surface emissivity, and T_{sfc} is the radiometric surface temperature (K).

The G is calculated as a function of R_n, TIR RS data and VI's [Bastiaanssen et al., 1998]. A common method of estimating G utilizing RS is described in Chávez et al., 2005.

$$G = (((0.3324 + (-0.024 LAI)) \times (0.8155 + (-0.3032 \ln(LAI)))) \times R_n) \tag{2.2}$$

where LAI is the leaf area index (m^2 m^{-2}) and is calculated using the NIR and red RS spectral reflectance data [Anderson et al., 2005]:

$$LAI = (4 \times OSAVI - 0.8) \times (1 + 4.73 \times 10^{-6} \times e^{15.64 \times OSAVI}) \tag{2.3}$$

where OSAVI is the Optimized Soil Adjusted Vegetation Index [Rondeaux et al., 1996]:

$$OSAVI = \frac{(1+L)(NIR - RED)}{NIR + RED + L} \tag{2.4}$$

In all of the SEB models, the methods of calculating H are different, but all revolve around a measure of the difference (dT, K) in aerodynamic temperature (T_o, K) (or radiometric surface temperature (T_{sfc}, K)) and air temperature (T_a, K), and the aerodynamic resistance to heat transfer (r_{ah}, s m^{-1}).

$$H = \frac{\rho_a \times Cp_a \times (dT)}{r_{ah}} \tag{2.5}$$

where ρ_a is the moist air density (kg m^{-3}), Cp_a is specific heat of dry air (J kg^{-1} K^{-1}). The r_{ah} is dependent on the crop characteristics and atmospheric conditions. The r_{ah} are corrected for atmospheric stability conditions utilizing the Monin-Obukhov similarity theory [Monteith and Unsworth, 1990]. The atmospheric stability correction follows the iterative process outline by Chávez et al. (2005).

$$r_{ah} = \frac{\ln(\frac{Z_m - d}{Z_{oh}}) - \psi_h(\frac{Z_m - d}{L_{mo}}) + \psi_h(\frac{Z_{oh}}{L_{mo}})}{u_* k} \tag{2.6}$$

where Z_m is the height of the wind speed measurement (m), d is the zero-plane displacement height (m), Z_{oh} is the roughness length for heat transfer (m), ψ_h is the stability correction factor for atmospheric heat transfer, L_{mo} is the Monin-Obukhov atmospheric stability length scale (m), u_* is the friction velocity (m s^{-1}) and k is the von Karman constant (0.41). The Z_m, d, and Z_{oh} are a function of the canopy height, which can be estimated using RS or based on physical measurements.

2.4.2.1.1. Two-Source Energy Balance Model (TSEB)

The TSEB [Neale et al., 2012], as discussed previously, computes the components of the surface energy balance, net radiation (R_n), soil heat flux (G), and sensible heat flux (H), separately for the canopy and the soil components of a RS image. The fluxes are computed using the high spatial (pixel) resolution aerial RS imagery (NIR, red, green and TIR). The TSEB is an iterative method that calculates the initial fluxes and then corrects H and the aerodynamic resistance to heat transfer (r_{ah}). The TSEB requires the NIR, red, green, blue and TIR bands (Post et al., 2000) to estimate the instantaneous LE. In order to separate the soil component from the canopy, OSAVI is used calculate the LAI [Rondeaux et al., 1996; Chávez et al., 2005]. The vegetation fractional cover (f_c), which is the fraction of the pixel that is vegetation, is then calculated as a function of LAI and the clumping factor (Ω) [Kusta and Norman, 2000]:

$$f_c = 1 - e^{-0.5 \times LAI \times \Omega} \tag{2.7}$$

The f_c is used to calculate the soil and the canopy components of the R_n. The R_n is calculated as the sum of the shortwave and long wave radiation budget using Eq. (2.1) [Monteith, 1973]:

The R_n is separated into the canopy component of R_n using the f_c, and then used to calculate the sensible heat flux for the soil (H_c, W m^{-2}). The H_c, and Monin-Obukhov similarity theory adjusted r_{ah} [Foken, 2006] are used to calculate the canopy temperature (T_c ,°C):

$$T_c = \frac{H_c \times r_{ah}}{\rho_a \times Cp_a} + T_a \tag{2.8}$$

The T_c is then used to estimate the temperature of the soil (T_s, °C) as a function of the T_{sfc}, T_c, and f_c [Norman et al., 1995].

$$T_s = \sqrt[4]{\frac{T_{sfc}^4 - (f_c \times T_c)^4}{1 - f_c}} \tag{2.9}$$

The T_c, T_s, α, air emissivity (ε_a), surface emissivity (ε_s), and LAI are then used to update the net radiation for the soil (R_{n_s}, W m^{-2}) and the canopy (R_{n_c}, W m^{-2}) [Kustas and Norman, 2000]. The canopy (H_c, W m^{-2}) and soil (H_s, W m^{-2}) components of the sensible heat flux (H) are then calculated:

$$H_c = R_{nc} \times (1 - (1.3 \times f_g \times \frac{\Delta}{\Delta + \gamma})) = \frac{\rho_a \times Cp_a \times (T_c - T_a)}{r_{ah}} \tag{2.10}$$

$$H_s = \frac{\rho_a \times Cp_a \times (T_s - T_a)}{r_{ah} + r_s} \tag{2.11}$$

where f_g is the fraction of vegetation that is green, Δ is the slope of the Saturation Vapor Pressure versus temperate curve, and r_s (s m^{-1}) is the resistance to heat flow just above the soil [Norman, 1995]. The G (W m^{-2}) is calculated as a function of the R_n and the LAI using Eq. (2.3) [Chávez et al., 2005]:

The total sensible heat flux (H_t, W m^{-2}) is calculated as the sum of the H_c and H_s:

$$H_t = H_c + H_s \tag{2.12}$$

The total instantaneous LE (LE_t, W m^{-2}) is calculated using Eq. (1.6). The contribution of the soil (LE_s, W m^{-2}) and canopy (LE_s, W m^{-2}) are calculated as a function of their respective energy fluxes:

$$LE_S = R_{n\_s} - H_S - G \tag{2.13}$$

$$LE_C = R_{n\_c} - H_C - G \tag{2.14}$$

The hourly ET_a (ET_{a_h}, mm h^{-1}) are calculated using Eq. (1.7), and the daily ET_a (ET_{a_d}, mm d^{-1}) are calculated using Eq. (1.10) and Eq. (1.11). The final spatial resolution of the TSEB ET_a was determined utilizing the TIR imagery's resolution (11.76 cm). The TSEB process is described in detail in Appendix 3.

2.4.2.1.2. Surface Aerodynamic Temperature Model (SAT)

The SAT Model is a single source SEB method that models the spatially distributed aerodynamic temperature (T_o, K) as a function of T_s, T_a, LAI, wind speed (u, m s^{-1}) and r_{ah} [Chávez et al., 2005]. The SAT requires the same RS data as the TSEB model. The sensible heat flux (H), corrected for atmospheric stability, is calculated using the T_o:

$$H = \frac{\rho_a \times Cp_a \times (T_o - T_a)}{r_{ah}} \tag{2.15}$$

where T_o is modeled as [Chávez et al., 2005]:

$$T_o = (0.534 \times T_{sfc}) + (0.39 \times T_a) - (0.224 \times LAI) - (0.192 \times U) - 1.67 \tag{2.16}$$

The R_n is calculated using Eq. (2.1) and the G is calculated using Eq. (2.2). The instantaneous LE (LE, W m^{-2}) is calculated as the residual of the surface energy balance equation:

$$LE = R_n - G - H \tag{2.17}$$

The hourly and daily ET_a are calculated using Eq. (1.7) and Eq. (1.10) thru Eq. (1.11). The final spatial resolution of the SAT ET_a were determined utilizing the TIR imagery's spatial resolution (11.76 cm). The SAT process is described in detail in Appendix 3.

2.4.2.3. Crop Water Stress Index Model (CWSI)

The CWSI model [Idso et al., 1981] utilizes the spatially distributed TIR imagery and meteorological data to derive a crop coefficient used in scaling the ASCE-EWRI reference ET. The CWSI is calculated using the following equation:

$$CWSI = \frac{dT - dT_{ll}}{dT_{ul} - dT_{ll}} \tag{2.18}$$

where dT (K) is the difference between the individual pixel T_c (K) and the T_a (K) from the RS TIR imagery and weather station data. In this study, the procedure for calculating dT differed from the method describe by Idso et al., 1981. The CWSI model was originally developed using hand held infrared thermometers (ground-based RS) measuring T_c perpendicular to the crop in order to avoid any soil background temperature effects. While using the UAS data the radiometric surface temperature (T_{sfc}) were used instead of T_c in order to produce the spatially distributed ET_a utilizing the TIR RS Imagery alone.

$$dT = T_{sfc} - T_a \tag{2.19}$$

where dT_{ll} (K) is a function of the site specific coefficients and the VPD:

$$dT_{ll} = a(VPD) + b \tag{2.20}$$

where a is -1.97 and b is 3.11 for semi-arid corn [Idso et al., 1982] and the VPD is calculated as the difference between the saturation vapor pressure of air (e_s kPa) and the actual vapor pressure of the air (e_a, kPa) [Idso et al., 1982]:

$$VPD = e_s - e_a \tag{2.21}$$

dT_{ul} (K) is a function of the site specific coefficients and the vapor pressure gradient (VPG) [Idso et al., 1982]:

$$dT_{up} = a(VPG) + b \tag{2.22}$$

where the VPG is the difference between the vapor pressure at air temperature and at a higher temperature of T_a plus the coefficient b [Idso et al., 1982]:

$$VPG = e_s(T_a) - e_s(T_a + b) \tag{2.23}$$

The spatially distributed ET_a are calculated using the CWSI as a reduction coefficient and the potential ET (ET_p, mm h^{-1}), or crop non-water stressed ET, with the following equation [Idso et al., 1982]:

$$ET_a = (1 - CWSI) \times ET_p \tag{2.24}$$

where ET_p calculated from the reference ET and the basal crop coefficient:

$$ET_p = k_{cb} \times ET_{ref} \tag{2.25}$$

The CWSI method is depicted in Figure 2.10. The horizontal line is the dT_{ul} (max stress) and the lower line is the dT_{ll} (min stress) [Idso et al., 1982]. The hourly ET_a (mm h^{-1}) is calculated using the CWSI, and the ET_p from Eq. (1.10) and Eq. (1.11). The final spatial resolution of the CWSI ET_a were determined utilizing the TIR imagery's spatial resolution (11.76 cm). The CWSI process is described in detail in Appendix 3.

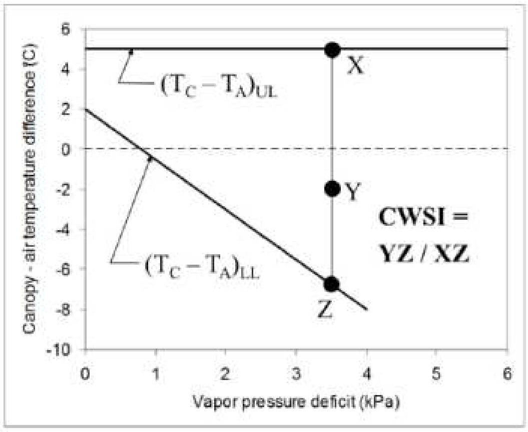

Figure 2.10. Graphically depicted CWSI [Idso et al., 1982]

2.4.2.4. Reflectance-based Crop Coefficients Model (k_{cbrf})

The reflectance-based crop coefficients model [Neale et al., 1989; Bausch, 1993] utilize the spatially distributed Tempest UAS RS NIR and red imagery. The k_{cbrf} describes the relationship between the ASCE-EWRI reference ET and the crop ET_a:

$$ET_a = k_{cbrf} \times ET_{ref} \tag{2.26}$$

The reflectance-based crop coefficient method assumes a linear relationship between the RS derived VI's and k_{cbrf}. Two methods of deriving k_{cbrf} were used in this study. The first method used the relationship, developed by Neale et al. (1989), for corn in Greeley, CO. This method utilizes the RS derived NDVI:

$$NDVI = \frac{NIR - RED}{NIR + RED} \tag{2.27}$$

$$k_{cbrf} = 1.181(NDVI) - 0.026 \tag{2.28}$$

The second method derives the k_{cbrf} using the RS derived f_c [Trout et al. 2008; Johnson and Trout, 2012].

$$k_{cbrf} = 1.13 \times f_c + 0.14 \tag{2.29}$$

The methodology used for calculating the f_c in the study differs from the Johnson and Trout (2012) method. Instead of using the linear relationship between NDVI and f_c, the f_c were derived using Eq. (2.7). The deviation was to limit the error associated with calculating similar terms differently throughout the models. The daily ET_a are calculated using (1.10) and Eq. (1.11). The final spatial resolution of the reflectance-based ET_a were determined utilizing the Tetracam ADC SNAP imagery's spatial resolution (6.9 cm). The k_{cbrf} process is described in detail in Appendix 3.

2.4.3. Hybrid Soil Water Content Model

In order to estimate the root zone SWD, the Hybrid SWC model [Neale et al., 2012], was implemented using the NDVI derived k_{cbrf} and the most accurate ET_a derived from the four models described. The Hybrid SWD model tracks the growing season SWD by using the FAO 56 SWB method, with the SWD and k_{cb} updated periodically with the Tempest UAS RS derived ET_a and k_{cbrf}. The procedure of the Hybrid SWC is located in Appendix 3.

The FAO-56 SWB is used in multiple processes of the hybrid model. The first use is the tracking of the daily SWD for use with a PA irrigation system [Neale et al., 2012]. The FAO-56 SWB approach starts with a given soil profile at field capacity (θ_{FC}, mm m^{-1}) or measured volumetric SWC [Allen et al., 1995]. Field capacity is generally defined as the amount of water held in the soil after excess water has drained away and the rate of downward drainage has decreased. Once the SWB begins, the root zone SWDs are tracked using the following equation [Allen et al., 1995]:

$$D_i = D_{i-1} + ET_a - (P - SRO) - I_n + DP - GW \tag{2.30}$$

Where D_i (mm) is the soil water depletion at the end of day i, D_{i-1} is the soil water depletion at the end of day i-1 (mm), ET_a is the actual crop evapotranspiration (mm), P (mm) is the gross precipitation, SRO (mm) is the surface runoff, I_n (mm) is the net irrigation on day i, DP (mm) is the deep percolation on day i, and GW (mm) is the ground water capillary contribution from the water table on day i [Hoffmann et al., 2007]. The initial SWD for ARDEC field 1070 was estimated using the NP SWS on 29JUN2015. The SWD is defined as the difference between the θ_{fc} and the SWC at day i (θ_i) [Neale et al., 2012]:

$$SWD_{Di} = (\theta_{FC} - \theta_i) \times R_z \tag{2.31}$$

The second use is the estimation of the SWB ET (ET_{WB}) and the components of the dual crop coefficient, k_s and k_e. The components of the dual crop coefficient are calculated based on the soil characteristics and water status [Neale et al., 2012]. The stress coefficient, k_s, according to Allen et al. (1995) is calculated as:

$$k_S = \frac{TAW - D_r}{TAW - RAW} \tag{2.32}$$

where TAW is the total available water (mm), D_r is the root zone depletion (mm), and RAW is the readily available water (mm). The TAW is calculated as the water available between the θ_{FC} and the θ_{WP}. The RAW is the portion of the TAW that a crop can extract from the soil root zone without experiencing stress. The TAW, D_r and RAW are depicted in Figure 2.10. When D_r < RAW, k_s is 1 and there is no water stress. When TAW > D_r > RAW, k_s ranges from 0 (maximum water stress) to 1 [Allen et al., 1995].

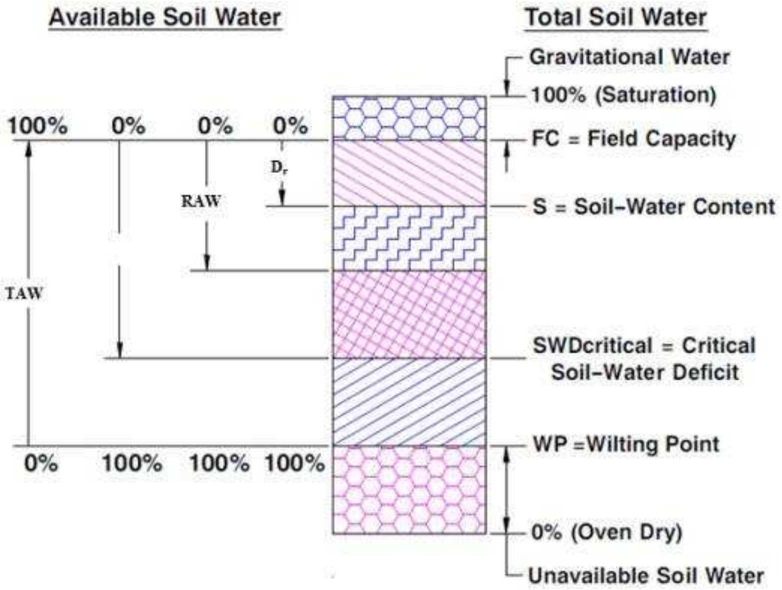

Figure 2.11. Available soil water adapted from Steele et al. (2010).

The shallow soil water evaporation coefficient, k_e, is calculated using the following equation:

$$k_e = k_r (k_{c\max} - k_{cb}) \leq f_{ew} \times k_{c\max} \qquad (2.33)$$

where, k_r is the evaporation reduction coefficient, $k_{c\max}$ is the maximum value of k_c following a wetting event, and f_{ew} is the fraction of soil that receives sunlight, and water during the wetting event [Allen et al., 1995]. An in-depth discussion of the application of the FAO 56 SWB can be found in Appendix 3.

The RS derived ET_a and k_{cbrf} are assimilated into the FAO 56 SWB by updating the k_s [Neale et al., 2012]. In order to update the SWD, ET_a is used to calculate the updated stress coefficient, k_s :

$$k_s = \frac{\frac{ET_a}{ET_{ref}} - k_e}{k_{cbrf}} \qquad (2.34)$$

The updated k_s is used to estimate the actual SWD (D_i, mm) by using the linear relationship between the k_s, readily available water (RAW, mm) and total available water (TAW, mm) as shown in Figure 2.11. If the Hybrid model derived $k_s = 1$, $D_i < \text{RAW}$. If $k_s < 1$, then the D_i is a function of the linear relationship between RAW ($K_s = 1$) and TAW ($k_s = 0$) [Allen et al., 1995]. In the terms of a PA irrigation system, if the $D_i<\text{RAW}$, irrigation is not required. If $D_i > \text{RAW}$, irrigation is required [Allen et al., 1995].

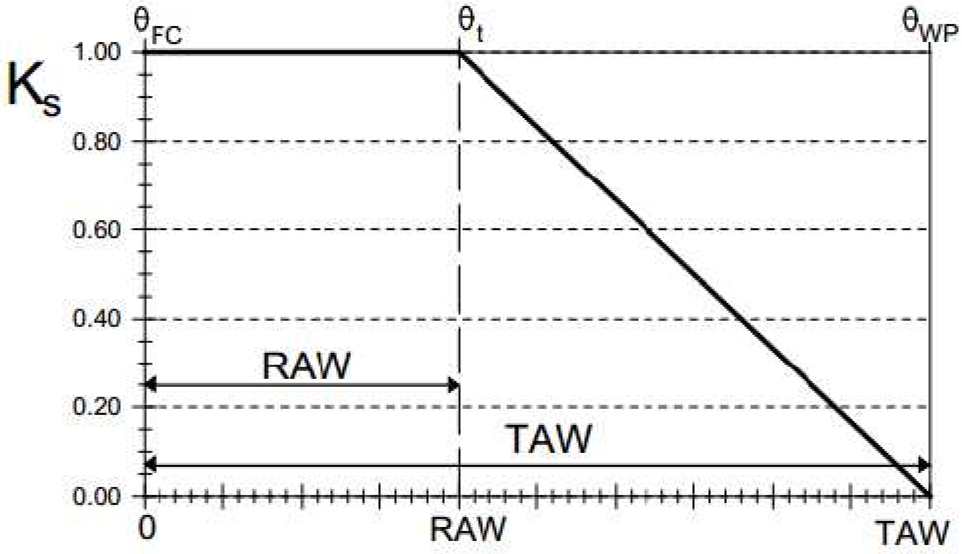

Figure 2.12. Relationship between k_s, RAW and TAW [Allen et al., 1995]

The actual SWC (θ_i mm) is updated using the D_i, θ_{FC} and R_z:

$$D_i = (\theta_{FC} - \theta_i) \times R_Z \tag{2.35}$$

$$\theta_i = \theta_{FC} - \frac{D_i}{R_z} \tag{2.36}$$

The k_{cbrf} is then used to adjust the k_{cb} in the SWB between RS overpasses. By adjusting k_{cb} based on the actual crop characteristics, ET_{WB} will more accurately estimate ET_a [Neale et al., 2012]. Figure 2.12 depicts the use of the k_{cbrf} when compared to k_{cb}. Under ideal conditions the k_{cbrf} will closely approximate k_{cb}. Crops that are under non-standard conditions will generally fall below the k_{cb} [Neale et al., 2012]. The final spatial resolution of the Hybrid SWD were determined utilizing the TIR imagery's spatial resolution (11.76 cm).

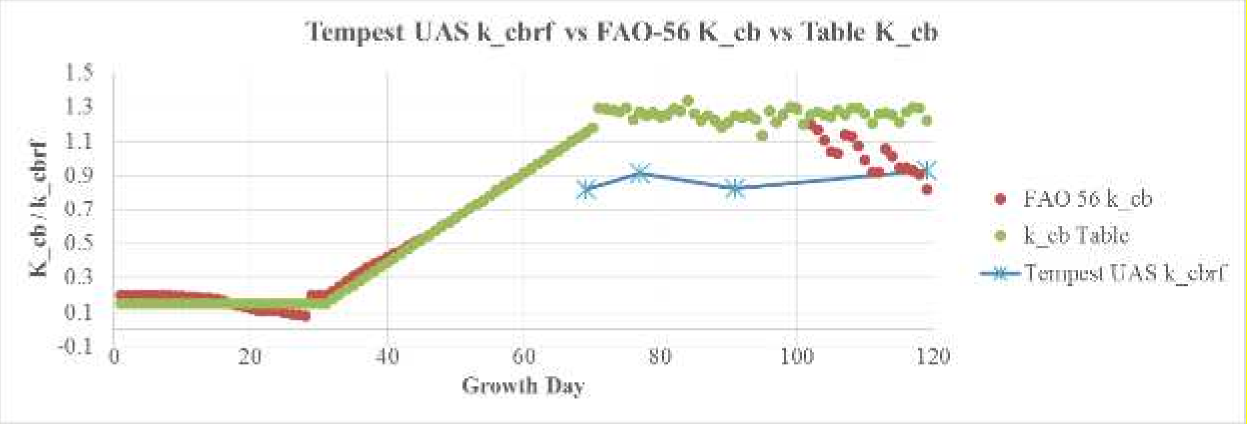

Figure 2.13. Full irrigation treatment k_{cbrf} vs. k_{cb} vs. the tabulated k_{cb} over the growing season at ARDEC field 1070 during the 2015 RS campaign.

2.4.4. Comparison

Two comparisons were conducted using the data collected during the study. The first comparison evaluated the raw Tempest multispectral and thermal imagery versus the ground-based remote sensing data. The purpose of the first comparison was to evaluate quality and suitability of the Tempest RS derived imagery and provide recommendations for future applications of the system. The second comparison evaluated the Tempest UAS RS derived ET_a and SWD against the ET_a and SWD calculated by the NP and the FAO 56 SWB. The purpose of the second comparison was to evaluate the most appropriate RS derived ET_a method for use with the hybrid model, and evaluate the accuracy of the Tempest RS derived SWD. The objective of the comparisons were to provide recommendations for the application of the Tempest UAS RS data in PA irrigation management systems. All of the comparisons were conducted for each individual overpass and over campaign (all RS overpasses) time frame.

The optical multispectral (red, and green), NIR and TIR imagery collected with the Tempest and USU RS platform were directly compared to the multispectral (NIR, red, green) and thermal (TIR) data collected on the ground over the spatially distributed crop and soil locations.

The four Tempest RS derived ET_a algorithms (TSEB, SAT, CWSI, K_{cb}) and the resulting RS adjusted SWB ET_a were evaluated with the ET_a derived from the NP and the FAO 56 SWB. The Tempest derived SWD, using the most accurate of the RS derived ET_a, was evaluated with the SWD measured using the NP and the FAO-56 SWB estimates.

The evaluations were conducted using the Mean Bias Error (MBE), the Root Mean Square Error (RMSE), Student T-Test (t) and the Nash-Sutcliffe Model Efficiency Coefficient (NSCE) (Nash et al., 1970). The MBE, RMSE, Student T-Test and NSCE were calculated as follows:

$$MBE = N^{-1} \sum_{i=1}^{N} P_i - O_i \tag{2.36}$$

$$RMSE = \left[N^{-1} \sum_{i=1}^{N} (P_i - O_i)^2 \right]^{0.5} \tag{2.37}$$

$$t = \frac{\bar{X} - \mu}{\frac{s}{\sqrt{N}}} \tag{2.38}$$

$$E = 1 - \frac{\sum (O_i - P_i)^2}{\sum (O_i - \bar{O})^2} \tag{2.39}$$

where N is the number of observations (RS), P is the RS model prediction, O is the ground observation, $\bar{O}$ is observed mean, $\bar{X}$ is the RS mean, μ is the ground-measured mean and s is the standard deviation of the RS data. The MBE describes the models systematic bias error. A positive MBE (MBE>0) suggest a model overestimation, while a negative MBE (MBE<0) suggests a model underestimation. The RMSE is the sample standard deviation of the differences (residuals) between the observed and the predicated. The RSME is a measure of accuracy when comparing multiple models. The NSCE is used to quantitatively describe the predictive accuracy of the models compared to the observed data. A positive E (E>0) suggest that the predicted value more closely approximates the observed data then the mean of the observed data. The Student T-Test is an assessment of the statistical significances of the variance of the sample means (RS data) and the population means (ground data). The T-Test used a significance level (α) of 0.05 to denote statistical significance of the test. The study used a two tailed T-Test that will test whether or not the mean value of the sample (RS) is statistically the same as the mean value of the control (MSR5 or NP). The analysis was conducted using the following equation for a two-tailed paired T-Test:

$$2 \times P[T \leq t] \geq \alpha \tag{2.40}$$

There is significant statistical evidence that the means are statistically the same if the probability is greater than the established α.

CHAPTER 3: RESULTS AND ANALYSIS

The results of the summer 2015 ARDEC field 1070 Tempest UAS remote sensing campaign and the error statistics are discussed in this chapter. The evaluations of all the methods are presented for the individual RS overpasses and the 2015 RS campaign. The accuracy, of the raw RS data, are evaluated using the MBE, RMSE and NSCE. The most appropriate RS ET_a model is identified for the use of the ET method with the CSU Tempest RS platform data. The Hybrid model derived SWDs were evaluated for ARDEC field 1070. A summary of the data and statistics are found in Appendix 4.

3.1 Raw data results and analysis

The 2015 RS campaign was a preliminary study to evaluate the feasibility of using the CSU Tempest UAS to collect RS data for use in estimating the ET_a and SWD of agricultural fields. In order to utilize the Tempest UAS derived RS data in the estimation of the ET_a and SWD, the quality of the raw RS data (NIR, red, green and TIR) were evaluated with the ARDEC field 1070 ground-based MSR5 data multispectral and thermal data. The raw RS data used in this study were only calibrated using the individual sensor’s internal factory calibrations. During the 2015 campaign, the multispectral sensor (TETRACAM ADC SNAP) malfunctioned causing errors to the internal calibration and magnitude of recorded data. The malfunctioning of the multispectral sensor was caused by two coding errors. The first malfunction of the Tetracam resulted from an error in the code responsible for the writing of the data on the storage media. The second malfunction was caused by a coding error that recorded the maximum spectral reflectance instead of the average for a pixel. During the 22JUL15 flight, the multispectral sensor began to intermittently malfunction causing the calibration and the data recording process to produce largely inflated and inconsistent data. The malfunction was responsible for the high spectral reflectance MBE (4.14%) and RMSE (6.98%) of the 22JUL15 overpass. During the two subsequent flights (30JUL15 and 13AUG15) the malfunction only affected the internal calibration of the multispectral sensor. While the ratios of the bands remained same throughout the image, the reported values were of a much greater magnitude than expected (UAS NIR = 77.8 % vs MSR5 NIR= 38.84%). On 19AUG15, the multispectral sensor was inoperable due to the malfunction, and required reprograming by the sensor manufacturer. The final overpass with the Tempest provided adequate accuracy, but had higher levels of error due to the need to update the internal calibration of the sensor. Due to the malfunction with the multispectral sensor, the NIR, red and green imagery for the RS overpasses on 30JUL15 and 13AUG15 were scaled to adjust the magnitude of the data, as depicted in Figure 3.1. The corrections for both overpasses are described in Table 3.1.

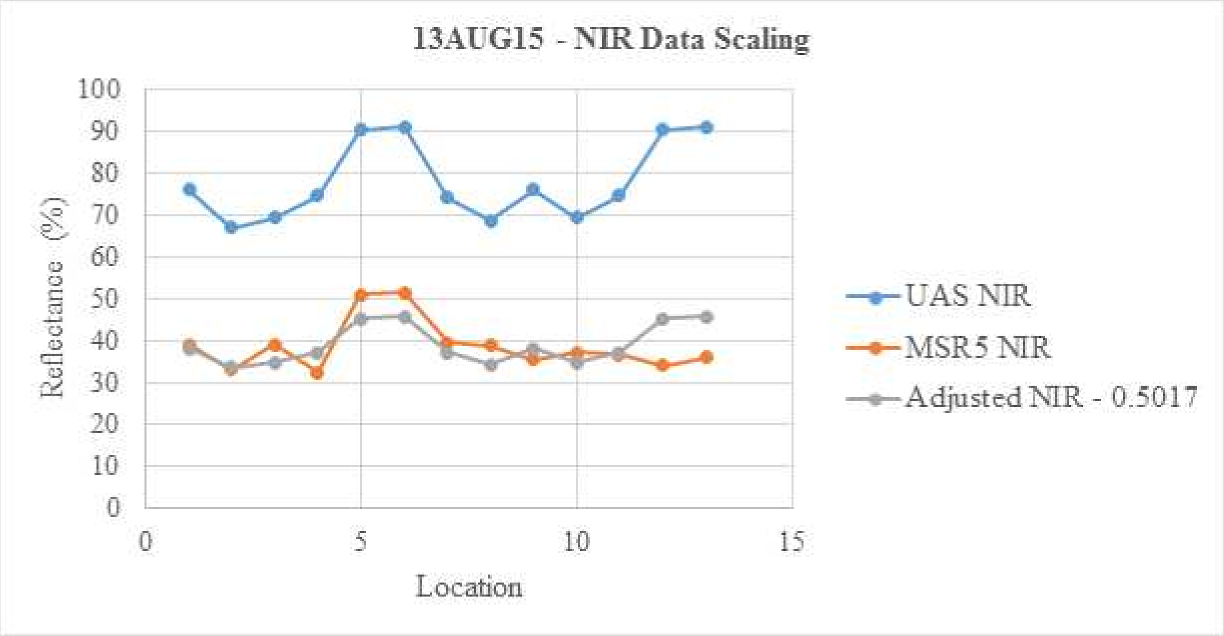

Figure 3.1. Scaling of the Tempest UAS RS NIR data due to the malfunction of the multispectral sensor.

Table 3.1. Scalar value used to correct the Tempest UAS RS NIR, red and green imagery for 30JULY and 13AUG15.

Date	NIR	Red	Green
30-Jul-15	0.7572	0.3975	0.2526
13-Aug-15	0.5017	0.261	0.1735

3.1.1. Thermal Infrared (TIR)

During the 2015 RS campaign, the CSU Tempest RS derived thermal imagery had a MBE, RMSE, and NSCE of -1.36 ^{o}C, 5.68 ^{o}C and 0.66, respectively, when compared to the ground-based MSR5 data. As the study progressed throughout the campaign, the accuracy of the thermal imagery increased until the final flight on 10SEP15, with a MBE, RMSE and NSCE of 1.20 ^{o}C, 2.40 ^{o}C and 0.92, respectively. The increased accuracy of the thermal sensor was the result of refining the collection and operational procedures associated with the sensor throughout the campaign. The overall analyses of the Tempest RS TIR Tsfc are inconclusive due to the low number of successful flights and the changing operational procedures throughout the campaign. With further testing and refinement of the sensor and collection procedures, the accuracy of the data are expected to increase to an acceptable level. Figure 3.2 depicts the direct comparison of the Tempest TIR imagery with the MSR5 TIR data during the 2015 ARDEC field 1070 RS campaign.

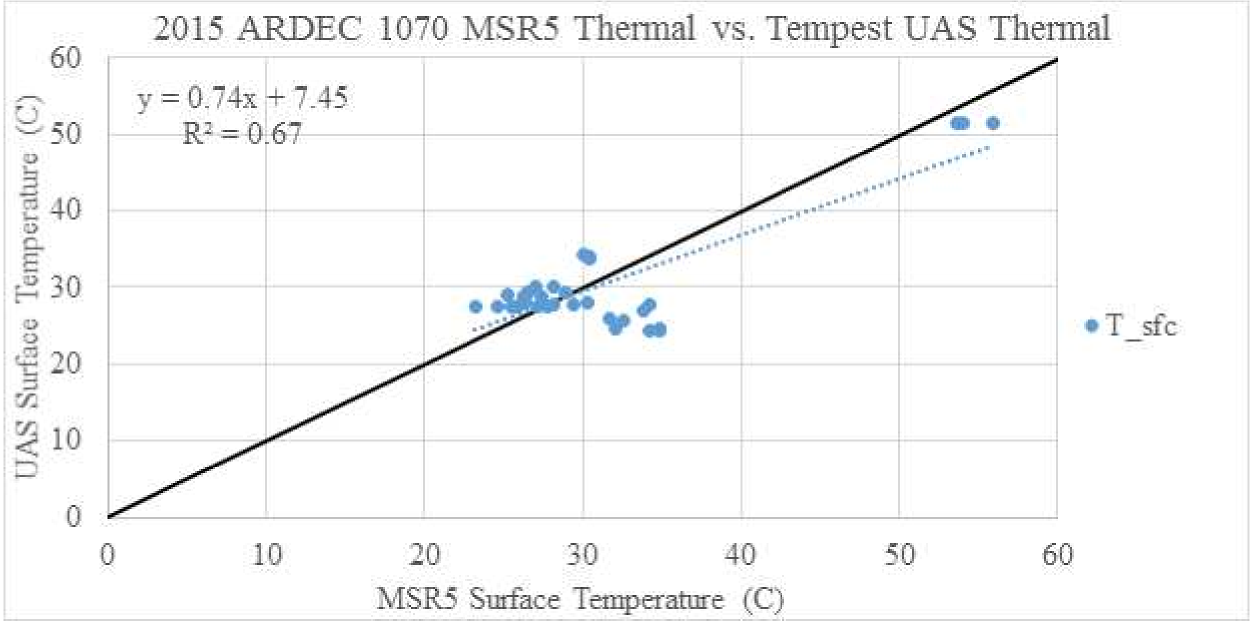

Figure 3.2. 2015 ARDEC 1070 RS Campaign Thermal RS vs MSR5 data comparison.

3.1.2. Multispectral (NIR, red and green)

The NIR, red and green Tempest RS data collected during the 2015 campaign showed a greater degree of accuracy than the thermal data. Figure 3.3 depicts the RMSE (% reflectance or ºC) of the TIR, NIR, red and green Tempest RS imagery during the 2015 ARDEC field 1070 RS campaign.

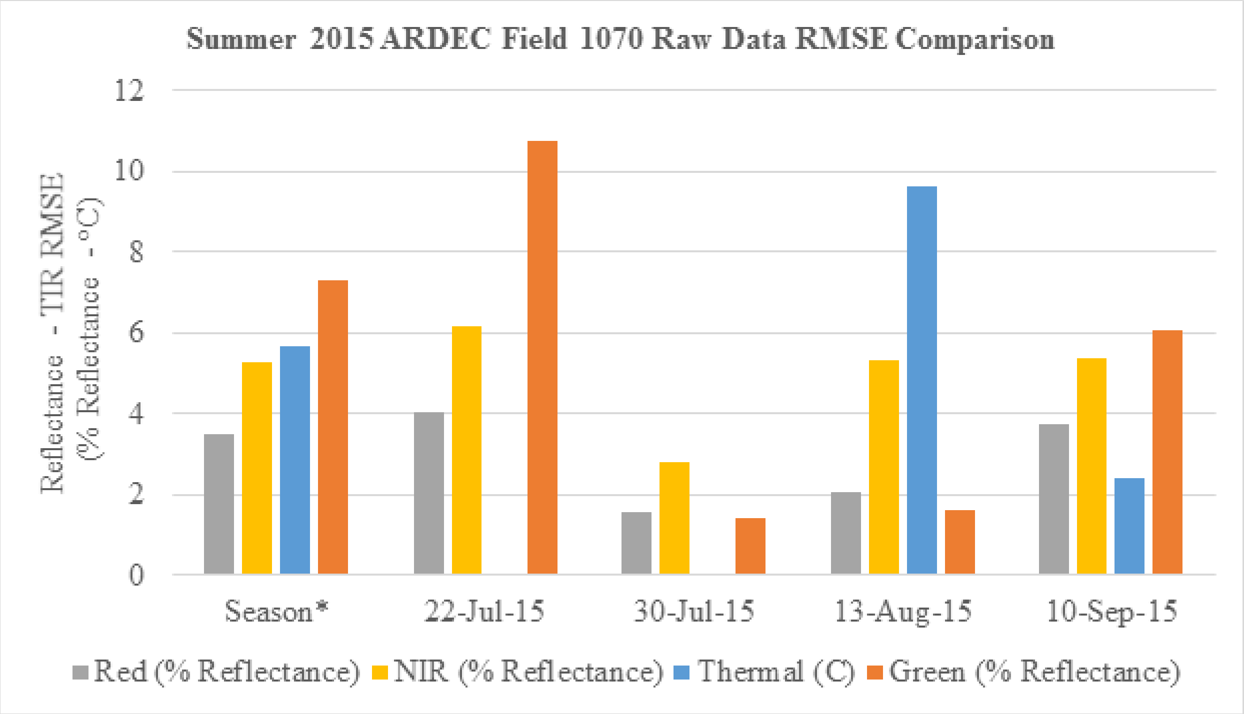

Figure 3.3. RMSE (% reflectance or °C) of the NIR, red, green and TIR imagery from the 2015 CSU Tempest RS campaign at ARDEC field 1070.

The most accurate band of the Tempest UAS multispectral sensor over the campaign was the red band, with a slight overestimation of the red reflectance with a MBE, RMSE NSCE of 0.81%, 3.51% and 0.91, respectively. Figure 3.4 depicts the strong relationship between Tempest RS red imagery vs MSR5 data. The NIR preformed less accurately, with a RMSE of 5.26%, an overall underestimation with a MBE of -1.17% and NSCE of 0.83. Figure 3.5 depicts the strong relationship between Tempest NIR imagery vs MSR5 data. The least accurate band of the multispectral sensor was the green band with campaign values of MBE=5.06 %, RMSE=7.31 % and NSCE of 0.51. Since all of the studies ET_a algorithms mainly rely on the NIR and red bands, the effects of the errors associated with the green band will be limited. The lone exception is the TSEB, which utilizes the green band to estimate the soil albedo (Eq. A.3.2.42). The expected error are low since the NIR is the predominate factor in the equation. Figure 3.6

shows the less favorable agreement of the campaign RS green vs MSR5 data. Table 3.2, 3.3 and 3.4 provides summaries of the NIR, red, green and TIR data for the 2015 campaign.

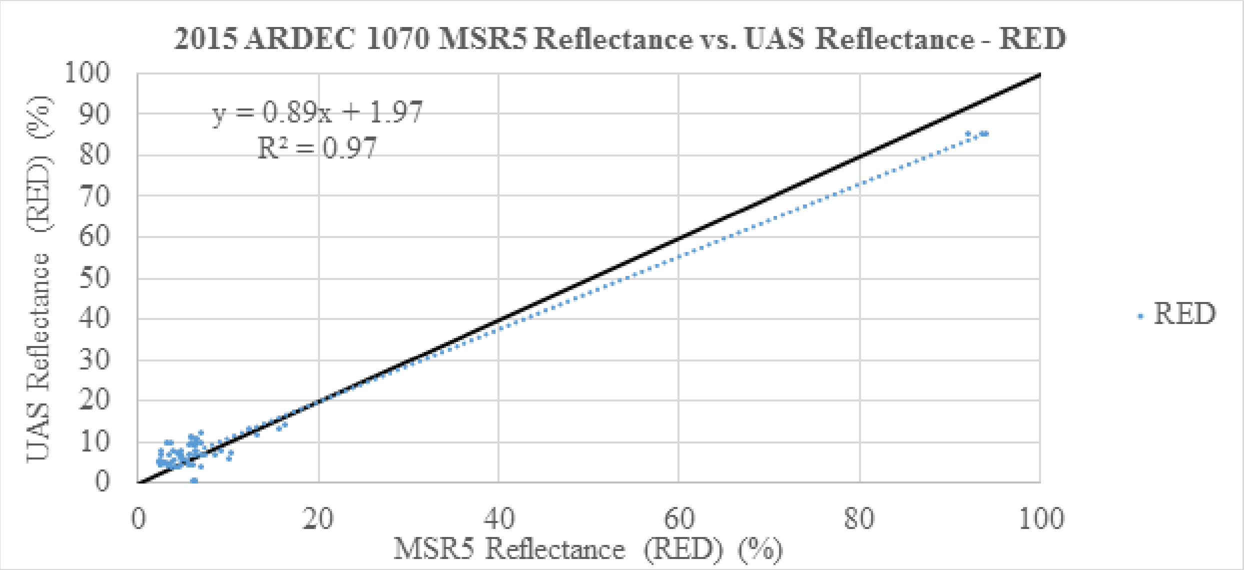

Figure 3.4. 2015 ARDEC 1070 RS Campaign red RS vs MSR5 data comparison.

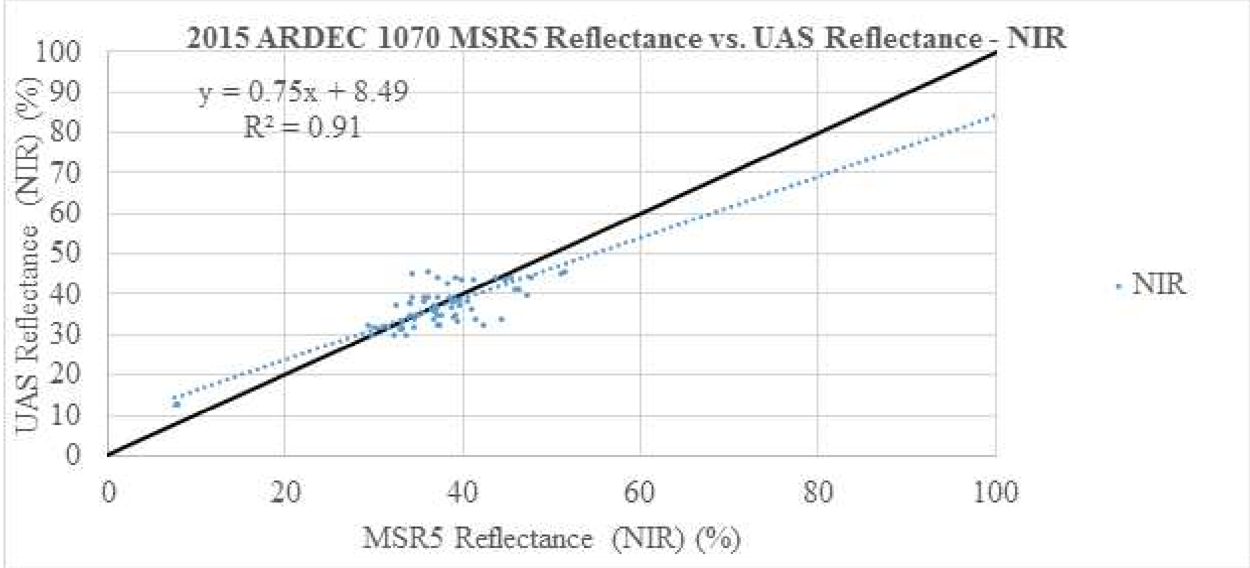

Figure 3.5. 2015 ARDEC 1070 RS Campaign NIR RS vs MSR5 data comparison.

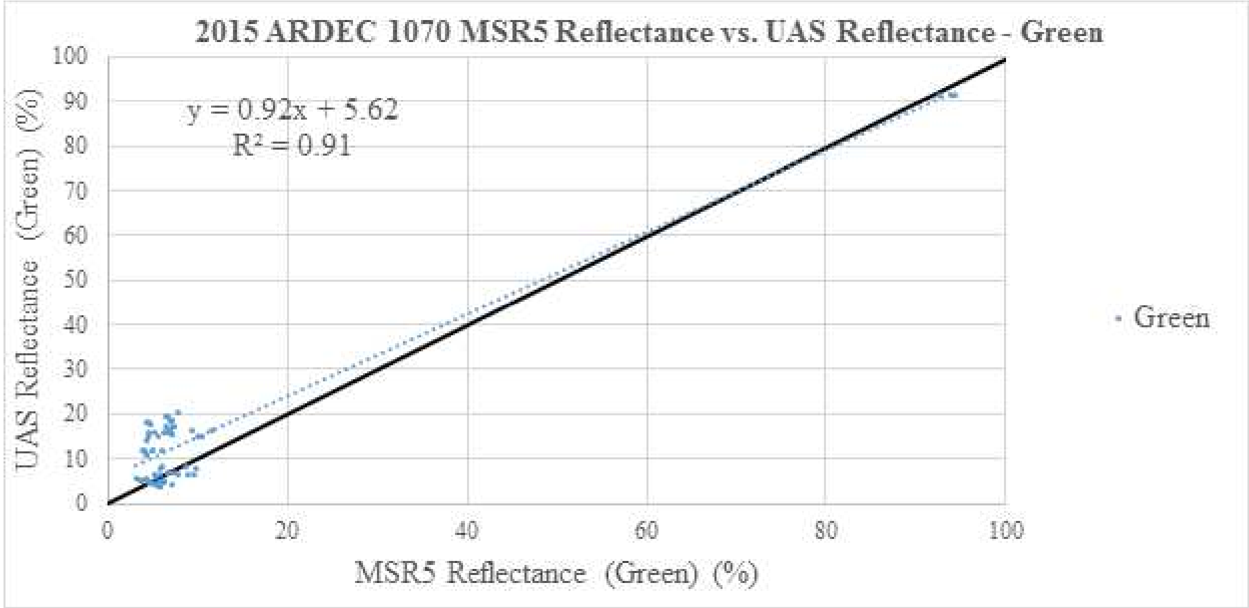

Figure 3.6. 2015 ARDEC 1070 RS Campaign green RS vs MSR5 data comparison

Table 3.2. MBE Summary of the 2015 ARDEC 1070 RS Campaign RS vs MSR5 data comparisons

2015 Tempest UAS Raw Data vs MSR5 Data MBE Results				
Flight Date	**MBE**			
	Thermal (C)	**Green (% Reflection)**	**Red (% Reflection)**	**NIR (% Reflection)**
Season*	**-1.36**	**5.06**	**0.81**	**-1.17**
22-Jul-15	⬛	10.09	3.22	-0.88
30-Jul-15	⬛	0.08	0.05	0.14
13-Aug-15	-8.02	0.14	0.04	0.19
10-Sep-15	1.20	3.28	-0.55	-1.51
Data linearly corrected due to eqipment malfunction				
Uncorrected data				
No data due to equipment malfunction				

Table 3.3. RMSE Summary of the 2015 ARDEC 1070 RS Campaign RS vs MSR5 data comparisons.

2015 Tempest UAS Raw Data vs MSR5 Data RMSE Results				
Flight Date	**RMSE**			
	Thermal (C)	**Green (% Reflection)**	**Red (% Reflection)**	**NIR (% Reflection)**
Season*	**5.68**	**7.31**	**3.51**	**5.26**
22-Jul-15	■	10.76	4.03	6.16
30-Jul-15	■	1.41	1.55	2.80
13-Aug-15	9.62	1.64	2.06	5.33
10-Sep-15	2.40	6.06	3.74	5.38
Data linearly corrected due to eqipment malfunction				
Uncorrected data				
No data due to equipment malfunction				

Table 3.4. Student-T Test Summary of the 2015 ARDEC 1070 RS Campaign RS vs MSR5 data comparisons.

2015 Tempest UAS Raw Data vs MSR5 Data RMSE Results				
Flight Date	**T_Test**			
	Thermal	**Green**	**Red**	**NIR**
Season*	**0.12**	**0.00**	**0.05**	**0.06**
22-Jul-15	■	0.10	0.58	0.82
30-Jul-15	■	0.81	0.91	0.93
13-Aug-15	0.00	0.79	0.95	0.93
10-Sep-15	0.45	0.29	0.98	0.71
Data linearly corrected due to eqipment malfunction				
Uncorrected data				
No data due to equipment malfunction				

The study focused primarily on the NIR and red bands of the Tempest RS imagery due to their importance in the calculation of the RS VIs (OSAVI and NDVI) required in the estimation of the ET_a and SWD. The accuracy to the NIR and red bands are shown by the campaign MBE and RMSE of the OSAVI and NDVI, with values of MBE =-0.024 and RMSE=0.21. The close agreement between the Tempest and the MSR5 suggests that the values of the NIR and red bands of the multispectral sensor are adequate for use in the RS ET_a and SWD models.

The statistical analysis of the raw Tempest UAS data, using $\propto$=0.05, suggest that there is significant statistical evidence that the mean campaign reflectance for the TIR (0.12), Red (0.05) and NIR (0.06) are the same as the mean reflectance from the MSR5. The green (0.00) for the campaign does not have statistical significant evidence that the mean reflectance is the same as the MSR5 for the entire campaign. All of the band showed statistical significant evidence that the mean reflectance is the same as the MSR5 reflectance for the individual RS overpasses. The discrepancy between the campaign and RS overpasses stems from the low sample size from the summer of 2015 RS campaign. In order to increase the power and accuracy of the T-test, additional ground data collection must be conducted to increase the sample size of the individual and campaign overpasses. Even with the low sample size, the raw Tempest RS data accurately describes the actual conditions on the ground.

The NSCE analysis of the raw Tempest RS data shows the wellness of fit between the Tempest raw data and data collected with the MSR5 multispectral sensor. All of the bands had seasonal NSCE values greater than 0, which shows that the variance between the ground and Tempest data is less than the variance between the observed and mean ground measurements. This suggests that using the spatially distributed RS data is more accurate than using the mean ground-based remote sensing data. Table 3.5 and Figure 3.7. describe the NSCE results for the raw RS data.

Table 3.5. NSCE analysis of the Raw Tempest UAS RS data.

Raw Data Nash-Sutcliffe Coefficient of Efficiency				
	Thermal	**Green**	**RED**	**NIR**
Season	0.66	0.51	0.91	0.83
22-Jul-15	N/A	-215.82	-12.40	-1.14
30-Jul-15	N/A	-0.58	-0.18	0.35
13-Aug-15	-9.16	-0.53	-0.17	0.33
10-Sep-15	0.92	0.70	0.94	0.94

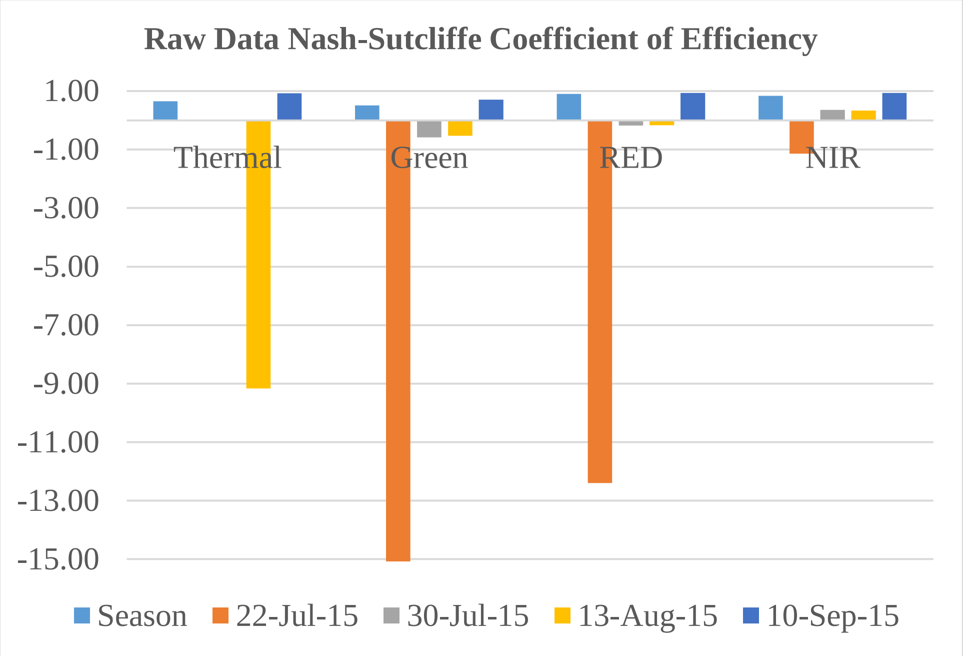

Figure 3.7. Raw data NSCE comparison for the 2015 Tempest RS campaign.

Errors, not associated with the individual sensor's operational capabilities, were induced into the UAS RS and ground RS systems from multiple sources including variation in data collection procedures on the ground and the Tempest UAS, environmental conditions (changing conditions or non-ideal conditions during the flights) and the uncertainty of the exact location of the footprint/field of view of the ground data. The UAS data were collected over a period of five minutes (essentially a single point in time), while the ground data were collected over thirty to forty-five minutes. The longer sample time for the ground-based RS were a result of having to move the equipment throughout the test location, during which time the meteorological conditions were continually changing. These introduced errors contributed to variation between the ground and UAS data. However, when working with vegetation indices a good deal of the environmental conditions are normalized. An additional source of error most probably was caused by the data processing procedures in ERDAS Imagine. The raw Tempest data were not geometrically or optically corrected prior to the analysis. The error associated with the lack of geometric and optical correction are unknown and will be addressed in future studies. The errors associated with the lack of correction are evident in Figure 3.8. By addressing the errors induced by the data collection and processing procedures, the accuracy of the Tempest UAS RS platform will increase when compared to the ground collected data.

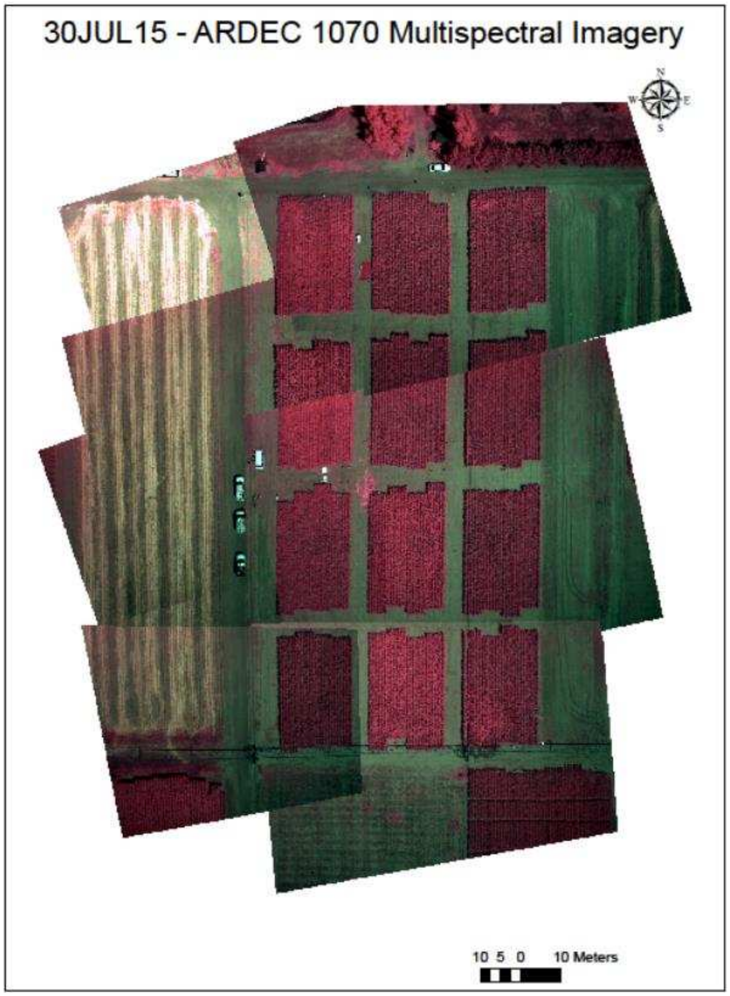

Figure 3.8. Depiction of the raw data processing errors of the multispectral imagery.

3.2. Daily ET_a Results and analysis

All five RS methods used to calculate daily ET_a utilized the raw data collected with the Tempest UAS (supplemented with the USU data if required), meteorological data from the ARDEC CoAgMet weather station and ERDAS Imagine GIS software. The RS derived daily ET_a were compared to the daily ET_a values estimated using the weekly NP data and two FAO-56 SWB models. The FAO-56 SWBs were calculated using varying soil root zones depths and crop coefficients. The two SWBs were calculated using root zone depths of 1.5 m and 1 m. The analysis of the multiple root zone depths was required due to insufficient irrigation throughout the growing season causing the root zone to reach non-standard depths ($R_z \geq 1$ m). The summary of the results of the 2015 Tempest UAS RS ET_a campaign are described in Table. 3.6. The RS, FAO-56 and NP derived daily ET_a values for the ARDEC 1070 NP locations are provided in Appendix 4.

Table 3.6. Summary of the statistics from the daily ET_a derived from the 2015 Tempest UAS RS campaign.

Method	Statistic	Season	22-Jul-15	30-Jul-15	13-Aug-15	10-Sep-15
TSEB	MBE (mm/d)	**0.29**	N/A	0.23	0.06	0.58
	RMSE (mm/d)	**0.89**	N/A	1.10	0.54	0.93
	2*P[T<=t]	**0.00**	N/A	0.15	0.47	0.00
SAT	MBE (mm/d)	**0.49**	N/A	-0.89	0.03	0.96
	RMSE (mm/d)	**1.21**	N/A	1.56	0.95	1.47
	2*P[T<=t]	**0.00**	N/A	0.00	0.83	0.00
NDVI	MBE (mm/d)	**0.79**	0.14	1.27	0.49	1.28
	RMSE (mm/d)	**1.43**	0.91	1.83	1.00	1.74
	2*P[T<=t]	**0.00**	0.29	0.00	0.00	0.00
FAO-56 SWB Rz=1 m	MBE (mm/d)	**-0.94**	-1.17	-0.96	-1.27	-0.36
	RMSE (mm/d)	**1.22**	1.46	1.23	1.36	0.82
	2*P[T<=t]	**0.00**	0.39	0.00	0.14	0.83
FAO-56 SWB Rz=1.5 m	MBE (mm/d)	**1.44**	-0.73	0.52	1.97	1.20
	RMSE (mm/d)	**1.64**	1.11	0.86	2.17	1.49
	2*P[T<=t]	**0.00**	0.39	0.00	0.00	0.00
CWSI	MBE (mm/d)	**1.58**	N/A	0.52	-0.55	0.01
	RMSE (mm/d)	**1.86**	N/A	0.86	0.74	0.75
	2*P[T<=t]	**0.00**	N/A	0.00	0.01	0.00
FC	MBE (mm/d)	**1.88**	1.08	2.65	1.25	1.92
	RMSE (mm/d)	**2.30**	1.44	2.96	1.85	2.23
	2*P[T<=t]	**0.00**	0.00	0.00	0.00	0.00

The most accurate Tempest RS derived daily ET_a from the study was from the TSEB method. The TSEB had promising agreement with the NP derived ET_a, with a campaign slight overestimation MBE of 0.29 mm/day, RMSE of 0.89 mm/day and NSCE of 0.67. The TSEB derived ET_a were selected for further evaluation with the Hybrid SWD model. The TSEB performed better, with an average reduction of MBE of 0.65 mm/day and RMSE of 0.33 mm/day, than the most accurate FAO 56 SWB method using R_z=1 m (MBE of -0.94 mm/day and RMSE of 1.22 mm/day) at estimating the daily ET_a. Figure 3.9 depicts the relationship between the TSEB and SWB derived ET_a and the NP derived ET_a during the 2015 ARDEC field 1070 RS campaign. The FAO-56 SWB consistently underestimated the ET_a while TSEB overestimated the lower values (ET_a < 3.20 mm/d) of ET_a and closely approximates ET_a values over 3.20 mm/d.

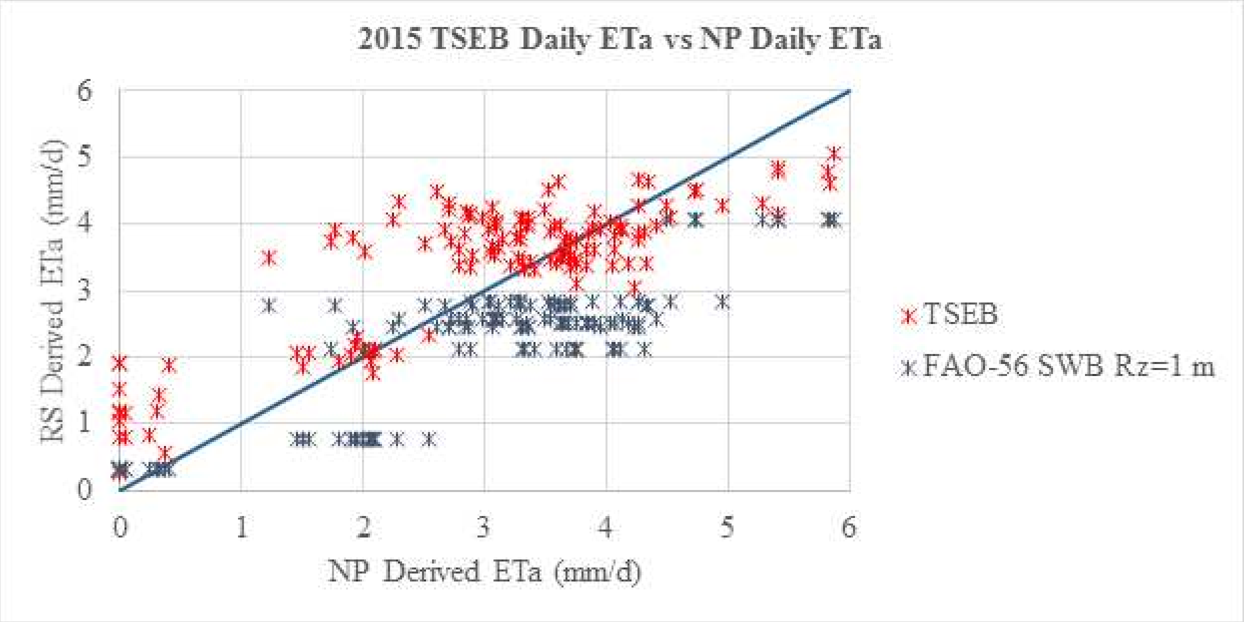

Figure 3.9. Comparison of the TSEB and RS Adjusted SWB and FAO 56 SWB derived daily ET_a vs the NP derived daily ET_a.

Of the five RS daily ET_a models tested, the TSEB and SAT models (both SEB based) performed better than or comparable to the most accurate FAO 56 SWB estimations with average decrease of RMSE of 0.33 mm/day and 0.01 mm/d, respectively, when compared with the FAO-56 SWB RMSE. Figure 3.10 depicts the comparison of the methods RMSE of the RS and SWB derived daily ET_a to the NP derived daily ET_a, showing the level of performance of the various methods.

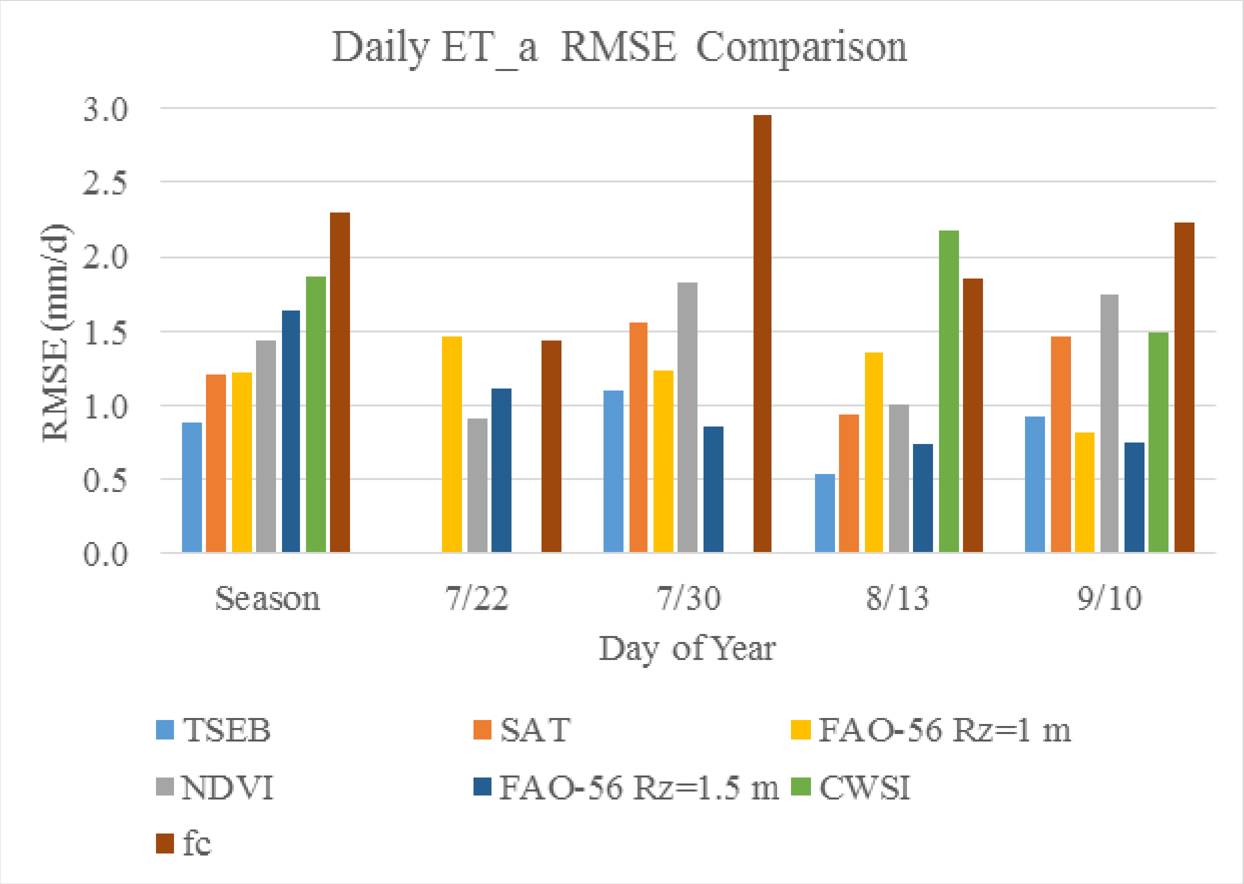

Figure 3.10. Comparison of the daily ET_a RMSE (mm/d) at ARDEC 1070 during the 2015 growing.

The NSCE analysis of the most accurate ET_a models are described in Table 3.7 and Figure 3.11. The NSCE of the TSEB (0.67) suggest that there is significant agreement between the method and the ground observation over the RS campaign and for the individual RS overpasses. The ET_a NSCEs increased throughout the season, it is unknown whether the increase was caused by the capabilities of the Tempest RS data or were a result of the refinement of the collection procedures throughout the RS campaign.

Table 3.7. NSCE analysis of the RS derived ET_a models (TSEB and SAT).

ETa Nash-Sutcliffe Coefficient of Efficiency		
	TSEB	**SAT**
Season	0.67	0.19
30-Jul-15	0.35	0.06
13-Aug-15	0.66	-0.04
10-Sep-15	0.73	0.43

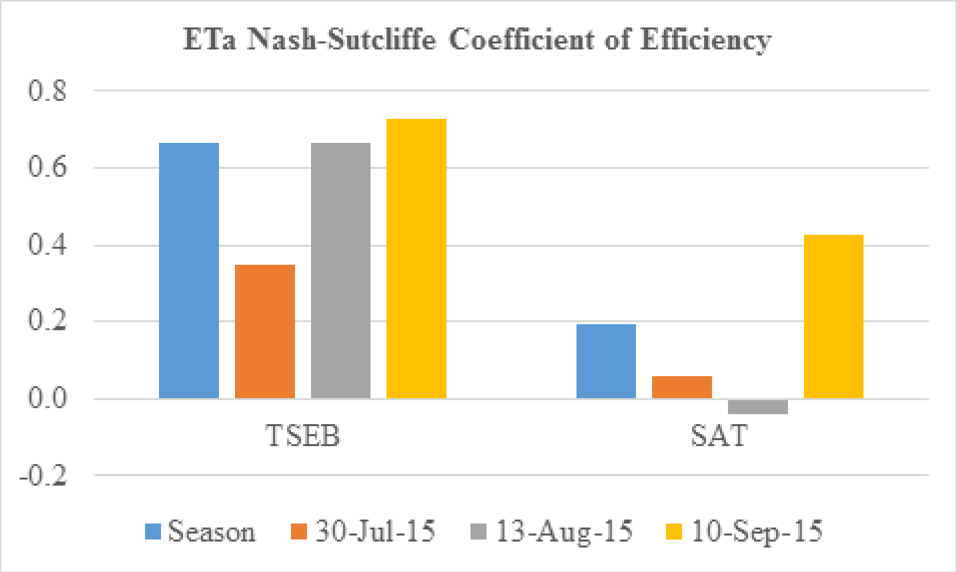

Figure 3.11. NSCE comparison of the TSEB and SAT RS ET_a methods utilizing the Tempest UAS remote sensing data.

The available data suggests that the RS models, the TSEB in particular, have the ability to more accurately estimate the spatially distributed daily ET_a than using the FAO-56 SWB method alone. For application in a PA irrigation management system, the spatially distributed ET_a data are more beneficial than the field-average (point) FAO-56 SWB ET_a, due to the inherent variability of the ET_a throughout a field. The spatial variability of ARDEC field 1070 of the FAO-56 SWB and the TSEB derived ET_a is shown in Figure 3.12. Figure 3.12 is the spatially distributed variability of the FAO-56 SWB and RS derived ET_a (RS ET_a – SWB ET_a). The capability of modeling the spatial variability of a field's crop water requirement is critical to accurately developing an efficient PA irrigation management system. Figure 3.12 highlights the advantage of at least occasionally estimating ET_a with RS techniques. Three FAO-56 SWB, one for each irrigation treatment, were utilized to estimate the ET_a, and a large spatial variability is present in the treatments.

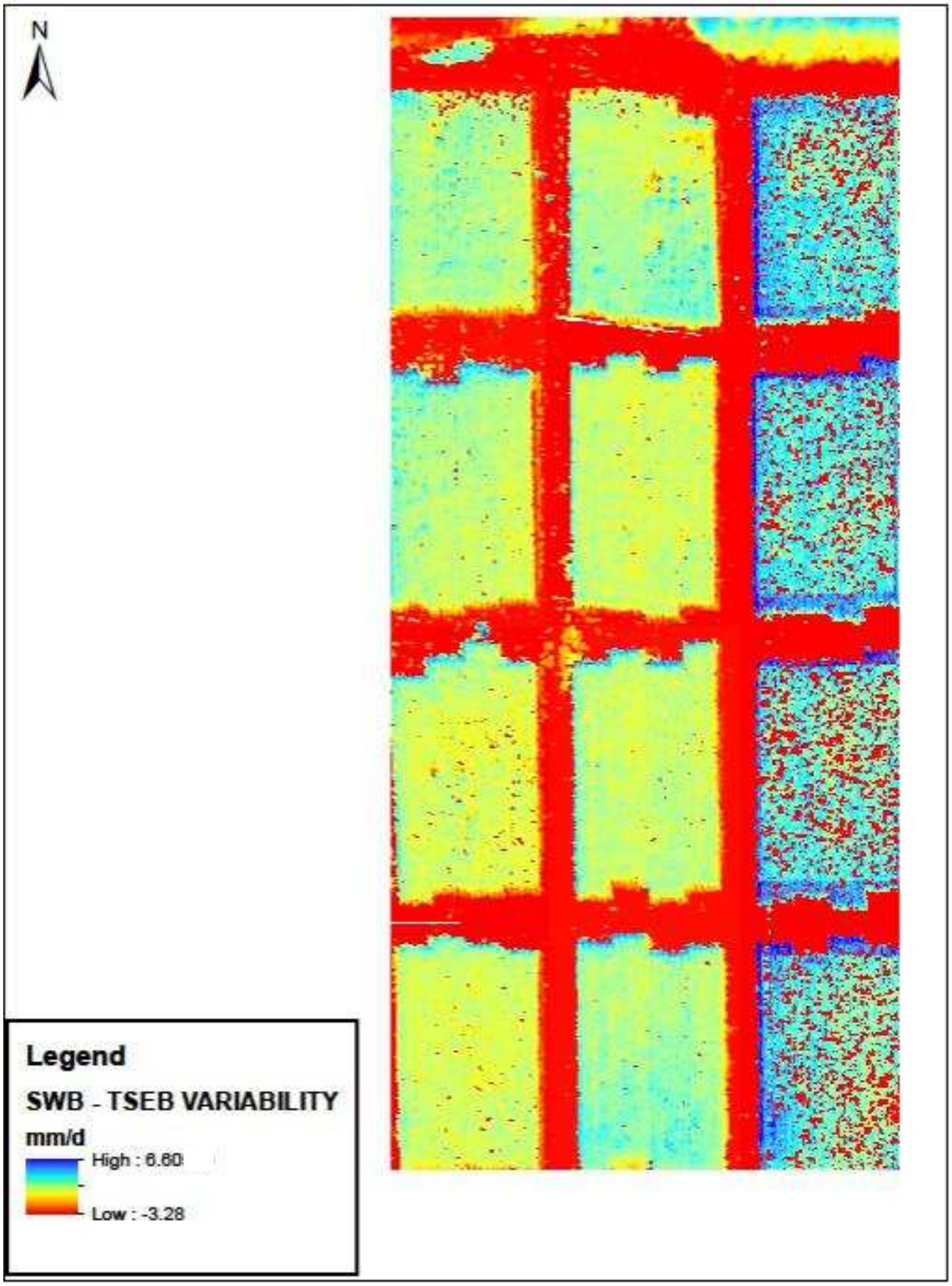

Figure 3.12. Spatial variability of the difference between the TSEB and FAO-56 SWB ET_a estimates.

The CWSI and the f_c (reflectance) methods performed worse than the best FAO-56 SWB during the 2015 campaign. The f_c reflectance method performed the worst of the RS models tested with a campaign MBE of 1.88 mm/day and RMSE of 2.30 mm/day when compared to the NP derived daily ET_a. The increased error associated with the f_c (reflectance) based ET_a model were associated with the spatial variability of the meteorological, physical (wetted soil) and biophysical conditions of the test location, as well soil background interference resulting from treatments depicting low LAI and f_c. The f_c method only accounts for the transpiration based on the amount of vegetative cover. The drought treatments showed the largest amount of error since the method bases the ET_a estimation on the amount of f_c and not the level of stress experienced by the crop. Even though the drought treatments were experiencing stress ($k_s<1$) at a higher level than the other treatment, the f_c of the treatments remained relatively the same. To increase the accuracy of the reflectance-based models, site-specific calibrations that take into account the local meteorological and biophysical properties of the location are required. A possible source of the increased error associated with using the CWSI method are the evolution of the collection methods and procedures associated with the thermal sensor throughout the 2015 RS campaign. As shown in Table 3.2, the RMSE of the thermal imagery reduced from 9.62^oC to 2.40^oC from the 13AUG15 flight to the 10SEP15 flight. The reduction in the thermal RMSE caused the RMSE of the CWSI daily ET_a to go from 2.17 mm/day on 13AUG15 to 1.49 mm/day on 10SEP15, which was similar to the SAT overpass RMSE of 1.47 mm/day. The accuracy of the CWSI will continue to increase as the procedures for the thermal sensor are refined and less soil background are seen by the sensors. The CWSI method was developed for use with data collected after solar noon in order to allow the crop to develop the increased canopy temperature associated with higher levels of stress. Since the RS data were collected before solar noon, the canopy was not allowed to heat to show the true level of stress, resulting in an increased ET_d. The error with the thermal sensor also affected the RMSE of the TSEB and SAT models as well. The overall increase of error of the SAT and TSEB models were less than with the CWSI due to the integration of the thermal and multispectral data. Additionally, the CWSI ET_a were estimated utilizing T_{sfc} in lieu of T_c in order to provide a model based on the TIR imagery alone. This introduced error to the CWSI derived ET_a due to the variation between the canopy and the surface radiometric temperatures. In order to increase the accuracy of the CWSI method, the T_c should be calculated as described in the TSEB method.

During the summer 2015 ARDEC field 1070 RS campaign, all of the methods had significant statistical evidence that their mean ET_a differed from the mean NP derived ET_a. During individual RS overpasses, the NDVI (22JUL15: 0.29), TSEB (30JUL15: 0.15, and 13AUG15: 0.47) and SAT (13AUG15: 0.83) methods had $2*P[T \leq t] > \alpha = 0.05$, showing statistically significant evidence that their mean ET_a were the same as the mean NP derived ET_a. A source of error while conducting the Student T-test can be attributed to the mechanical and procedural deviations between the RS overpasses. Further testing is required to analyze the statistical significance of the RS ET_a methods.

Due to the low number of RS overpasses and variations in the RS data used for the RS derived comparisons, and the variation of the individual RS overpasses, the analysis of the RS models are inconclusive. Additional data collection overpasses are required to fully analyze the capability of the RS models.

The final product of the RS ET_a model is a spatially distributed daily ET_a map for the use with a PA irrigation system. Figure 3.13 is the spatially distributed daily ET_a map for ARDEC field 1070 on 10SEP15. The daily ET_a map ranges from light green (6.61 mm/d) to red (0 mm/d). As shown by the map, the full and limited irrigation treatments have a higher level of ET_a than the drought treatments. The daily ET_a map is used to calculate the SWD in a PA irrigation management system.

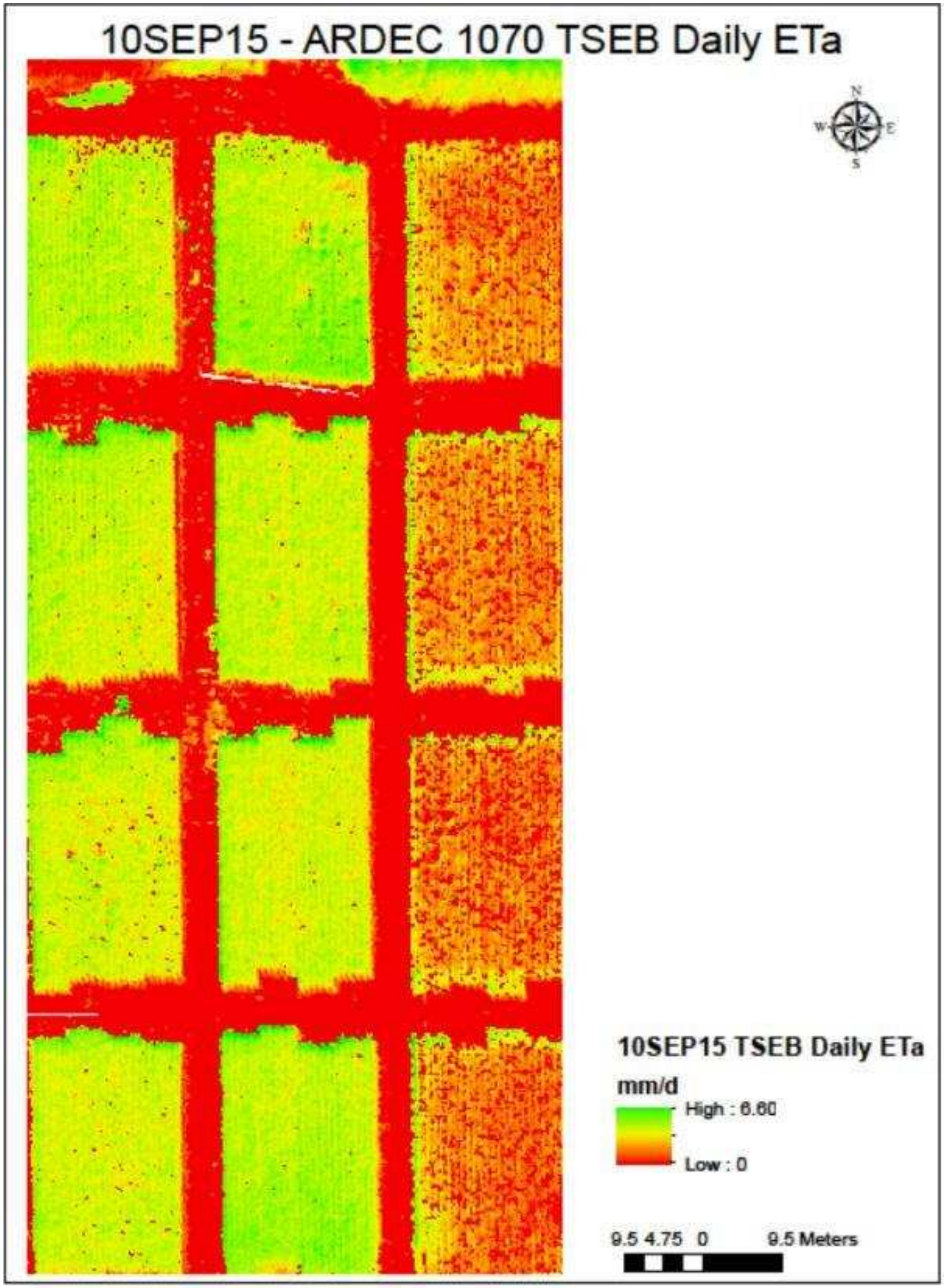

Figure 3.13. Spatially distributed daily ET_a map for ARDEC field 1070 on 10SEP15.

3.3. Mapping Soil Water Content using the Soil Water Balance

The RS derived soil water balances were calculated using the TSEB estimated ET_a and the hybrid soil water balance method. The spatially distributed SWD, calculated using the hybrid soil water balance method, were compared to the daily FAO-56 SWD and the weekly NP derived SWD. All values of SWD are reported in mm m^{-1} to allow comparison over multiple R_z depths. The comparison of the SWDs occurred for the flights conducted on 30JUL15, 13AUG15 and 10SEP15 in order to ensure that the crop was experiencing stress conditions ($k_s<1$) and the availability of the required data. This was a requirement to estimate the SWD (D_i) using the hybrid method due to the relationship between k_s and D_i, illustrated in Figure 2.9. The summary of the statistics for comparison of the Hybrid, FAO-56 (UAS adjusted, R_z=1 m and R_z=1.5 m) and NP derived SWD for ARDEC field 1070 as a whole, over the campaign and individual RS overpasses, are described in Table 3.8 and 3.9. Appendix 4 provides the SWD (NP, Hybrid and FAO-56 SWB) by NP access tube location for the individual overpasses.

Table 3.8. Summary of the RS flight day soil water deficit statistics for the ARDED field 1070 summer 2015 RS campaign.

ARDEC 1070 RS Overpass Soil Water Deficit Summary				
	Date	**MBE (mm)**	**RMSE (mm)**	**T-Test**
Hybrid	30-Jul-15	6.32	19.74	0.03
	13-Aug-15	-9.92	21.94	0.00
	10-Sep-15	-3.76	18.78	0.25
Rz=1 m FAO-56	30-Jul-15	-29.55	59.09	0.00
	31-Jul-15	-14.16	23.83	0.00
	1-Aug-15	-25.16	31.90	0.00
Rz= 1.5 m FAO-56	30-Jul-15	46.69	53.16	0.00
	13-Aug-15	39.50	48.20	0.00
	10-Sep-15	46.57	54.94	0.00

Table 3.9. Summary of the RS Campaign soil water deficit statistics for the ARDED field 1070 summer 2015 RS campaign.

ARDEC 1070 RS Campaign Soil Water Deficit Summary				
	MBE (mm/m)	**RMSE (mm/m)**	**T-Test**	
Hybrid	-2.45	20.20	0.24	Campaign
Rz=1 m FAO-56	-22.96	33.59	0.00	Campaign
Rz= 1.5 m FAO-56	29.68	42.60	0.00	Campaign

The hybrid method produced the most accurate estimation of the spatially distributed SWD (mm/m) of all the methods with a MBE of -3.55 mm/m, a RMSE of 21.60 mm/m and NSCE of 0.86. The hybrid data analysis did not include the 10SEP15 NP from the drought treatments 409, 410 or 411 due to abnormally low SWD (25 mm/m decrease) of those locations. Utilizing the 5TE SWS in the 410 treatment, the actual SWD are consistent with the hybrid and SWB estimates. The low NP SWD calculations were attributed to the dry conditions of the soil. The soil experienced cracking and established preferential water infiltration paths to the NP access tubes, resulting in lower SWD estimation. In future research, NP as well as 5TE SWS should be used to calculate the actual SWD. The hybrid method RMSE was 13.40 mm/m less than the most accurate FAO-56 SWB (R_z=1 m) RMSE with an average underestimation (MBE of -23.13 mm/m) of the SWD, RMSE of 33.68 mm/m and NSCE of 0.37. The comparisons of the RMSE for all of the methods are shown in Figure 3.14. Figure 3.15 shows the direct comparison of the hybrid SWD to all forty-eight NP locations for ARDEC field 1070.

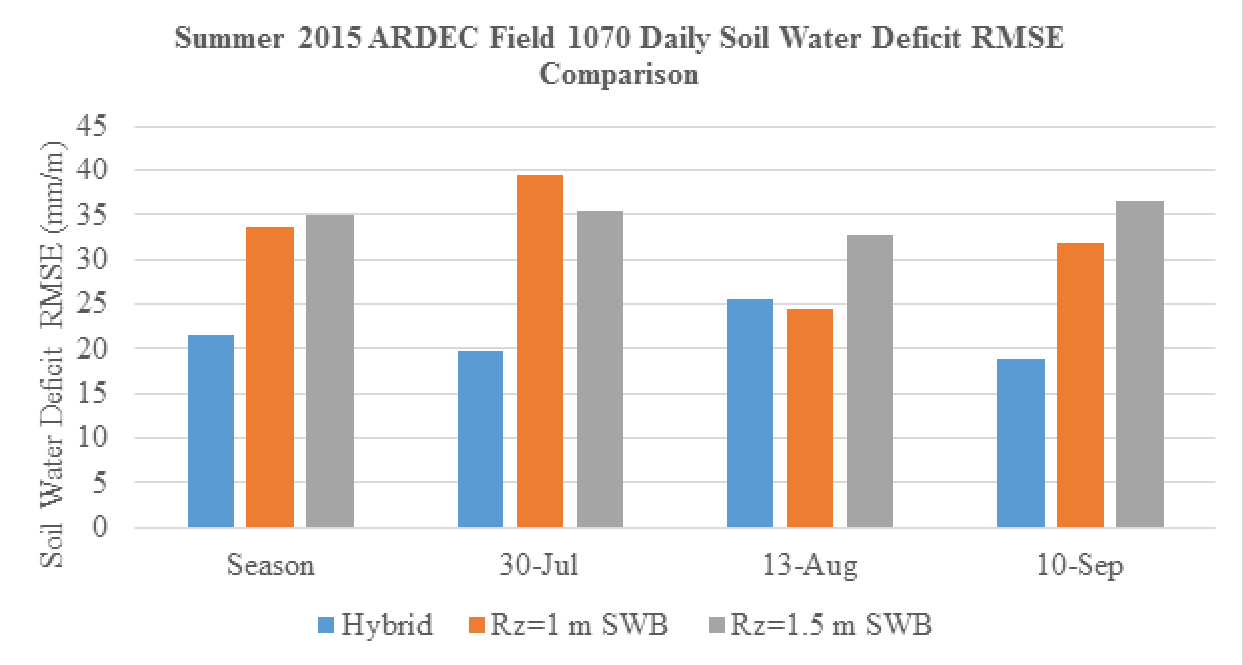

Figure 3.14. Seasonal and Daily comparison of the RMSE (mm/m) of the Hybrid and FAO-56 SWB SWDs.

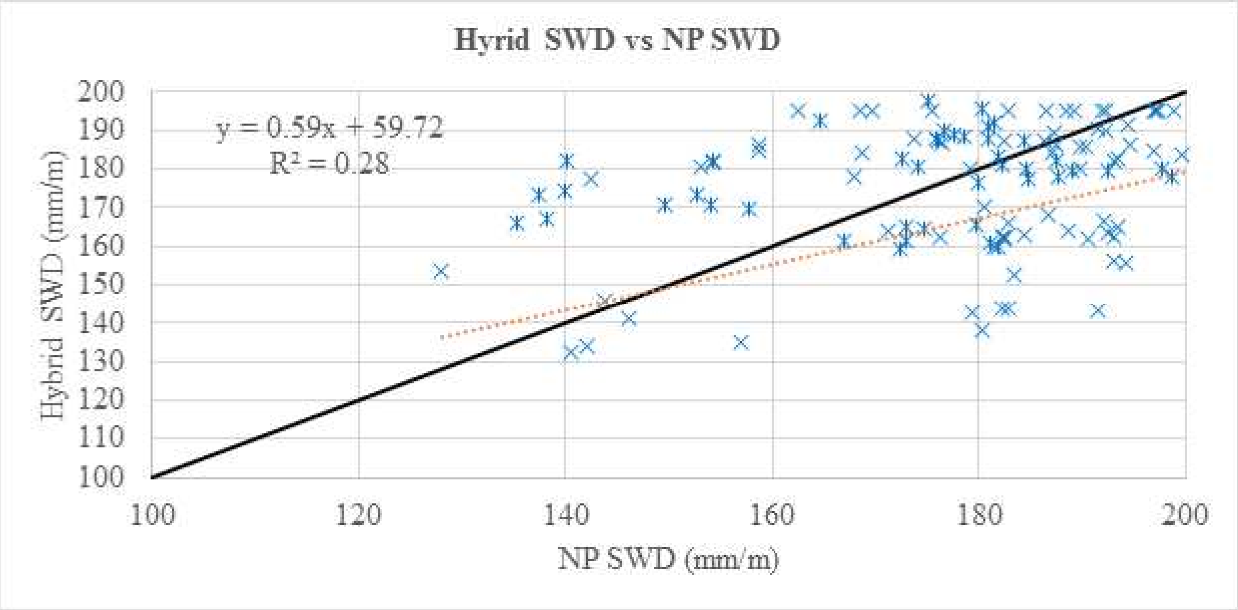

Figure 3.15. Seasonal comparison of the Hybrid soil water deficits.

Figure 3.14 shows that the hybrid method is the most accurate methods over the 2015 campaign, but it also suggests that the accuracy of the FAO-56 SWB method depends on the assumed R_z of the model. According to the FAO-56, the R_z for field corn is between 1.0 and 1.7 m. Under conditions of no water stress (k_s=1), the R_z remains around 1.0 m. While, under conditions of water stress ($k_s<1$), the R_z increases as the crop attempts to access the required water at deeper layers if available. During the summer of 2015, there were insufficient irrigation in all irrigation treatments throughout the growing season. As a result of the unintended water stress, the R_z of all the treatments were larger than anticipated and the R_z of the plots spatially varied with treatment and time. The fact that the MBEs of the FAO-56 SWBs for the Rz=1m and Rz=1.5m go from an average underestimation (MBE=-23.13 mm/m) to an average overestimation (MBE=29.68) suggest that the actual R_z were between the 1m and 1.5m that were tested. The relationship between the treatments and the spatially and temporally distributed R_z is shown in Figure 3.16.

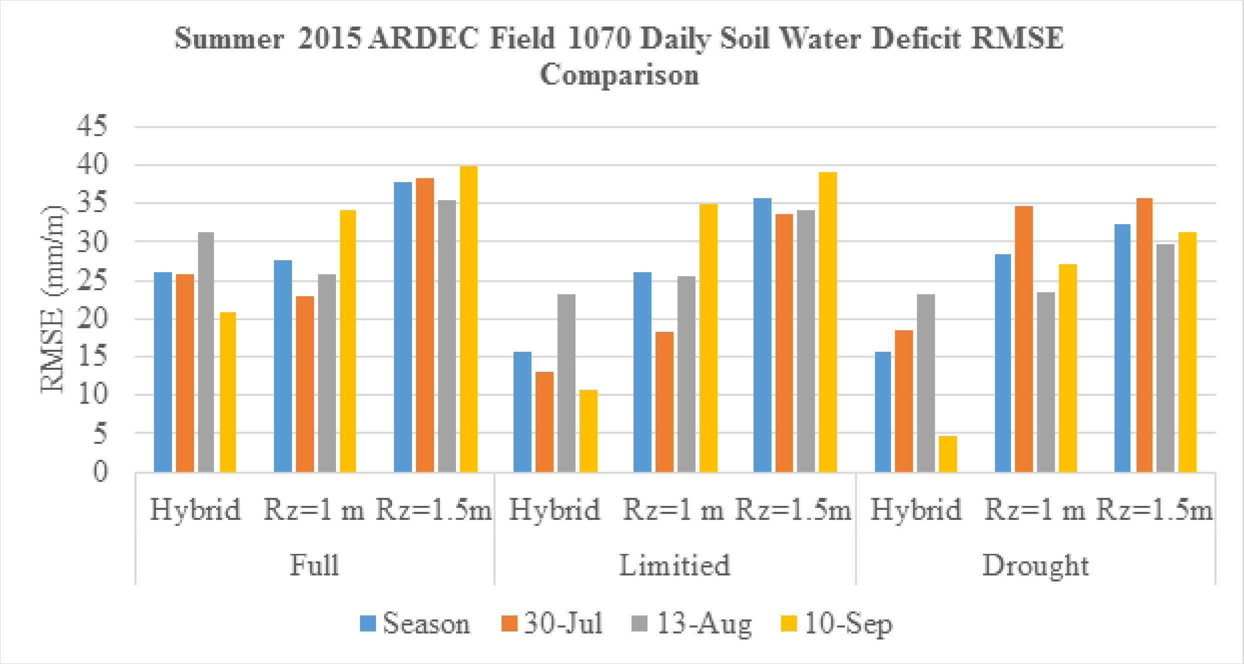

Figure 3.16. Seasonal and Daily comparison of the RMSE (mm/m) of the Hybrid and FAO-56 SWB soil water deficits for the three irrigation treatments and R_z depths.

Table 3.10. Hybrid and FAO-56 SWB NSCE analysis.

SWD Nash-Sutcliffe Coefficient of Efficiency							
	FAO	**Hybrid**	**FAO**			**Hybrid**		
			Full	**Limited**	**Drought**	**Full**	**Limited**	**Drought**
Season	0.37	0.86	0.90338	0.34431	0.82626	0.94026	0.8531	0.92252
30-Jul-15	0.6803	0.83338	0.71198	0.71268	0.45105	0.66606	0.90648	0.84806
13-Aug-15	0.91126	0.98665	0.92344	-0.4234	0.81925	0.95404	-0.1521	0.82199
10-Sep-15	-1.5249	0.89301	0.77299	-11.614	0.81799	0.91528	-0.143	0.87014

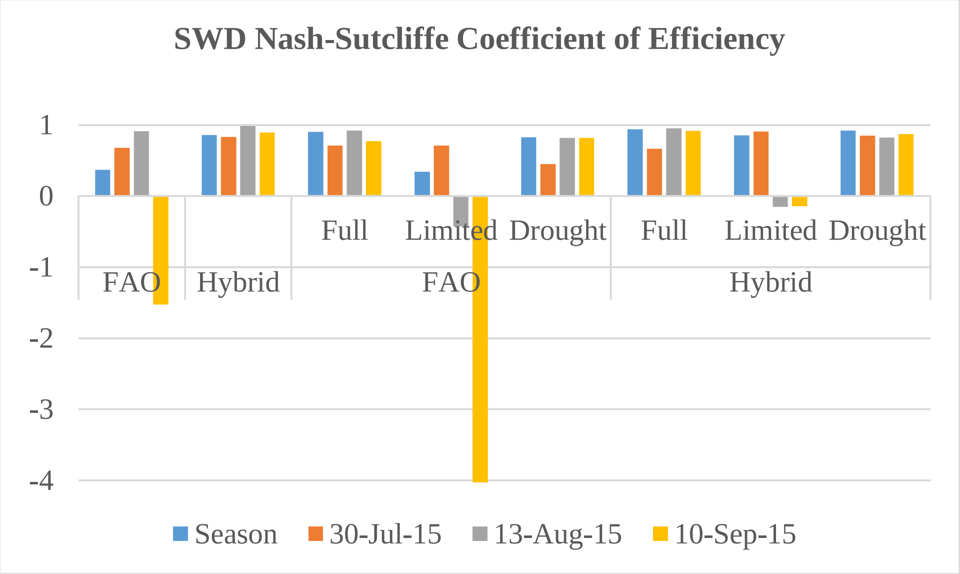

Figure 3.17. NSCE comparison of the irrigation treatment Hybrid and FAO-56 SWD model for the RS campaign and RS overpasses.

The NSCE analysis of the Hybrid and the FAO-56 SWD suggests that the Hybrid method is superior at estimating the spatially distributed SWD. The accuracy of the Hybrid method is the greatest in conditions of larger SWD and crop water stress. The increased accuracy under higher SWD levels is depicted in Figure 3.17.

There is evidence to suggest that there is a statistical significance (α=0.05) that both the hybrid (2*P[T≤t]=0.44) and the UAS adjusted FAO-56 SWB (2*P[T≤t]=0.23) have a seasonal mean soil water deficit that are the same as the seasonal mean of the NP derived SWD. With the low MBE, RMSE, NSCE approaching 1 and statistical significant evidence that the seasonal mean are the same, the hybrid method, using the TSEB derived ET_a, is a valid method of estimating the spatially distributed SWD.

The assimilation of the RS derived SWD into the FAO-56 SWB increased the accuracy of the FAO-56 SWB by an average reduction of RMSE by 7.37 mm/m over the growing season. The increased accuracy RS adjusted SWB resulted in an increase of required irrigation by approximately 36%. The increased water requirement were caused by the insufficient irrigation as discussed previously. Figure 3.18 shows the comparison of the UAS adjusted SWB and the FAO-56 SWB derived SWD. The figure shows the increased accuracy of the UAS adjusted SWB. The accuracy is affected by the underestimated hybrid SWD on 13AUG15. Possible sources of error for the UAS adjusted and FAO-56 SWB are inaccurate effective irrigation and precipitation amounts, as well as in accurate R_z depths as discussed previously. Inaccurate effective irrigation and precipitation would account for the underestimation of SWD from 13AUG15 until 10SEP15. During this time frame, there was an estimated 81.28 mm of effective irrigation and 11.43 mm of effective precipitation. The effective irrigation is assumed to be an accurate representation when using an efficiency of 90% using a lateral move irrigation system. The error is more than likely associated with the assumed effective precipitation at ARDEC 1070. The low average amount of precipitation (0.97 mm/event) from 30JUL15 to 10SEP15, along with high wind speeds (average daytime wind speed, u=2.31 m/s) and other meteoroligcal conditions suggest that the effective precipitiaton at ARDEC 1070, for events less than 3 mm was 0 mm. This is shown by the "P_n=0" in Figure 3.18. Additional research on the effects of the small wetting events on the estimation of the SWD is required.

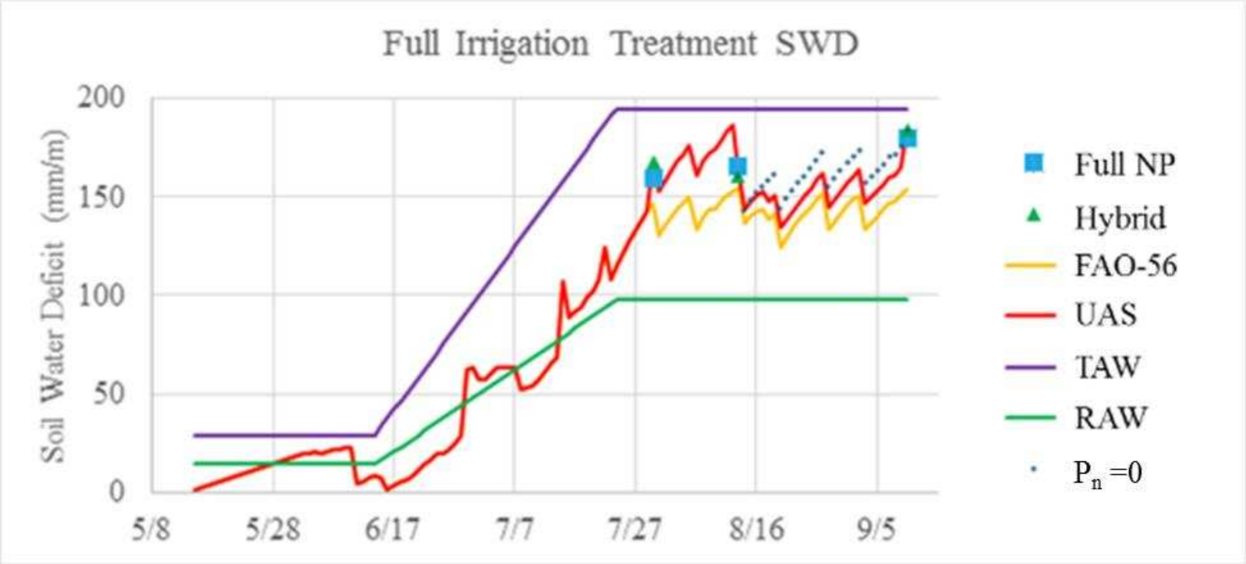

Figure 3.18. Seasonal comparison of the SWD (mm/m) of the UAS adjusted SWB and FAO-56 SWB SWDs for the full irrigation treatments.

The adjusted SWB is a FAO-56 SWB adjusted with the hybrid derived SWD when RS data are available, and the k_{cbrf} are used to adjust the k_c. On average, the adjusted k_{cb} was 17.52% lower than the FAO-56 derived k_{cb}. The relationship between the k_{cb} and the adjust k_{cb} are shown in Figure 3.19. Figure 3.18 depicts the FAO-56 SWB and the Hybrid models estimation of k_{cb} the when compared to the NP data. As the number of RS overpasses increase, the extrapolation of the k_{cbrf} will become more accurate due to the shorter intervals of the calculations. Figure 3.20 shows the spatially distributed k_{cbrf} on 10SEP15.

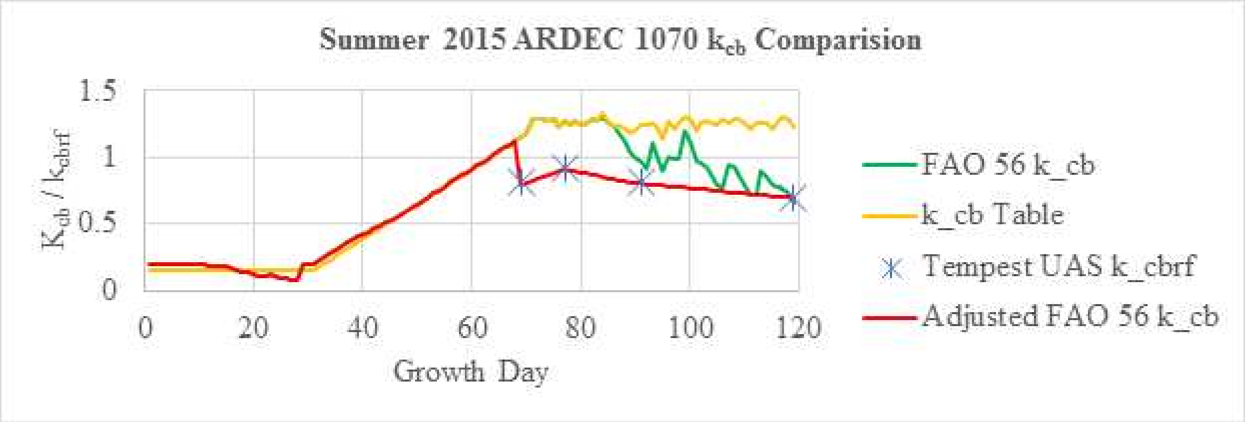

Figure 3.19. Comparison of the full irrigation treatment FAO-56 k_{cb} and the hybrid k_{cbrf} during the summer 2015 ARDEC 1070 RS campaign.

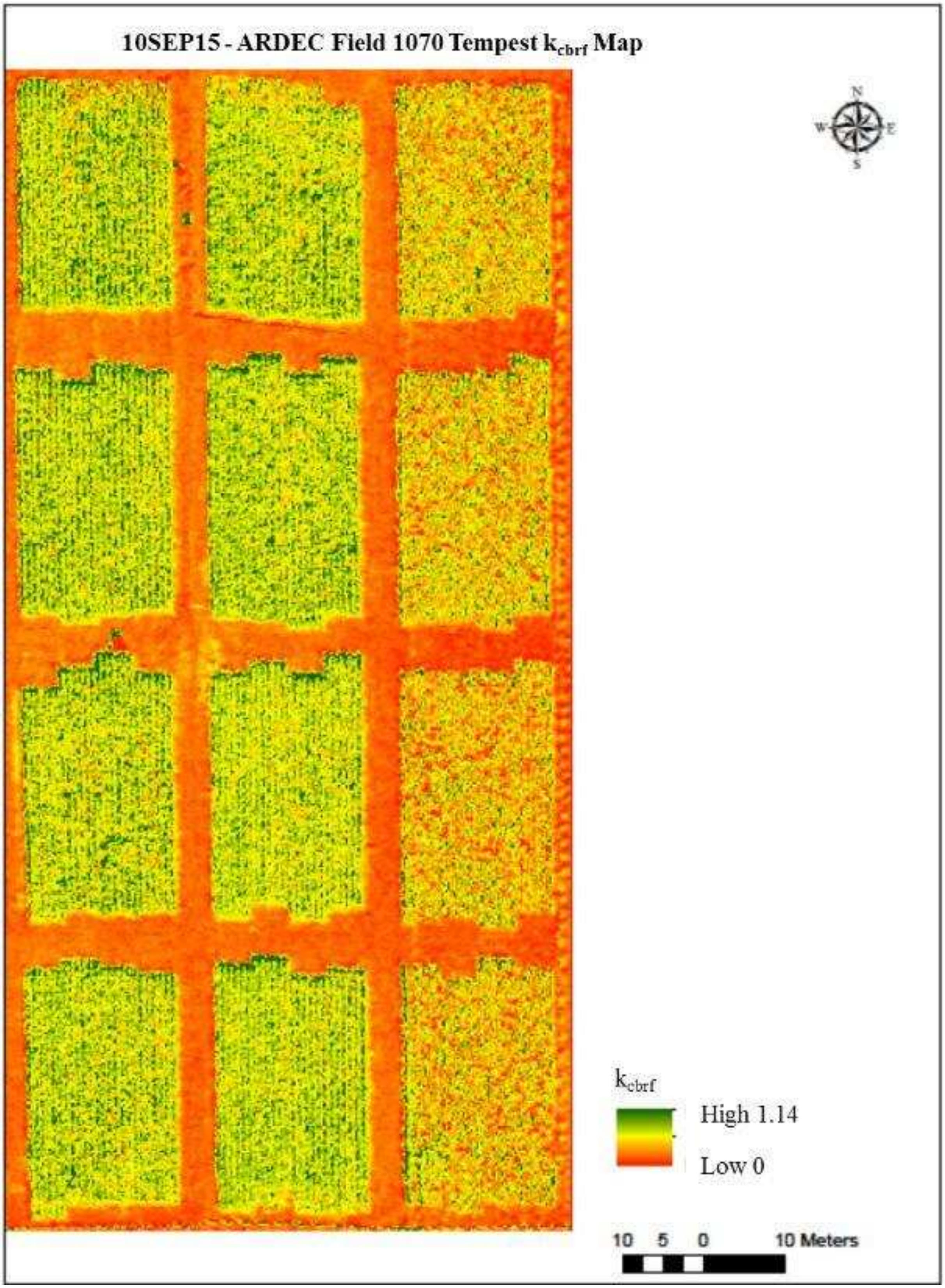

Figure 3.20. Spatially distributed k_{cbrf} map for ARDEC field 1070 on 10SEP15.

As the number of RS overpasses assimilated increases, the accuracy of the UAS adjusted FAO-56 SWB will continue to increase. This allows for greater control of irrigation scheduling in a precision agriculture irrigation program. The end state of the study was the production of a spatially distributed SWD map for use in a PA irrigation program. Figure 3.21 is the ARDEC field 1070 10SEP2015 irrigation map for use in a PA irrigation system. The blocks represent the control zones of a Zone-Controlled SS-VRI System. The colors ranging from blue (85 mm) to red (155 mm) represent the required application amount to return the soil profile to the threshold where $k_s=1$ (θ_t mm/m). In a PA irrigation system, the acceptable stress level of a crop is the driving factor for irrigation. Using the Hybrid method and UAS adjusted FAO-56 SWB, an irrigation planner can accurately track the actual spatially distributed crop water requirements, increasing the efficiency of the irrigation system. The 10SEP15 – ARDEC 1070 SWD inset of Figure 3.21 shows the spatially distributed SWD from the soils field capacity (θ_{FC}).

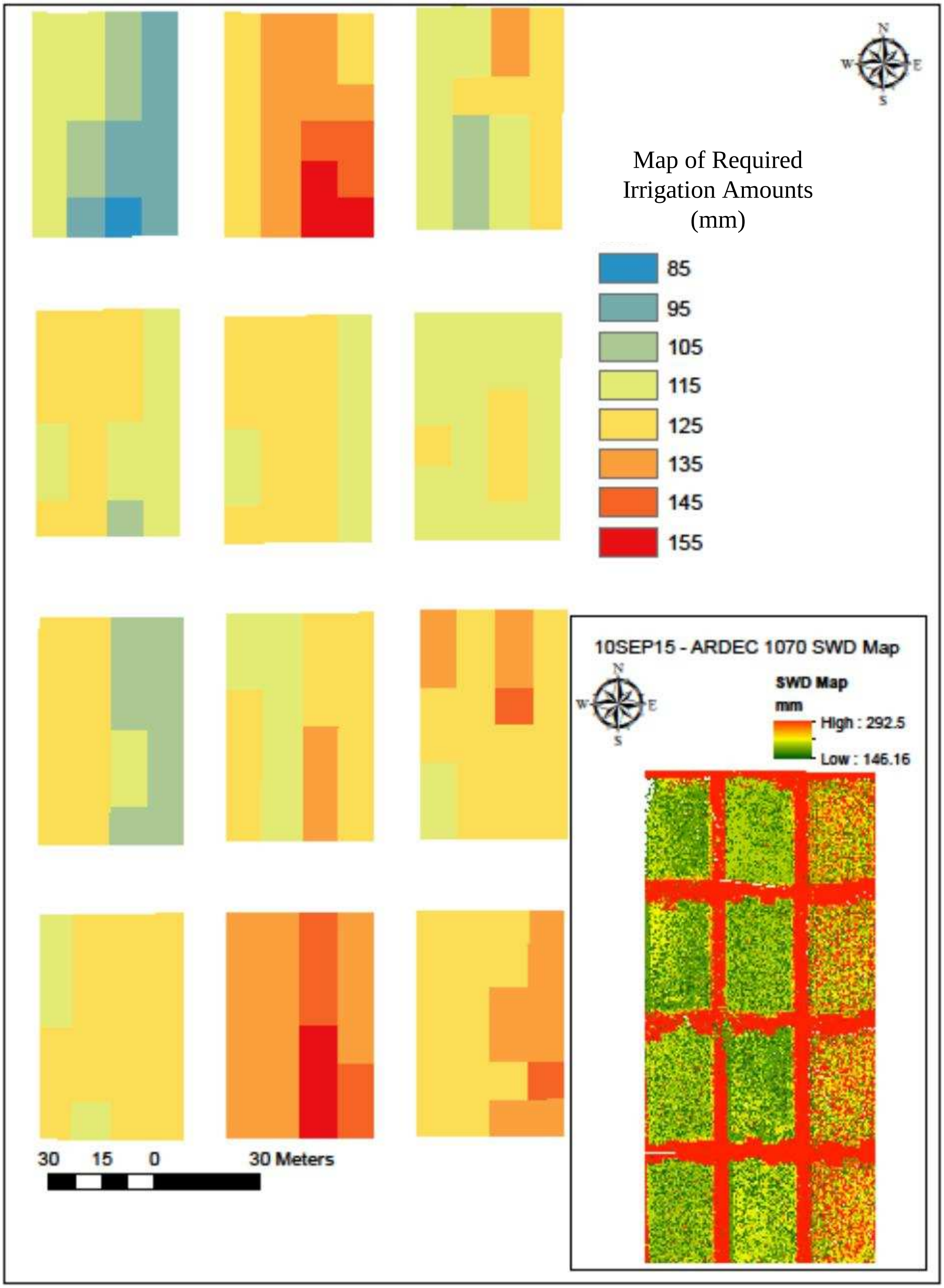

Figure 3.21. 10SEP15 ARDEC field 1070 irrigation requirement map based on the Hybrid SWB Method.

CHAPTER 4: CONCLUSION

Data from the summer 2015 CSU Tempest RS campaign at the CSU ARDEC field 1070 were presented to evaluate the performance of the CSU Tempest UAS RS platforms ability to accurately estimate the spatially distributed spectral reflectance (NIR, red and green), radiometric surface temperature (T_{sfc}), daily evapotranspiration (ET_a) and the root zone SWD. The primary evaluation of the Tempest RS data were divided into three sections. The first section compared the raw RS derived thermal and optical imagery against ground-based measurements using the MRS5 multispectral sensor. The second section compared four method of RS derived ET_a (TSEB, SAT, CWSI and k_{cbrf}) to NP and FAO-56 SWB derived ET_a. The final section evaluated the hybrid method for estimating root zone SWD utilizing the TSEB derived ET_a against the NP and FAO-56 SWB derived SWD. The results and analysis from the study are summarized in accordance with the objectives listed in the introduction.

4.1. Results and Analysis Overview

1. Raw data analysis: The raw thermal, NIR and optical imagery collected during the 2015 CSU Tempest RS campaign agreed well with the data collected using the ground-based multispectral sensor. The RS TIR data had a MBE of -0.52 ^{o}C, RMSE of 5.68^{o}C and NCSE of 0.66 during the campaign due to variations in the operations procedures associated with the thermal sensor. During the last flight of the 2015 campaign, 10SEP15, the TIR RMSE and NSCE were reduced to 2.4^{o}C and 0.92, respectively. The RS derived multispectral imagery (NIR, red, and green), correlated with the ground-based multispectral sensor with RMSE of 5.26%, 3.51% and 7.31%, respectively. The red and NIR RS data strongly agreed with the ground based data with season NSCE of 0.91 and

0.83, respectively. Errors associated with the raw data may be correlated with the low number of ground-based samples, mechanical and procedural malfunctions throughout the campaign, as well as changing and/or non-ideal meteorological and biophysical conditions during the data collection. The accuracy of the raw data will continue to improve as the number overpasses increases and the procedural process are further refined.

2. RS ET_a model evaluation: Of the four RS derived ET_a estimation models evaluated during the study, the TSEB showed the best agreement with the NP derived ET_a, with a MBE of 0.29 mm/d, RMSE of 0.89 mm/d and NSCE of 0.67 over the 2015 campaign period considered. The TSEB and SAT (MBE of 0.49 mm/d, RMSE of 1.21 mm/d and NSCE of 0.19) methods performed better at estimating the daily ET_a than the FAO-56 SWB method (MBE of 0.91 mm/d, RMSE of 1.22 mm/d and NSCE of 0.41). The remote sensing adjusted SWB performed better than the FAO-56 SWB with a MBE of 0.77 mm/d, RMSE of 1.20 mm/d and NSCE of 0.51; showing that even without daily RS overpass the assimilation of RS data into ET_a estimates has the capability of increasing the accuracy of the FAO-56 SWB for use in a PA irrigation system. Errors may be attributed to non-ideal meteorological (i.e., wet soil surface from morning dew), and biophysical (root zone depth, plants that are not actively ETing, etc.) variations at the test location, as well as the errors associated with the raw RS data.

3. SWD estimation: Utilizing the TSEB derived ET_a and the Hybrid SWD model produced promising agreement with the NP derived SWD estimates. The hybrid method had a MBE of -2.45 mm/m, RMSE of 20.20 mm/m and NSCE = 0.86 throughout the campaign with a correlation using the T-Test with a probability of 0.24 when using $\alpha=0.05$. The RS

adjusted SWB also had strong agreement with the NP with a RMSE of 26.22 mm/m and a probability 0.23. The FAO-56 SWB had less agreement with the NP with a MBE of -22.96 mm/m, RMSE value of 33.59 mm/d and NSCE of 0.37. The errors associated with the hybrid model SWD are attributed to the errors of the raw RS data and ET_a calculations, as well as the physical characteristics of the study site. The errors caused by the physical characteristic are apparent in the drought treatments, where the NP SWC levels were artificially high due to the preferential water infiltration paths associated with the dry soil cracking and NP access tubes. The degree of agreement of the RS derived ET_a shows that utilizing the RS data to adjust the SWB is a viable procedure for use in PA irrigation management systems.

4. CSU Tempest operations: Throughout the study, the operational and approval procedures of conducting research with the CSU Tempest have continually evolved. The COA application process has been implemented by two additional departments at CSU. The Tempest RS platform is prepared to conduct weekly RS overpasses at the ARDEC and other alternative test locations during the summer of 2016. Currently, the Tempest has two approved COAs, with one pending approval, in western and southern Colorado for the 2016 campaign.

4.2. Recommendations for future research

Future studies should focus on several area of research with the Tempest UAS. The first area of focus are the operational and collection procedures of the Tempest UAS RS platform. As a preliminary study of the Tempest UAS RS platform, the operational and collection procedures were continually refined throughout the campaign as malfunctions occurred with the systems. Due to the high number of malfunctions during the summer of 2015, there is room for improvement of the data collection process. The second area of focus is the data processing of the raw Tempest data. During the study, the raw Tempest data were not spectrally, geometrically or optically corrected, which caused both spectral and geometric distortions that contributed to the overall error of the system. The sensors on the Tempest UAS have factory spectral calibration, but refined, site specific calibrations are required to increase accuracy of the system. Additionally, the geo-rectification of the raw data were accomplished using manual ground reference points (GRP) in the GIS software. Due to the small size of the ARDEC field 1070 test location, manual geo-rectification was possible. With the ability of the Tempest to collect data over 1,000 acres an hour, the geo-rectification process requires automation. The final area of focus is the application of the techniques over various crops and environmental conditions. A source of error for the RS derived ET_a and SWD are the uncertainty of the crop biophysical characteristics. Further research should focus on more accurately modeling plant characteristics (R_z, crop height, etc.). The study was limited to data collected over a single crop at ARDEC 1070 due to regulatory restraints, available SWD information, equipment malfunctions and weather constraints. One of the strengths of the Tempest is the flexibility to collect data when the opportunity presents itself. During the 2015 campaign, multiple flights occurred under non-standard conditions (i.e. not within two hours or solar noon, high winds, soil surface wet from dew and k_e=0, etc.). Results comparing the data over various crops and environmental conditions will allow refinement of the methods based on the actual conditions, increasing the effectiveness of the UAS platforms in provide frequent data for use in PA.

REFERENCES

Allen, R. G. (1992). “Standard Reference Evapotranspiration Calculations: REF-ET.” ASCE Irrigation and Drainage Proceedings, Water Forum. Page 140-145.

Allen, R. G., et al. (2007b). “Satellite-based energy balance for mapping Evapotranspiration with internalized calibration (METRIC) – Applications.” *J. Irrig. Drain. Eng.*, 133(4), 395–406.

Allen, R. G., M. Tasumi, A. Morse, and R. Trezza. 2004. A Landsat-based energy balance and evapotranspiration model in western U.S. water rights regulation and planning. Irrig. and Drain. Sys. 19(3-4): 251-268.

Allen, R. G., Pereira, L. S., Raes, D., and Smith, M. (1998). Crop evapotranspiration-Guidelines for computing crop water requirements-FAO Irrigation and drainage paper 56. *FAO, Rome*, *300*, 6541.

Allen, R. G., Tasumi, M., and Trezza, R. (2007a). “Satellite-based energy balance for mapping evapotranspiration with internalized calibration (METRIC) - Model.” *J. Irrig. Drain. Eng.*, 133(4), 380–394.

Anderson, M.C., C.M.U. Neale, F. Li, J.M. Norman, W.P. Kustas, H. Jayanthi, J. Chávez. 2004. Upscaling ground observations of vegetation water content, canopy height, and leaf area index during SMEX02 using aircraft and Landsat imagery. Remote Sensing of Environment, 92:447-464.

ASCE-EWRI. (2005). “The ASCE standardized reference evapotranspiration equation.” Report by the American Society of Civil Engineers Task Committee on Standardization of Reference Evapotranspiration, R. G. Allen, I. A. Walter, R. L. Elliot, T. A. Howell, D. Itenfisu.

Bastiaanssen, W.G.M., Menenti, M., Feddes, R.A., Holstlag, A.A.M., 1998. A remote sensing surface energy balance algorithm for land (SEBAL). 1. Formulation. J. Hydrol. 212–213, 198–212.

Bastiaanssen, W.G.M.; Menenti, M.; Feddes, R.A.; Holtslag, A.A.M. “A remote sensing surface energy balance algorithm for land (SEBAL): 1.” Formulation. *J. Hydrol*. 1998, *212–213*, 198–212.

Bastiaanssen, W.G.M.; Pelgrum, H.; Wang, J.; Ma, Y.; Moreno, J.F.; Roerink, G.J.; van der Wal, T. “A remote sensing surface energy balance algorithm for land (SEBAL): 2.” Validation. *J. Hydrol.* 1998, *212–213*, 213–229.

Black C.A. 1965. “Methods of Soil Analysis: Part I Physical and mineralogical properties”. American Society of Agronomy, Madison, Wisconsin, USA.

Carlson, T. Triangle Models and Misconceptions. *International Journals of Remote Sensing Applications*; Volume 3; Issue 3; 2013.

Chávez J.L., C.M.U. Neale, L.E. Hipps, J.H. Prueger, and W.P. Kustas. 2005. Comparing aircraft-based remotely sensed energy balance fluxes with eddy covariance tower data using heat flux source area functions. J. of Hydrometeorology, AMS, 6(6):923-940.

Chávez, J. L., and C. M. U. Neale. 2003. Validating airborne multispectral remotely sensed heat fluxes with ground energy balance tower and heat flux source area (footprint) functions. ASAE-CIGR Meeting Paper No. 033128. St. Joseph, Mich.: ASAE.

Chávez, J. L., C. M. U. Neale, L. E. Hipps, J. H. Prueger, and W. P. Kustas. 2005. Comparing aircraft-based remotely sensed energy balance fluxes with eddy covariance tower data using heat flux source area functions. J. Hydromet. 6(6): 923-940.

Chávez, J. L., P. H. Gowda, T. A. Howell, C. M. U. Neale, and K. S. Copeland. 2009b. Estimating hourly crop ET using a two-source energy balance model and multispectral airborne imagery. Irrig. Sci. 28(1): 79-91.

Chávez, J. L., P. H. Gowda, T. A. Howell, C. M. U. Neale and K.S. Kopeland. 2009. Estimating Hourly Crop ET Using a Two-Source Energy Balance Model and Multispectral Airborne Imagery. Irrigation Science, Vol. 28, No. 1, pp: 79-91.

Chávez, J. L., T. A. Howell, and K. S. Copeland. 2009a. Evaluating eddy covariance cotton ET measurements in a semiarid advective environment with large weighing lysimeters. Irrig. Sci. 28(1): 35-50.

Chávez, J.L., C.M.U. Neale, J.H. Prueger and W.P. Kustas. 2008. Daily Evapotranspiration estimates from extrapolating instantaneous airborne remote sensing ET values. Irrigation Science J. (2008) 27:67-81.

Chávez, J.L., Gowda, P.H., Howell, T.A., Garcia, L.A., Copeland, K.S., and Neale, C.M.U. 2012. ET mapping with high resolution airborne remote sensing data in an advective semi-arid environment. Journal of Irrigation and Drainage Engineering. ASCE. Vol. 138, No. 5, May 1, 2012. Pp. 416-423.

Chávez, J.L., T.A. Howell, P.H. Gowda, K.S. Copeland, and J.H. Prueger. 2010. Surface Aerodynamic Temperature Modeling over Rainfed Cotton. Transactions of the ASABE, 53(3):759-767.

Chávez, J.L., Taghvaeian, S., Trout, T. J. (2012). Evaluating remote sensing based crop water use monitoring methods using soil moisture sensors. In Proceedings of the 2012 ASABE Annual International Meeting. Paper No. 12-1337502. July 29-August 1, 2012. Dallas, Texas. St. Joseph, MI: ASABE.

DeJonge, K. C., Taghvaeian, S., Trout, T. J., & Comas, L. H. (2015). Comparison of canopy temperature-based water stress indices for maize. *Agricultural Water Management*, *156*, 51-62.

Evans, R. G., King, B. A. (2012) Site-specific sprinkler irrigation in a water limited future. Trans ASABE 55(2):493–504

Evans, Robert G.; LaRue, Jake; Stone, Kenneth C.; and King, Bradley A., "Adoption of site-specific variable rate sprinkler irrigation systems" (2013). Irrig Sci (2013) 31:871–887 DOI 10.1007/s00271-012-0365-x

Finn, M. P. Remote Sensing of Soil Moisture using Airborne Hyperspectral Data. *GI Science and Remote Sensing*; 2011; 48; 4; 522-540.

Gillies, R. R., Kustas, W. P., Humes, K. S. A verification of the 'triangle' method for obtaining surface soil water content and energy fluxes from remote measurements of the Normalized Difference Vegetation Index (NDVI) and surface radiant temperature. *International Journal of Remote Sensing*; 18; 15; 1997.

Gillies, R. R.., Carlson, T. N. Thermal Remote Sensing of surface soil water content with partial vegetation cover for incorporation into climate models. *Journal of Applied Meteorology*; 1995; 34; 745-756.

Gillies, R.T., Carlson, T.N., Cui, J., Kustas, W.P., Humes, K.S., 1997. A verification of the ‘‘triangle’’ method for obtaining surface soil water content and energy fluxes from remote measurements of the Normalized Difference Vegetation Index (NDVI) and surface radiant temperatures. Int. J. Remote Sens. 18 (15), 3145–3166.

Gonzalez-Dugo, M. P., Neale, C. M. U., Mateos, L., Kustas, W. P., Prueger, J. H., Anderson, M. C., and F. Li. 2009. A comparison of operational remote sensing-based models for estimating crop evapotranspiration. Agricultural and Forest Meteorology, 149 (2009) pp1843-1853

Gonzalez-Dugo, M.P., Mateos, L., 2008. Spectral vegetation indices for benchmarking water productivity of irrigated cotton and sugarbeet crops. Agric. Water Manage. 95, 48–58.

Gowda, P. H., Chávez, J. L., Colaizzi, P. D., Evett, S. R., Howell, T. A., and Tolk, J. (2008). “ET mapping for agricultural water management: Present status and challenges.” Irrig. Sci., 26(3), 223–237.

Gowda, P. H., Chávez, J. L., Colaizzi, P.D., Evett, S. R., Howell, T. A., and Tolk, J.A. 2008. ET mapping for agricultural water management: Present status and challenges. Irrig. Sci.26:223 –237.

Gowda, P.H., Howell, T.A., Vinukollu, R., Colaizzi, P.D. and Evett, S. R. 2009b. Evaluation of five surface energy balance approaches for mapping ET us-ing Landsat TM data acquired during BEAREX08. Paper presented at: ASA, CSSA, and SSSA Annual Meetings, Pittsburg, PA. 1–5 Nov

Hadjimitsis, D. G., Clayton, C. R., Hope, V. S. (2004). “An assessment of the effectiveness of atmospheric correction algorithms through the remote sensing of some reservoirs.” International Journal of Remote Sensing. 2004, 25, 3651-3674.

Hillel, D. (1998): Environmental Soil Physics, Academic Press, San Diego, CA

Hipps L, Kustas W (2001) Patterns and organisation in evaporation. In: Grayson R, Blo¨schl G (eds) Spatial patterns in catchment hydrology: observations and modeling, chap 5. Cambridge University Press, London.

Hoffman, G. J., R. G. Evans, M. E. Jensen, D. L. Martin, and R. L. Elliott. (2007b). Design and Operation of Farm Irrigation Systems. 2nd ed. American Society of Agricultural and Biological Engineers. (2007)

Huete, A. R. (1988). A Soil-Adjusted Vegetation Index (SAVI). *Remote Sensing of Environment* 25: 295-309.

Huisman, J. A., Hubbard, S. S., Redman, J. D., & Annan, A. P. (2003). Measuring soil water content with ground penetrating radar. Vadose zone journal, 2(4), 476-491.

Hunt, E. R., Daughtry, C. S. T., Mirsky, S. B., Hively, W.D. Remote sensing with unmanned aircraft systems for precision agriculture applications. *Second International Conference on Agro-Geoinformatic;* 2013.

Idso, S.B.; Jackson, R.D.; Pinter, P.J.Jr.; Reginato, R.J.; Hatfield, J.L. Normalizing the stress degree day parameter or environmental variability, *Agric. Meteorol.* **1981**, *24*, 24-45.

Kustas, W. P., J. G. Alfieri, M. C. Anderson, P. D. Colaizzi, J. H. Prueger, S. R. Evett, C. M.U. Neale, A. N. French, L. E. Hipps, J. L. Chávez, K. S. Copeland, T. A. Howell. 2012. Evaluating the two-source energy balance model using local thermal and surface flux observations in a strongly advective irrigated agricultural area, Advances in Water Resources, Volume 50, December 2012, Pages 120-133.

Kustas, W. P., Norman, J. M. (1999) Evaluation of soil and vegetation heat flux predictions using a simple two-source model with radiometric temperatures for partial canopy cover. Agric For Meteorol 94:13–29

Kustas, W. P., Norman, J. M. (2000) A two-source energy balance approach using directional radiometric temperature observations for sparse canopy covered surfaces. Agron J 92:847–854.

Kustas, W.P., Norman, J.M., 1996. Use of remote sensing for evapotranspiration monitoring over land surfaces. Hydrol. Sci. 41, 495–516.

Li, Z.-L., Tang, R., Wan, Z., Bi, Y., Zhou, C., Tang, B., Yan, G., Zhang, X. A Review of Current Methodologies for Regional Evapotranspiration Estimation from Remotely Sensed Data. *Sensors* 2009, *9*, 3801-3853.

Li, Z.L.; Tang, R.; Wan, Z.; Bi, Y.; Zhou, C.; Tang, B.; Yan, G.; Zhang, X. A review of current methodologies for regional evapotranspiration estimation from remotely sensed data. *Sensors* 2009, *9*, 3801–3853.

Mahrt, L., and D. Vickers. 2004. Bulk formulation of the surface heat flux. Boundary-Layer Meteorol. 110(3): 357-379.

Mcebisi Mkhwanazi, José L. Chávez , Allan A. Andales and Kendall DeJonge, 2015, SEBAL-A: A remote sensing ET algorithm that accounts for advection with limited data. Part II: Test for transferability, Remote Sensing, accepted on 18 Sept 2015. Published 10 Nov. 2015. Remote Sens. 2015, 7(11), 15068-15081; doi:10.3390/rs71115068

Mcebisi Mkhwanazi, José L. Chávez , and Allan A. Andales, 2015, SEBAL-A: A remote sensing ET algorithm that accounts for advection with limited data. Part I: Development and validation, Remote Sensing, accepted on 3 Nov 2015. Published 10 Nov. 2015. Remote Sens. 2015, 7(11), 15046-15067; doi:10.3390/rs71115046

McLoud, P.R., R. Gronwald, and H. Kuykendall. 2007. Precision Agriculture: NRCS Support for Emerging Technologies, Agronomy Technical Note No. 1. East National Technology Support Center, Natural Resources Conservation Service, Greensboro, NC.

Moran, M.S., Clarke, T.R., Inoue, Y., Vidal, A., 1994. Estimating cropwater deficit using the relation between surface-air temperature and spectral vegetation index. Remote Sens. Environ. 49, 246–263.

Moriasi DN, Arnold JG, Van Liew MW, Bingner RL, Harmel RD, Veith TL (2007) Model evaluation guidelines for systematic quantification of accuracy in watershed simulations, Trans. ASABE, 50(3): 885-900.

Nash JE and Sutcliffe JV (1970) River flow forecasting through conceptual models part 1- A discussion of principles. Journal of Hydrology, 10 (3): 282-290.

NASA Landsat. NASA Landsat mission page: (http://www.nasa.gov/mission_pages/landsat/spacecraft/index.html#.VmnsE_krKUk).

Neale, C. M., Hatim, M. E. Geli,. Kustas, W. P., Alfieri, J. G., Gowda, P. H., Evett, S. R., Prueger, J. H., Hipps, L. E., Dulaney, J. P., Chávez, J. L., French, A. N., and Howell, A. Soil water content estimation using a remote sensing based hybrid evapotranspiration modeling approach. *Advances in Water Resources*; 50; December 2012: 152-161.

Neale, C. M., Jayanthi, H., Wright, J.l.. Irrigation water management using high resolution airborne remote sensing. *Journal of Irrigation and Drainage System*; Volume 19; 2005; 321-336.

Neale, C.M.U., Bausch, W.C., Heermann, D.F., 1989. Development of reflectance-based crop coefficients for corn. Trans. ASAE 32 (6), 1891–1899.

Norman, J. M.; Kustas, W. P.; Humes, K. S. Source approach for estimating soil and vegetation energy fluxes in observations of directional radiometric surface temperature. *Agric. For. Meteorol*. 1995, *77*, 263–293.

Norman, J.M., Kustas, W. P., Humes, K. S. (1995) A two-source approach for estimating soil and vegetation energy fluxes form observations of directional radiometric surface temperature. Agric Forest Meteorol 77:263–293

Petropoulos, G. P. Remote Sensing of Energy Fluxes and Soil Moisture Content. (2014). CRC Press, New York.

Postel, Sandra. “Pillar of Sand: Can the Irrigation Miracle Last?” Norton and Company, New York, 1999. Postel S (1999) Pillar of sand: can the irrigation miracle last? Worldwatch Books, W. W. Norton & Co, New York, 312 p

Rydlund, P.H., Jr., and Densmore, B.K., 2012, Methods of practice and guidelines for using survey-grade global navigation satellite systems (GNSS) to establish vertical datum in the United States Geological Survey: U.S. Geological Survey Techniques and Methods, book 11, chap. D1, 102 p. with appendixes.

Sellers, P. J. 1992. Biophysical models of land surface processes. In: Climate System Modeling K.E. Trenberth (ed.). Cambridge University Press, Cambridge, UK, 451-490.

Seneviratne, S. I., T. Corti, E. L. Davin, M. Hirschi, E. B. Jaeger, I. Hehner, B. Orlowskey, and A. J. Teuling (2010): Investigating soil moisture-climate interactions in a change climate: a review, Earth Sci. Rev., 99, 125-161.

Shiklomanov, I.A. (1993). World Fresh Water Resources. In P. H. Gleick (ed.), Water in Crisis: A Guide to the World’s Freshwater Resources. New York, Oxford University Press

Shuttleworth WJ, Gurney RJ, Hsu AY, Ormsby JP (1989) FIFE: the variation in energy partition at surface flux sites. Int Assoc Hydrol Sci (IAHS) Publication 186: 67–74

Topp, G.C., and Ferre, T.P.A. 2002. Water content. In J.H. Dane and G.c. Topp Eds. *Methods of Soil Analysis, part 4- Physical Methods*. Soil Science Society of America, Madison, WI, (417-545.

UNEP (2008), Vital Water Graphics - An Overview of the State of the World’s Fresh and Marine Waters. 2nd Edition. UNEP, Nairobi, Kenya. ISBN: 92-807-2236-0

United Nations, Department of Economic and Social Affairs, Population Division (2015). World Population Prospects: The 2015 Revision, Key Findings and Advanced Tables. New York, United Nations.

Varble, J.L., Chávez, J.L. “Performance evaluation and calibration of soil water content and potential sensors for agricultural soils in eastern Colorado.” *ELSEVIER: Agricultural Water Management*; 101; October 2011: 93-106.

Walthall, C.L., J. Hatfield, P. Backlund, L. Lengnick, E. Marshall, M. Walsh, S. Adkins, M. Aillery, E.A. Ainsworth, C. Ammann, C.J. Anderson, I. Bartomeus, L.H. Baumgard, F. Booker, B. Bradley, D.M. Blumenthal, J. Bunce, K. Burkey, S.M. Dabney, J.A. Delgado, J. Dukes, A. Funk, K. Garrett, M. Glenn, D.A. Grantz, D. Goodrich, S. Hu, R.C. Izaurralde, R.A.C. Jones, SH. Kim, A.D.B. Leaky, K. Lewers, T.L. Mader, A. McClung, J. Morgan, D.J. Muth, M. Nearing, D.M. Oosterhuis, D. Ort, C. Parmesan, W.T. Pettigrew, W. Polley, R. Rader, C. Rice, M. Rivington, E. Rosskopf, W.A. Salas, L.E. Sollenberger, R. Srygley, C. Stöckle, E.S. Takle, D. Timlin, J.W. White, R. Winfree, L. Wright-Morton, L.H. Ziska. (2015). Climate Change and Agriculture in the United States: Effects and Adaptation. USDA Technical Bulletin 1935. Washington, DC. 186 pages.

APPENDIX 1: CSU TEMPEST UAS

1.1. Tempest UAS

The Tempest is a commercial off-the-shelf R/C model aircraft manufactured by UASUSA, based out of Boulder Colorado. It has been modified by the manufacturer to be an unmanned aircraft using a BlackSwift autopilot and integrating three sensors. There are currently 65+ approved COA's for the Tempest UAS. It is defined as a *miniature* unmanned aircraft with a gross take-off weight of 11 lbs, based on ASTM F2395-7 Standard Terminology for Unmanned Aircraft Systems. The very small size and low speed flight of the Tempest UA adds additional safety to the operation of the Tempest UAS since this aircraft has a small kinetic energy and therefore possess very little danger to any structure and significantly reduces the chance of serious injury to any personal on the ground in the event of an accident. In addition, since the UA propulsion is electrically powered, there is no on-board fuel that may contaminate the environment or pose as an accelerant for a fire in an accident.

1.1.1. Airframe Modifications

Modification have been performed on the Tempest UAS by the manufacturer to include the installation of the BlackSwift Autopilot and the addition of remote sensors to collect environmental data. The payload compartment is a modular system designed and tested by the manufacturer. Modifications are such that the aircraft meets the appropriate air worthiness requirements laid out in MIL-HDB-516A.

1.1.2. Tempest UAS Specifications

Figure A.1.1.1. Colorado State Universities Tempest UAS (Photo by CPT Jeffrey Hathaway)

Table A.1.1.1. Tempest UAS Performance Specifications [UASUSA, 2015]

Specifications	
Wingspan	127" (251 mm)
Wing Area	1016 sq in (0.65 sq m)
Empty Weight	10 lbs (4.54 kg)
Nominal GTOW	11 lbs (5 kg)
Maximum GTOW	20 lbs (9.07 kg)
Wing Loading	20.6 oz/sq ft
Length	61.375" (1524 mm)
Airfoil	MH-32
Center of Gravity	3.5" from leading edge of the wing (89mm)
Stall Speed	20 mph
Cruise Speed	50 mph
Max Speed	100 mph
Max Range	60 mi (52.14 NM)
Radio Range	10 mi (8.69 NM)
Flight Time	1.5 HR

1.1.3. Tempest Sensors

Table A.1.1.2. Tempest UAS Sensor Performance Specifications

Sensor	**nm**		**µm**		**Wavelength**	**130 m (AGL) Resolution**
FLIR TAU 2	7500	13,500	7.5	13.5	Thermal	11.76 cm
Tetracam SNAP ADC	520	920	0.52	0.92	green, red, NIR	6.5 cm
Sony A6000	390	780	0.39	0.78	Visible (RBG)	9.5 cm

Table A.1.1.3. Tempest UAS Sensor Field of View Specifications for Operations Flight.

Tempest Sensor Field of View						
Sensor		***Alt***	***150 ft / 45.72 m***	***200ft / 60.96 m***	***300 ft / 91.44 m***	***400 ft / 121.92 m***
	o (deg)	***Rad***	150	200	300	400
Tetra ACD SNAP (4:3)						
HFOV	37.67	0.657465529	102.33	136.44	204.67	272.89
VFOV	28.75	0.50178216	76.89	102.52	153.77	205.03
HPixel Size (1280)	N/A	N/A	0.08	0.11	0.16	0.21
VPixel Size (1024)	N/A	N/A	0.06	0.08	0.12	0.16
FLIR TAU 2						
HFOV- 19	32	0.558505361	86.02	114.70	172.05	229.40
VFOV	26	0.453785606	69.26	92.35	138.52	184.69
HPixel Size (640)	N/A	N/A	0.13	0.18	0.27	0.36
VPixel Size (480)	N/A	N/A	0.14	0.19	0.29	0.38
MSR5						
FOV	11.6	0.202458193	30.47	40.63	81.26	81.26
IRT						
FOV	11	0.191986218	28.89	38.52	77.03	57.77
A6000						
FOV	44	0.767944871	121.21	161.61	242.42	323.22
Pixel Size (1040)	N/A	N/A	0.12	0.16	0.23	0.31

Table A.1.1.4. Tempest UAS Sensor Pixel Specifications for Operations Flight.

Tempest Sensor Pixel Size								
Sensor	***150 ft***		***200ft***		***300 ft***		***400 ft***	
	mm	cm	mm	cm	mm	cm	mm	cm
Tetra ACD SNAP (4:3)								
HPixel Size (1280)	24.37	2.44	32.49	3.25	48.74	4.87	64.98	6.50
VPixel Size (1024)	18.31	1.83	24.41	2.44	36.62	3.66	48.82	4.88
FLIR TAU 2								
HPixel Size (640)	40.97	4.10	54.62	5.46	81.94	8.19	109.25	10.92
VPixel Size (480)	43.98	4.40	58.64	5.86	87.96	8.80	117.28	11.73
A6000								
Pixel Size (1040)	35.52	3.55	47.36	4.74	71.05	7.10	94.73	9.47

1.1.3.1. FLIR TAU 2

Figure A.1.1.2. FLIR TAU 2 640 Thermal Sensor

http://www.flir.com/cvs/cores/view/?id=54717

Spectral Bands: 7.5-13.5 µm

Dimensions: 1.75x1.75x1.18 IN

Weight: 90 grams

1.1.3.2. Tetracam ADC SNAP

Figure A.1.1.3. Tetracam ADC SNAP Multispectral Sensor

http://www.tetracam.com/Products-orig.htm

Spectral Bands: 520-920 nm (red, green, NIR)

Dimensions: 75x59x33 mm

Weight: 90 grams

1.1.3.3. Sony A6000

Figure A.1.1.4. Sony A600 SLR Digital Camera.

http://store.sony.com/-alpha-6000-mirrorless-interchangeable-lens-camera-zid27-ILCE6000//cat-27-catid-All-Alpha-a6000-Cameras;pgid=RUNyCXbEGC5SRpdVGsMRP1SH0000wKYKreeW;sid=bdnOOLCSnuvdOeQaDFOpPIKYKxg1BVAknVB-sTtG?vva_ColorCode=BC008

Lens: 30 mm fixed

Spectral Bands: 520-920 nm (red, green, blue)

Dimensions: 120x67x45 mm

Weight: 344 grams

1.1.4 Communications and Data Link

The SwiftPilot includes a datalink that is built on the Digi Xtend Frequency Hopping, Spread Spectrum (FHSS) radio modem from Digi International. The datalink has up to 115.2 Kbps throughput and is used for command and control, autopilot telemetry and features a user-configurable retry and acknowledgement error handling scheme. The Digi Xtend operates in the 902-928 MHz ISM frequency band with a maximum 1 Watt output power.

The system is expected to have a communication range of 12 miles line-of-sight with the vertically installed quarter-wave antenna used on the Tempest, and the Ground Control Station (GCS) antenna located at the launch/recovery site. The radio provides security, reliability and high tolerance to interference.

The ground control station consists of the SwiftStation provided by Black Swift Technologies, a pilot console, and an Android Tablet running the SwiftPilot User Interface. The following is an overview of these components containing excerpts from the “SwiftPilot User's Guide.” (http://www.blackswifttech.com)

The SwiftStation manages the communication link to the avionics systems, interfaces to Android Tablet, and provides a command and control stream to the UA. In addition, the SwiftStation includes a GPS receiver and antenna that locates the position of the ground station.

The SwiftStation is powered through an external 12V DC source, provided by a 120 V AC power supply adapter. This provides power to run the ground station. The SwiftStation allows for a 12V battery connection as well for when no convenient AC source is available to power the unit.

The SwiftStation connects to the tablet based user interface through a standard WiFi link. The ground station GPS antenna is connected to the external USB connector and the ground station UHF antenna is hooked up to through an SMA connector.

The pilot's console is a standard R/C style handset that is used for manually piloting the UA through an on-board receiver. The pilot console can be operated without the use of the SwiftStation through an on board multiplexer that selects control between the pilot console and the autopilot. This on-board multiplexer between the autopilot and pilot console is an extra layer of redundancy.

The Black Swift User Interface is a software application that runs on an Android Tablet and provides a command and control interface for the operator when the aircraft is in semi-autonomous mode. All of the SwiftPilot system features are accessible from this interface. This includes, but is not limited to, planning and loading waypoint flight plans, monitoring the health and status of the UA and the SwiftStation, and providing a graphical command and control touch interface for the operator. A screen shot is provided in Figure A.1.1.5.

Figure A.1.1.5. Blackswift SwiftStation.

The main features of the user interface include a moving map display over geo-referenced maps and satellite images, conveniently displayed health indicators in an aircraft status toolbar, an aircraft actions toolbar giving critical status information and control of the UA.

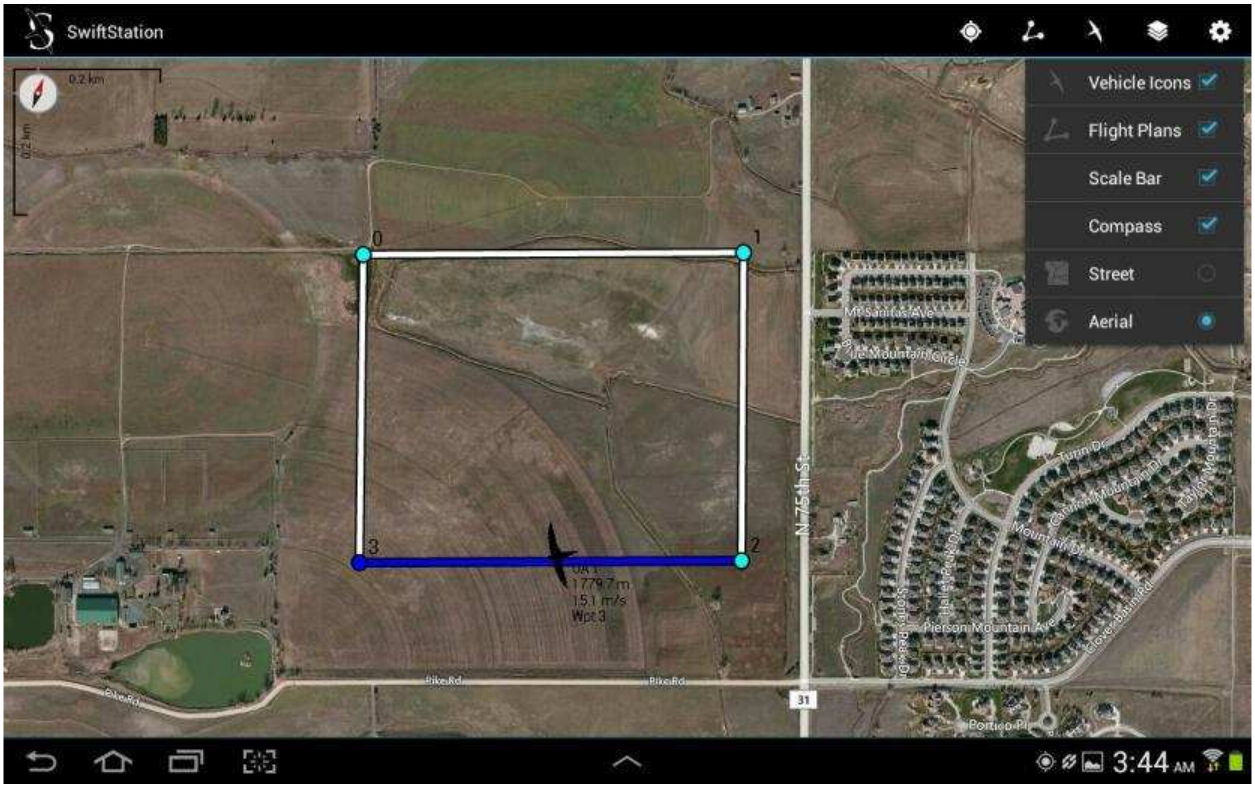

Vehicle Icons ☑
Flight Plans ☑
Scale Bar ☑
Compass ☑
Street ○
Aerial ●

Figure A.1.1.6. Screen shot of Black Swift User Interface.

1.2. Overview of the CSU Pilot Certification Program

The CSU Tempest UAS Training Program is designed to train and certify CSU Pilots on the Tempest UAS until the FAA releases their improved UAS guidance in FY 2016 or FY 2017. The FAA Certifications will be the baseline licensing until the new UAS guidance is released. This will ensure that CSU remains within the FAA Regulations during the transition period. The Flight Training Program was developed with UASUSA, the manufacturer of the Tempest UAS. The CSU Flight Training Program can be found at the CSU website [http://www.engr.colostate.edu/faculty-staff/profiles.php?id=194. The Flight Training will occur over several phases. Initial flight training will be conducted on a user-friendly foam R/C aircraft. This will ensure that any damage of the aircraft during training will be easily repairable and inexpensive. Once the basic flight skills are mastered on the initial trainer, the Pilot-in-Training

(PIT) will advance to a foam R/C aircraft that mimics the flight controls of the Tempest UAS. The Final stage of the flight training will be on the Tempest aircraft as the assistant pilot and finally the Pilot-in-Charge (PIC). The flight training schedule is based on the proficiency of the pilot at each stage of training. The stated time requirements are the minimum required for each Phase. Prior to moving onto the next phase of flight training, all PIT will demonstrate their proficiency with the current airframe. The requirements for certification are as follows:

- Completion of the flight training for pilot to be certified as a PIC
- Completion of the Online Ground School
- Certification of passing the Airman's Written Knowledge Exam
- FAA Class 2 Medical

1.3. CSU ARDEC RS Reference Markers

Figure A.1.1.7. Spectralon White Reflectance Target [Spectrolon 24 in x 24 in White Target, Labsphere, North Sutton, NH]. The white reflectance target sat at an elevation of 36 inches above ground level.

Figure A.1.1.8. Black Reflectance Target. 4’ x 4’ plywood painted black. The black reflectance target sat at an elevation of 12 inches above the ground.

Figure A.1.1.9. ARDEC 1070 Soil Target. Located in the buffer of the field.

APPENDIX 2: REMOTE SENSING ALGORITHMS

2.1. Surface Energy Balance for Land (SEBAL)

The SEBAL model [Bastiaanssen et al., 1998a, 1998b] was developed to establish a pixel by pixel relationship between the surface and air temperature (dT) as a linear relationship between the hot and cold radiometric surface temperature pixel of a RS image. The surface radiometric temperature is used instead of the aerodynamic temperature due to the difficulty in estimating the aerodynamic temperature, both with RS and physical measurements. The hot pixel is define as a dry agricultural surface in the image, while the cold pixel is defined as a well-watered, fully ETing agricultural field. At the cold pixel, the sensible heat flux (H_w) is assumed to be 0, the dT_w=0 and the latent heat:

$$LE = R_n - G \tag{A.2.1.1}$$

While at the hot pixel, the latent heat (LE_d) is assumed to be 0, H_d:

$$H_d = R_n - G \tag{A.2.1.2}$$

The dT_d is calculated as a function of H_d:

$$dT_d = \frac{H_d \times r_{ah}}{\rho \times C_p} \tag{A.2.1.3}$$

The linear relation of the radiometric surface temperature and the air temperature is calculated using the hot and cold anchor points and the linear relationship:

$$dT = a + b \times T_s \tag{A.2.1.4}$$

The pixel by pixel sensible heat flux (H) is then calculated based on the dT and the aerodynamic resistance (r_{ah}) corrected for atmospheric stability using Eq. (2.6):

The SEBAL method is effective at estimating ET_a over homogenous surfaces, and when there are clearly defined hot and cold pixels. Recently, the SEBAL method has been adjusted for advective conditions in Mkhwanazi et al. (2015). For actual conditions that do not have the stated conditions, SEBAL can experience large errors, upwards of 35% [Gowda et al., 2008]. Due to the requirement of the extreme temperatures associated with the hot and cold pixel, the SEBAL method is most effective when used with satellite-based remote sensing data.

2.2. Mapping Evapotranspiration at High Resolution with Internal Calibration (METRIC)

The METRIC method [Allen et al,. 2007a , 2007b] is another SEB model that uses the dT to estimate ET_a. The METRIC models was developed using the SEBAL model and utilizes RS data covering the red, NIR and TIR bands of the electromagnetic spectrum, as well as ground-based meteorological data. The METRIC model was developed to address several of issues of the SEBAL method discussed previously. The first difference is that METRIC does not assume the same boundary conditions at the hot and cold pixels as SEBAL does. At the cold pixel, H is not assumed to equal 0 or LE=Rn-G. Instead, LE_{wet} is set to:

$$LE_{wet} = 1.05 \times ET_{ref} \tag{A.2.1.5}$$

And H_w:

$$H_{wet} = R_n - G - LE_{wet} \tag{A.2.1.6}$$

At the hot pixel the LE is not assumed to equal 0, rather the hot pixel conditions are determined using a soil water balance method to estimate LE when a wetting event occurred close to the remote sensing platform overpass. The second major difference is the selection criteria for the hot and cold pixels. The METRIC model requires the selection of the hot and cold pixels from an agricultural pixel with biophysical properties similar to the reference ET [Gowda et al., 2008]. With the changes in the boundary condition and selection criteria of the hot and cold pixels, the METRIC model can be applied to the aerial and satellite-based remote sensing data, due to the high probability of the hot and cold pixels being present in a single agricultural field [Allen, 2002]. Additionally, the METRIC model has an advantage over SEBAL in areas under advective condition [Chávez et al., 2009]. In addition, METRIC requires very good quality hourly weather data to properly scale the dT function.

2.3. Other Methods – Triangle Method

Empirically based methods that compare RS derive VI's, T_{sfc}, albedo, and other, are also used to estimate surface SWC. These methods are based on plotting the RS data and biophysical properties in a scatter plot and making inference based on the shape of the plot [Petropoulos et al., 2009a]. The most common of these methods is the Triangle method [Gillies and Carlson, 1995] that compares the VI and the T_s to derive the surface SWC [Petropoulos et al., 2009a].

The VI vs T_s creates a triangle (or trapezoid) if the scene has the full range of soil moisture values, as depicted in Figure A.2.1. The right edge, known as the dry edge, represents the highest temperatures over the range of VI, which represents vegetation canopy cover from bare soil to full cover. The left edge, or wet edge, represent the cold temperatures over the same range of VI values. The bare soil and fully vegetative ET is then calculated using the Penmen-Monteith, or similar, equation. The location of the pixel on the scatter plot is developed into a crop water stress index, which is then directly related to the surface SWC and indirectly to the root zone SWC [Gillies et al., 2010, Carlson 2013].

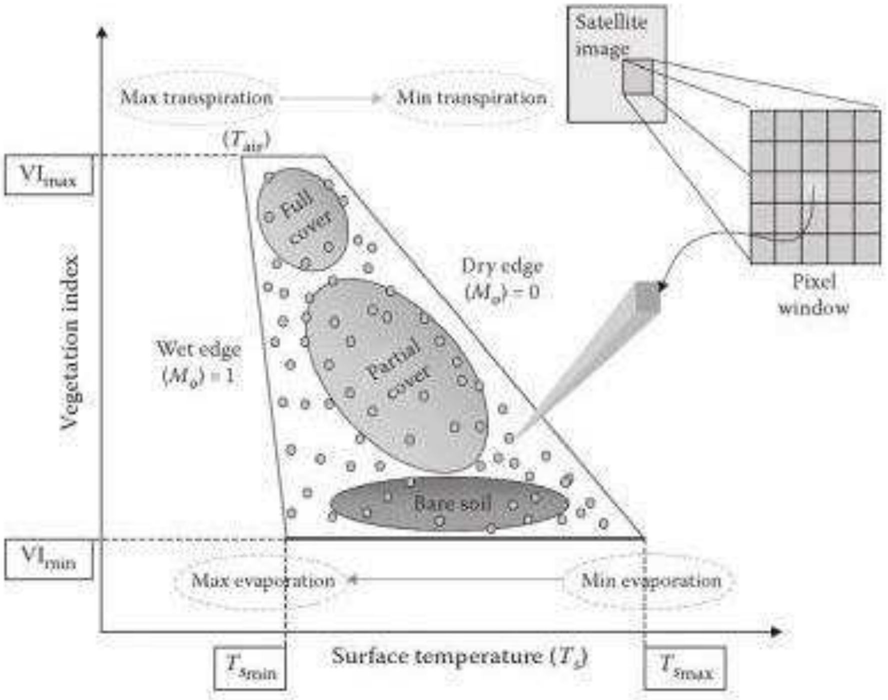

Figure A.2.1. Triangle Method VI vs T_s scatter plot [Petropoulos et al., 2009a].

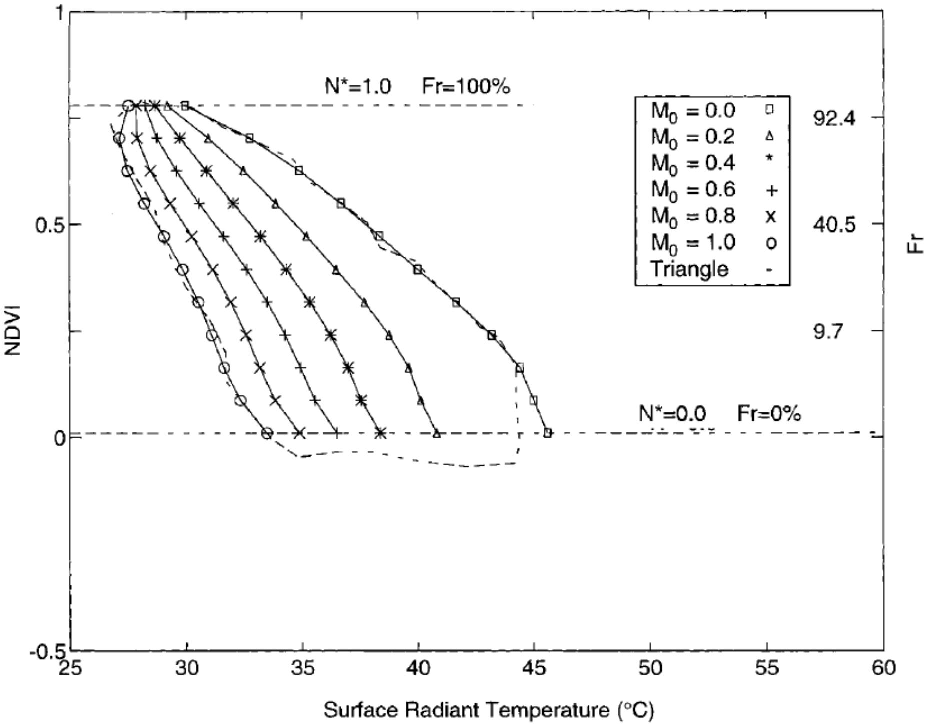

Figure A.2.2. Surface SWC (M_0) utilizing the triangle method [Gillies et al., 2010].

The triangle method is suited to aerial-based remote sensing platform due to the requirement for high spatial resolution multispectral and thermal optical imagery. Additionally, the method shows promise for use over large areas without site-specific tuning. The only ground data that is needed for the triangle method is the soil-water parameters of the imagery and air temperature.

APPENDIX 3: DESCRIPTION OF MODELS USED

3.1. Data Pre-Processing

1.1. Geo-reference Images using ERDAS Imagine 2015 GIS Software [ERDAS Imagine 2015, Hexagon Geospatial, Cape Town, South Africa].

1.2. Mosaic Images using GIS Software utilizing ground reference points and known location data. Attempt to utilize as few RS imagery as necessary to limit errors associated with pre-processing data.

1.3 Calibrate Imagery to reflectance and T_{sfc} using internal calibration. Convert from 8-bit digital number (DN (0-255) to reflectance (% or fraction) or T_{sfc} (^oC or K).

$$MS_{Internal\,Calibration} = 0.0039 \times DN \qquad \text{(A.3.1.1)}$$

$$T_{sfc} = a \times DN + b \qquad \text{(A.3.1.2)}$$

3.2. Two-Source Energy Balance (TSEB) ET_a Method

The following procedure is a description of the TSEB model and corresponding ERDAS Imagine Models. The name of the ERDAS Imagine model is described using the following format: “Reference Number Product.” (e.g. “1 OSAVI”). The ERDAS Imagine Models are located at the CSU website [http://www.engr.colostate.edu/faculty-staff/profiles.php?id=194].

2.1. Calculate OSAVI: Rondeaux et al. (1996). Range [-1:1]. “1 OSAVI”.

$$OSAVI = \frac{(1+L)\times(NIR-RED)}{NIR+RED+L} \qquad \text{(A.3.2.1)}$$

where L=0.16 as the optimal value to minimize soil background effects.

2.2. Calculate the crop height (h_{cc}, m): Chávez et al. (2005). Range [$h_{cc} \geq 0$]. “2 Crops”.

$$h_{cc} = (1.86 \times OSAVI - 0.2) \times (1 + 4.8 \times 10^{-7} \times e^{(17.69 \times OSAVI)}) \qquad \text{(A.3.2.2)}$$

2.3. Calculate Leaf Area Index (LAI): Chávez et al. (2005). Range [$0.5 \leq LAI \leq 5$] “3 LAI_RS”.

$$LAI = (4 \times OSAVI - 0.8) \times (1 + 4.73 \times 10^{-6} \times e^{15.64 \times OSAVI}) \qquad \text{(A.3.2.3)}$$

2.4. Calculate Fraction Vegetation Cover (f_c). Normal et al. (1995). Range [0:1]. “4 f_c”.

$$f_c = 1 - e^{-0.5 \times LAI} \qquad \text{(A.3.2.4)}$$

2.5. Calculate Local LAI (LAI_L). Kustas and Norman (2000). Range [$0.5 \leq LAI \leq 5$]. “5 LAI_l”.

$$LAI_L = \frac{LAI_{rs}}{f_c} \qquad \text{(A.3.2.5)}$$

2.6. Calculate the Fractional Soil Cover (f_s). Kustas and Norman (2000). Range [0:1]. “6 f_s”.

$$f_s = (f_c \times e^{-0.5 \times LAI_L}) + (1 - f_c) \qquad \text{(A.3.2.6)}$$

2.7. Calculate Clumping Factor (Ω). Kustas and Norman (2000). Range [0:1] “7 Clumping Factor”.

$$\Omega = \frac{-LN(f_s)}{0.5 \times LAI} \qquad \text{(A.3.2.7)}$$

2.8. Calculate “New” (updated w/ Ω) Fractional Vegetative Cover (f_{c_new}). Kustas and Norman (2000). Range [0:1]. “7 f_c_new”.

$$f_{c\_new} = 1 - e^{-0.5 \times LAI \times \Omega} \qquad \text{(A.3.2.8)}$$

2.9. Calculate Surface Albedo (α_s). Brest and Goward (1987). Range [0:1]. “8 Surface Albedo”.

$$\alpha_S = 0.512 \times RED + 0.418 \times NIR \tag{A.3.2.9}$$

2.10. Calculate the short wave radiation budget (R_{sw}, W m^{-2}). Range [$R_{sw} \geq 0$]. Inputs: α, R_s. “10 R_sw”.

$$R_{SW} = (1 - \alpha) \times R_S \tag{A.3.2.10}$$

where R_{sw} is the incoming short wave solar radiation (W m^{-2}) from weather station data.

2.11. Calculate ε_{sfc}. Brunsell and Gillies (2002). Range [0:1]. “11 Surface Emissivity”.

$$\varepsilon_{sfc} = f_c \times \varepsilon_v + (1 - f_c) \times \varepsilon_s \tag{A.3.2.11}$$

where vegetation emissivity (ε_v=0.98), and soil emissivity (ε_s=0.955).

2.12. Calculate the surface outgoing long wave radiation (R_{LW_out}, W m^{-2}). “12 R_lw_out”.

$$R_{LW\_out} = \varepsilon_S \sigma T_S^4 \tag{A.3.2.12}$$

where ε_{sfc} is the emissivity of the surface, and Where T_s is the air temperature of the surface (K).

2.13. Calculate the long wave radiation budget (R_{LW}, W m^{-2}). “13 R_lw”.

$$R_{LW} = R_{LW\_in} - R_{LW\_out} \tag{A.3.2.13}$$

2.14. Calculate the Atmospheric/air long wave incoming radiation (R_{LW_in}, W m^{-2}). Excel spread sheet.

$$R_{LW\_in} = \varepsilon_a \sigma T_a^4 \tag{A.3.2.14}$$

where T_a is the air temperature of the air (K), ε_a is the emissivity of the atmosphere, and σ is the Stefan-Boltzmann Constant (5.67E-08 W m^{-2})

2.15. Calculate ε_a. Range [0:1]. Excel spread sheet.

$$\varepsilon_a = 1.24\left(\frac{e_a}{T_a}\right)^{\frac{1}{7}} \tag{A.3.2.15}$$

where e_a is actual vapor pressure of the air (kPa) and T_a is the air temperature of the air (K).

2.16. Calculate Net Radiation (R_n, W m^{-2}). Monteith (1973). "14 R_n".

$$R_n = (1-\alpha)R_s + \varepsilon_a \sigma T_a^4 - \varepsilon_s \sigma T_s^4 \tag{A.3.2.16}$$

2.17. Calculate the extinction coefficient for the canopy (K). Campbell (1996), Campbell and Norman (1998). Excel spread sheet.

$$K = \frac{1}{2 \times COS(\theta_z \times \frac{\pi}{180})} \tag{A.3.2.17}$$

where, θ_z is the solar zenith angle (degrees) and π is 3.1416.

2.18. Calculate the components of theoretical Clear Sky Short Wave Radiation (R_s), Direct Beam Solar Radiation (R_b) and Diffuse Solar Radiation (R_d). Spokas and Forcella, 2006.

$$R_s = R_b + R_d \tag{A.3.2.18}$$

2.18.1. Calculate the Optical Air Mass Number (m). Excel spread sheet.

$$m = \frac{P}{(101.3 \times COS(\theta_z \times \frac{\pi}{180})} \tag{A.3.2.18.1}$$

where P is the barometric pressure (kPa) from weather data.

2.18.2. Calculate R_b. Excel spread sheet.

$$R_b = G_{sc} \times \tau_{atm\_KB} \qquad \text{(A.3.2.18.2)}$$

where G_{sc} is the solar constant (1360 W/m^2) and τ_{atm_KB} is the atmospheric transmittance calculated with REF-ET and Weather Station data [Allen, 1992].

2.18.3. Calculate R_d. Excel spread sheet.

$$R_d = 0.3 \times (1 - (\tau_{atm\_KD})^m) \times G_{sc} \times COS(\theta_z \times \frac{\pi}{180}) \qquad \text{(A.3.2.18.3)}$$

where τ_{atm_KD} is the atmospheric transmittance calculated with REF-ET and Weather Station data [Allen 1992].

2.19. Calculate the fraction (f_b) of incident Photosynthetically Active Radiation (PAR) from R_b. Range [0:1]. Goudriaan (1977). Excel spread sheet.

$$f_b = \frac{R_b}{R_b + R_d} \qquad \text{(A.3.2.19)}$$

2.20. Calculate the solar transmittance in the canopy (τ_c). Range [0:1]. Norman and Jarvis (1974). "15 Tau_c".

$$\tau_c = \frac{e^{A \times (1 - 0.47 \times f_b)} \times LAI_{rs}}{(((1 - \frac{1}{2k}) \times f_b) - 1)} \qquad \text{(A.3.2.20)}$$

2.20.1. Where A is (Goudriaan (1988)). Excel spread sheet.

$$A = 0.283 + 0.785 \times a + 0.159 \times a^2 \qquad \text{(A.3.2.20.1)}$$

where a=0.9. (DECAGON USERS MANUAL)

2.21. Calculate the initial Canopy Net Radiation (dR_n, W m^{-2}). Normal et al. (1995). Inputs: R_n and f_{c_new}. “16 dR_n”.

$$dR_n = R_n - (R_n \times e^{0.9 \times LN(1 - f_{c\_new})}) \qquad \text{(A.3.2.21)}$$

2.22. Calculate the Slope of the saturation vapor pressure versus temperature curve (Δ). Priestly and Taylor (1972). Excel spread sheet.

$$\Delta = \frac{2503 \times e^{(\frac{17.27 \times T}{T+273.3})}}{(T+273.3)^2} \qquad \text{(A.3.2.22)}$$

2.23. Calculate the psychrometric constant (γ). Priestly and Taylor (1972). Excel spread sheet.

$$\gamma = 0.000665 \times P \qquad \text{(A.3.2.23)}$$

2.24. Calculate the fraction of LAI that is green (f_g). Range [0:1]. Based on ground observations or as a function of OSAVI.

$$f_g = \begin{matrix} 0.98, OSAVI > 0.5 \\ 0.94, 0.25 > OSAVI \geq 0.5 \\ 0, OSAVI \leq 0.25 \end{matrix} \qquad \text{(A.3.2.24)}$$

2.25. Calculate the initial Sensible Heat Flux for Canopy (H_{c_int}, W m^{-2}). Priestly and Taylor (1972). Inputs: dR_n and f_g. “18 dR_n”.

$$H_{c\_\mathrm{int}} = dR_n \times (1 - (1.13 \times f_g \times \frac{\Delta}{\Delta + \gamma})) \qquad \text{(A.3.2.25)}$$

2.26. Calculate the initial aerodynamic resistance to heat transfer (rah_{int} s m^{-1}). Norman et al. (1995). “19 r_ah_int”

$$r_{ah} = \frac{LN(\frac{z_m - d}{z_{om}}) \times LN(\frac{z_m - d}{z_{oh}})}{U^* \times k^2} \quad \text{(A.3.2.26)}$$

where, z_m is the height of the wind speed measurement (m), d is the zero plane displacement (m), z_{om} is the roughness length for momentum (m) and z_{oh} is the roughness length for heat transfer (m).

2.27. Calculate the friction velocity (U^*, m s^{-1}). Norman et al. (1995). “20 iteration”.

$$U^* = \frac{U \times k}{LN(\frac{Z_m - d}{Z_{om}})} \quad \text{(A.3.2.27)}$$

2.28. Calculate the initial canopy temperature (T_{c_int}, K). Norman et al. (1995). “20 iteration”.

$$T_{c\_in} = \frac{(H_{c\_in} \times r_{ah})}{\rho_a \times Cpa} + T_a \quad \text{(A.3.2.28)}$$

2.29. Correct H_{c_int} for atmospheric stability using the Monin-Obukhov length Scale (L_{mo}, m). This is an iterative process, until the change in H_{c_int} is less than 5%. Norman et al. (1995). “20 iteration”.

$$H_{c\_in} = \frac{\rho_a \times Cpa \times (T_{c\_\text{int}} - T_a)}{r_{ah}} \quad \text{(A.3.2.29)}$$

$$L_{mo} = \frac{-u^3 \times T_a \times \rho_a C_{Pa}}{g \times k \times H} \quad \text{(A.3.2.30)}$$

The friction velocity (U^*), for non-neutral is derived using the stability correction for momentum and heat transfer (ψ_m, ψ_h). The stability correction factor for atmospheric heat transfer and momentum transfer, for unstable conditions (L_{M_O}<0), can be determined by

Businger-Dyer formulations (Dyer and Hicks, 1970; Dyer, 1974; Businger, 1988; Sugita and Brutsaert, 1990) and explained in detail in Chávez et al. (2005). “20 iteration”.

$$x_{Z_m} = (1-16\times\frac{Z_m-d}{L_{mo}})^{1/4} \tag{A.3.2.31}$$

$$x_{Z_{oh}} = (1-16\times\frac{Z_{oh}-d}{L_{mo}})^{1/4} \tag{A.3.2.32}$$

$$\psi h_{Z_m} = \begin{array}{l} 2\times LN(\frac{1+x_{Z_m}{}^{2}}{2}), L_{mo} < 0 \\ -5\times(\frac{Z_m-d}{L_{mo}}), L_{mo} = 0 \end{array} \tag{A.3.2.33}$$

$$\psi h_{Z_{oh}} = \begin{array}{l} 2\times LN(\frac{1+x_{Zoh}{}^{2}}{2}), L_{mo} < 0 \\ -5\times(\frac{Z_{oh}-d}{L_{mo}}), L_{mo} = 0 \end{array} \tag{A.3.2.34}$$

$$\psi m_{Z_{om}} = 2\times LN(\frac{1+x_{Zom}}{2}) + LN(\frac{1+x_{Zom}{}^{2}}{2}) - 2\times ATAN(x_{Zom}) + \frac{\pi}{2} \tag{A.3.2.35}$$

$$\psi m_{Z_m} = 2\times LN(\frac{1+x_{Z_m}}{2}) + LN(\frac{1+x_{Z_m}{}^{2}}{2}) - 2\times ATAN(x_{Z_m}) + \frac{\pi}{2} \tag{A.3.2.36}$$

$$U^{*} = \frac{U\times k}{LN(\frac{Z_m-d}{Z_{om}}) - \psi m_{Z_m} \times LN(\frac{Z_m-d}{L_{mo}}) + \psi m_{Z_{om}} \times LN(\frac{Z_{om}}{L_{mo}})} \tag{A.3.2.37}$$

$$r_{ah} = \frac{LN(\frac{Z_m-d}{Z_{om}}) - \psi h_{Z_m} \times LN(\frac{Z_m-d}{L_{mo}}) + \psi h_{Z_{oh}} \times LN(\frac{Z_{oh}}{L_{mo}})}{U^{*}\times k} \tag{A.3.2.38}$$

2.30. Calculate initial soil temperature (T_{s_in}, ^{o}C)). Normal et al. (1995). “21 T_s_in”.

$$T_{s\_in} = \sqrt[4]{\frac{(T_{sfc} - 273.15)^4 - (f_{c\_new} \times T_{c_{in}})^4}{1 - f_{c\_new}}} \tag{A.3.2.39}$$

2.31. Calculate the initial long wave radiation emitted by the canopy (L_c, W m^{-2}). Norman et al. (1995). “22 L_c”.

$$L_c = \varepsilon_c \times \sigma \times T_{c_{\mathrm{int}}}^4 \tag{A.3.2.40}$$

where ε_c is the canopy emissivity and is set to 0.98 for healthy green vegetation.

2.32. Calculate the initial long wave radiation emitted by the soil (L_s, W m^{-2}). Norman et al. (1995) “23 L_s”.

$$L_s = \varepsilon_s \times \sigma \times T_{s_{\mathrm{int}}}^4 \tag{A.3.2.41}$$

where ε_s is the soil emissivity and is set to 0.92 for bare soil.

2.33. Calculate Soil Albedo (α_s). Range [0:1]. Post et al. (2000). “24 soil albedo”.

$$\alpha_s = 0.785 \times NIR - 0.745 \times Blue + 0.872 \times Green + 0.01 \tag{A.3.2.42}$$

where the blue is calculated as a function of the green band:

$$Blue = 0.47 \times Green \tag{A.3.2.42.1}$$

The Tetracam SNAP ADC did not collect data over the blue band of the electromagnetic spectrum. In order to develop the required blue band data for the study, a linear regression of the MSR5 blue vs the Tempest green bands. The regression allowed the estimation of the blue band from the green bands. The linear relationship is dependent on the spectral sensitivity and bandwidth associated with the multispectral sensor.

2.34. Calculate the short wave radiation for soil (S_{ns}, W m^{-1}). Kustas and Norman (2000). "25 s_ns".

$$S_{ns} = \tau_c \times (1 - \alpha_s) \times R_s \qquad \text{(A.3.2.43)}$$

2.35. Calculate the long wave net radiation from the canopy (L_{nc}, W m^{-1}). Kustas and Norman (2000). "26 l_nc".

$$L_{nc} = (1 - e^{-k_1 \times \Omega \times LAI_{rs}}) \times (R_{lw_{in}} + L_s - 2L_c) \qquad \text{(A.3.2.44)}$$

where K_1 is the extinction coefficient set to 0.95.

2.36. Calculate the long wave net radiation form the soil (L_{ns}, W m^{-1}). Kustas and Norman (2000). "27 l_ns".

$$L_{ns} = (R_{lw\_in} \times e^{-K_1 \times \Omega \times LAI}) + ((1 - e^{-K_1 \times \Omega \times LAI}) \times L_c) - L_s \qquad \text{(A.3.2.45)}$$

2.38. Calculate the net radiation for the soil (R_{ns}, W m^{-1}). Norman et al. (1995). "28 r_ns".

$$R_{ns} = S_{ns} + L_{ns} \qquad \text{(A.3.2.46)}$$

2.39. Calculate the net radiation for the canopy (R_{nc}, W m^{-1}). Norman et al. (1995). "29 r_nc".

$$R_{nc} = R_n - R_{ns} \qquad \text{(A.3.2.47)}$$

2.40. Estimate the sensible heat flux for the canopy using the R_{nc}. Norman et al. (1995). "30 h_c".

$$H_c = R_{nc} \times (1 - (1.13 \times f_g \times \frac{\Delta}{\Delta + \gamma})) \qquad \text{(A.3.2.48)}$$

2.41. Using Eq. (A.3.2.48), updated the r_{ah} using the Monin-Obukhov iterative procedure outlined in section 2.29. “31 iteration 2”.

2.42. Estimate the mean canopy leaf width (wc, m). For corn, assume the wc is 0.09 m. Chávez et al. (2009).

2.43. Calculate the extinction coefficient for the wind function (a_{ext}). Range [0:1]. Norman et al. (1995). “33 a_ext”.

$$a_{ext} = 0.28 \times ((\Omega \times LAI)^{\frac{2}{3}}) \times (h_{cc}^{\frac{1}{3}}) \times wc^{-\frac{1}{3}} \tag{A.3.2.49}$$

2.44. Calculate the wind speed at the top of the canopy (U_c, m s^{-1}). Norman et al. (1995). “34 u_c”.

$$U_c = U^* \times \frac{LN(\frac{h_{cc} - d}{z_{om}})}{LN(\frac{z_m - d}{z_{om}}) - \Psi_m} \tag{A.3.2.50}$$

2.45. Calculate the wind speed close to the soil surface (U_s, m s^{-1}). Norman et al. (1995). “35 u_s”.

$$U_s = U_c \times e^{-a_{ext} \times (1 - \frac{0.15}{h_{cc}})} \tag{A.3.2.51}$$

2.46. Calculate the resistance to heat flow above the soil surface (r_{so}, s^{-1}). Norman et al. (1995). “36 r_so”.

$$r_{so} = \frac{1}{0.004 + (0.012 \times U_s)} \tag{A.3.2.52}$$

2.47. Compute the soil heat flux (G, W m^{-2}). Chávez et al. (2005). “38 G”.

$$G=(((0.3324+(-0.024\times LAI))\times(0.8155+(-0.3032\times LN(LAI))))\times R_n) \quad \text{(A.3.2.53)}$$

2.48. Estimate the updated canopy temperature (T_c, °C) based on updated H_c and r_{ah}. Norman et al. (1995). “39 t_c”.

$$T_c=\frac{H_c\times r_{ah}}{\rho_a\times Cp_a}+T_a \quad \text{(A.3.2.54)}$$

2.49. Estimate the updated soil temperature (T_s, °C) based on the updated T_c. Noman et al. (1995). “40 t_s”.

$$T_s=\sqrt[4]{\frac{(T_{sfc}-273.15)^4-(f_{c\_new}\times T_c)^4}{1-f_{c\_new}}} \quad \text{(A.3.2.55)}$$

2.50. Calculate the sensible heat flux from the soil (H_s, W m^{-1}). Norman et al. (1995). “41 h_s”.

$$H_s=\frac{\rho_a\times Cpa\times(T_s-T_a)}{r_{ah}+r_{so}} \quad \text{(A.3.2.56)}$$

2.51. Compute the total sensible heat flux (H, W m^{-1}). Norman et al. (1995). “42 h”.

$$H=H_c+H_s \quad \text{(A.3.2.57)}$$

2.52. Estimate the latent heat flux for the soil (LE_s, W m^{-1}). Norman et al. (1995). “43 le_s”.

$$LE_s=R_{ns}-H_s-G \quad \text{(A.3.2.58)}$$

2.53. Verify that T_s and T_c are correct. If $LE_s\geq 0$, then the T_s and T_c are correct. If $LE_s<0$, then the soil is dry. The LE_s is set to 0 and H_s is recalculated as:

$$H_s=R_{ns}-G \quad \text{(A.3.2.59)}$$

Utilizing the new H_s, recalculate T_s and T_c by inverting Eq. (2.56) and then Eq. (2.55). Norman et al. (1995). “44 le_s is less than 0 (T_s and T_c)”.

2.54. Calculate the final H based on results of section 2.53. “45 h_final”.

2.55. Compute the total (soil and canopy) latent heat flux (LE, W m^{-2}). “46 et_i et_d”.

$$LE = R_n - H - G \tag{A.3.2.60}$$

2.56. Compute the hourly actual ET (ET_a, mm hr^{-1}) from the LE. Allen et al. (2007). “46 et_i et_d”.

$$ET_a = \frac{3600 \times LE \times 1000}{\lambda_v \rho_w} \tag{A.3.2.61}$$

where λ_v is the latent heat of vaporization (J kg^{-1}) and ρ_w is the density of water (~1,000 kg m^{-3}).

2.57. Extrapolate the hourly ET_a to the daily ET_a (mm d^{-1}) using the Reference ET Fraction (ET_rF). “46 et_i et_d”.

$$ET_rF = \frac{ET_{a_i}}{ET_r} \tag{A.3.2.62}$$

where ET_r is the ASCE-EWRI reference ET.

$$ET_{a\_d} = ET_rF * ET_{r\_d} \tag{A.3.2.63}$$

*Note: If the soil is dry, but there is surface moisture (dew during an early flight, ect.), the daily ET_a must be adjusted according to FAO-56 SWB derived k_e.

3.3. Surface Aerodynamic Temperature (SAT) ET_a Method

The following procedure is a description of the SAT model and corresponding ERDAS Imagine Models.

3.1. Calculate OSAVI: Rondeaux et al. (1996). Range [-1:1]. “1 OSAVI”.

$$OSAVI = \frac{(1+L)\times(NIR-RED)}{NIR+RED+L} \tag{A.3.3.1}$$

where L=0.16 as the optimal value to minimize soil background effects.

3.2. Calculate the crop height (h_{cc}, m): Chávez et al. (2005). Range [$h_{cc} \geq 0$]. “2 Crops”.

$$h_{cc} = (1.86\times OSAVI - 0.2)\times(1+4.8\times10^{-7}\times e^{(17.69\times OSAVI)}) \tag{A.3.3.2}$$

3.3. Calculate Leaf Area Index (LAI): Chávez et al. (2005). Range [$0.5 \leq LAI \leq 5$] “3 LAI_RS”.

$$LAI = (4\times OSAVI - 0.8)\times(1+4.73\times10^{-6}\times e^{15.64\times OSAVI}) \tag{A.3.3.3}$$

3.4. Calculate the initial aerodynamic resistance to heat transfer (rah_{int} s m^{-1}). Norman et al. (1995). “4 r_ah_int”

$$r_{ah} = \frac{LN\left(\frac{z_m-d}{z_{om}}\right)\times LN\left(\frac{z_m-d}{z_{oh}}\right)}{U^{*}\times k^{2}} \tag{A.3.3.4}$$

where, z_m is the height of the wind speed measurement (m), d is the zero plane displacement (m), z_{om} is the roughness length for momentum (m) and z_{oh} is the roughness length for heat transfer (m).

3.5. Calculate the aerodynamic temperature (T_o, ºC). Chávez et al. (2010). “5 t_o”.

$$T_O = 0.534 \times T_{sfc} + 0.39 \times T_a - 0.224 \times LAI - 0.192 \times U - 1.67 \qquad \text{(A.3.3.5)}$$

3.6. Calculate the initial sensible heat flux (H, W m^{-2}). Norman et al. (1995). “6 H_int”.

$$H = \frac{\rho_a \times Cpa \times (T_O - T_a)}{r_{ah}} \qquad \text{(A.3.3.6)}$$

3.7. Calculate the friction velocity (U^*, m s^{-1}). Norman et al. (1995). “7 Lmo”.

$$U^* = \frac{U \times k}{LN(\frac{Z_m - d}{Z_{om}})} \qquad \text{(A.3.3.7)}$$

3.8 Correct H_{int} for atmospheric stability using the Monin-Obukhov length Scale (L_{mo}, m). This is an iterative process, until the change in H_{c_int} is less than 5%. Norman et al. (1995). “7 Lmo”.

$$L_{mo} = \frac{-u^3 \times T_a \times \rho_a C_{Pa}}{g \times k \times H} \qquad \text{(A.3.3.8)}$$

The velocity (U^*, Eq. (A.3.3.16)), for non-neutral is derived using the stability correction for momentum and heat transfer (ψ_m, ψ_h). The stability correction factor for atmospheric heat transfer and momentum transfer, for unstable conditions (L_{M_O}<0), can be determined by Businger-Dyer formulations (Dyer and Hicks, 1970; Dyer, 1974; Businger, 1988; Sugita and Brutsaert, 1990) and explained in detail in Chávez et al. (2005). “8 iteration”.

$$x_{Z_m} = (1 - 16 \times \frac{Z_m - d}{L_{mo}})^{1/4} \qquad \text{(A.3.3.10)}$$

$$x_{Z_{oh}} = (1 - 16 \times \frac{Z_{oh} - d}{L_{mo}})^{1/4} \qquad \text{(A.3.3.11)}$$

$$\psi h_{Z_m} = \begin{array}{l} 2\times LN(\frac{1+x_{Z_m}{}^2}{2}), L_{mo} < 0 \\ -5\times(\frac{Z_m - d}{L_{mo}}), L_{mo} = 0 \end{array} \tag{A.3.3.12}$$

$$\psi h_{Z_{oh}} = \begin{array}{l} 2\times LN(\frac{1+x_{Zoh}{}^2}{2}), L_{mo} < 0 \\ -5\times(\frac{Z_{oh} - d}{L_{mo}}), L_{mo} = 0 \end{array} \tag{A.3.3.13}$$

$$\psi m_{Z_{om}} = 2\times LN(\frac{1+x_{Zom}}{2}) + LN(\frac{1+x_{Zom}{}^2}{2}) - 2\times ATAN(x_{Zom}) + \frac{\pi}{2} \tag{A.3.3.14}$$

$$r_{ah} = \frac{LN(\frac{Z_m - d}{Z_{om}}) - \psi h_{Z_m} \times LN(\frac{Z_m - d}{L_{mo}}) + \psi h_{Z_{oh}} \times LN(\frac{Z_{oh}}{L_{mo}})}{U^* \times k} \tag{A.3.3.15}$$

$$U^* = \frac{U\times k}{LN(\frac{Z_m - d}{Z_{om}}) - \psi m_{Z_m} \times LN(\frac{Z_m - d}{L_{mo}}) + \psi m_{Z_{om}} \times LN(\frac{Z_{om}}{L_{mo}})} \tag{A.3.3.16}$$

$$r_{ah} = \frac{LN(\frac{Z_m - d}{Z_{om}}) - \psi h_{Z_m} \times LN(\frac{Z_m - d}{L_{mo}}) + \psi h_{Z_{oh}} \times LN(\frac{Z_{oh}}{L_{mo}})}{U^* \times k} \tag{A.3.3.17}$$

3.9. Calculate Surface Albedo (α_s). Brest and Goward (1987). “9 Surface Albedo”.

$$\alpha_S = 0.512\times RED + 0.418\times NIR \tag{A.3.3.9}$$

3.10. Calculate the short wave radiation budget (R_{sw}, W m^{-2}). Inputs: α, R_s. “10 R_sw”.

$$R_{SW} = (1-\alpha)\times R_S \tag{A.3.3.10}$$

where R_{sw} is the incoming short wave solar radiation (W/m^2) from weather station data.

3.11. Calculate ε_{sfc}. Brunsell and Gillies (2002). “11 Surface Emissivity”.

$$\varepsilon_{sfc} = f_c \times \varepsilon_v + (1 - f_c) \times \varepsilon_s \qquad \text{(A.3.3.11)}$$

where vegetation emissivity (ε_v=0.98), and soil emissivity (ε_s=0.955).

3.12. Calculate the surface outgoing long wave radiation (R_{LW_out}, W m^{-2}). “12 R_lw_out”.

$$R_{LW\_out} = \varepsilon_s \sigma T_s^4 \qquad \text{(A.3.3.12)}$$

where ε_{sfc} is the emissivity of the surface, and Where T_s is the air temperature of the surface (K).

3.13. Calculate the long wave radiation budget (R_{LW}, W m^{-2}). “13 R_lw”.

$$R_{LW} = R_{LW\_in} - R_{LW\_out} \qquad \text{(A.3.3.13)}$$

3.14. Calculate the Atmospheric/air long wave incoming radiation (R_{LW_in}, W m^{-2}). Excel spread sheet.

$$R_{LW\_in} = \varepsilon_a \sigma T_a^4 \qquad \text{(A.3.3.14)}$$

where T_a is the air temperature of the air (K), ε_a is the emissivity of the atmosphere, and σ is the Stefan-Boltzmann Constant (5.67E-08 W m^{-2})

3.15. Calculate ε_a. Range [0:1]. Excel spread sheet.

$$\varepsilon_a = 1.24\left(\frac{e_a}{T_a}\right)^{\frac{1}{7}} \qquad \text{(A.3.3.15)}$$

3.16. Calculate Net Radiation (R_n, W m^{-2}). Monteith (1973). “14 R_n”.

$$R_n = (1-\alpha)R_s + \varepsilon_a \sigma T_a^4 - \varepsilon_s \sigma T_s^4 \quad \text{(A.3.3.16)}$$

3.17. Compute the soil heat flux (G, W m^{-2}). Chávez et al. (2005). “15 G”.

$$G = (((0.3324 + (-0.024 \times LAI)) \times (0.8155 + (-0.3032 \times LN(LAI)))) \times R_n) \quad \text{(A.3.3.17)}$$

3.18. Compute the total (soil and canopy) latent heat flux (LE, W m^{-2}). “16 et_i et_d”.

$$LE = R_n - H - G \quad \text{(A.3.3.18)}$$

3.19. Compute the hourly actual ET (ET_a, mm hr^{-1}) from the LE. Allen et al. (2007). “16 et_i et_d”.

$$ET_a = \frac{3600 \times LE \times 1000}{\lambda_v \rho_w} \quad \text{(A.3.3.19)}$$

where λ_v is the latent heat of vaporization (J kg^{-1}) and ρ_w is the density of water (~1,000 kg m^{-3}).

3.20. Extrapolate the hourly ET_a to the daily ET_a (mm d^{-1}) using the Reference ET Fraction (ET_rF). “16 et_i et_d”.

$$ET_r F = \frac{ET_{a_i}}{ET_r} \quad \text{(A.3.3.20)}$$

where ET_r is the ASCE-EWRI reference ET.

$$ET_{a\_d} = ET_r F * ET_{r\_d} \quad \text{(A.3.3.21)}$$

*Note: If the soil is dry, but there is surface moisture (dew during an early flight, ect.), the daily ET_a must be adjusted according to k_e.

3.4. Crop Water Stress Index (CWSI) ET_a Method

The following procedure is a description of the CWSI model and corresponding ERDAS Imagine Model "CWSI".

4.1. Calculate the dT (°C) of the canopy emissivity corrected T_c (°C) and the T_a (°C). Idso et al. (1982).

$$dT = T_c - T_a \tag{A.3.4.1}$$

When utilizing the TIR imagery, the surface temperature (T_{sfc}, °C) is utilized instead of T_c. If the multispectral imagery is available, the T_c can be estimated using the methods outlined in the TSEB model.

4.2. Calculate the vapor pressure difference (VPD, kPa). Idso et al. (1982).

$$VPD = e_s - e_a = 0.6108 \times e^{\frac{17.27 \times T_a}{T_a + 273.15}} - (0.6108 \times e^{\frac{17.27 \times T_a}{T_a + 273.15}}) \times \frac{RH}{100} \tag{A.3.4.2}$$

4.3. Calculate the vapor pressure gradient (VPG, kPa). Idso et al. (1982).

$$VPG = 0.6108 \times e^{\frac{17.27 \times T_a}{T_a + 273.15}} - (0.6108 \times e^{\frac{17.27 \times (T_a + 3.11)}{(T_a + 3.11) + 273.15}}) \times \frac{RH}{100} \tag{A.3.4.3}$$

4.4. Compute dT_{ll} (°C). Idso et al. (1982).

$$dT_{ll} = 3.11 - 1.97 \times VPD \tag{A.3.4.4}$$

4.5. Compute dT_{ul} (°C). Idso et al. (1982).

$$dT_{ul} = 3.11 - 1.97 \times VPG \tag{A.3.4.5}$$

4.6. Compute the CWSI. Idso et al. (1982).

$$CWSI = \frac{dT - dT_{ll}}{dT_{ul} - dT_{ll}} \tag{A.3.4.6}$$

4.7. Calculate the ET_a (mm h^{-1}). Idso et al. (1982).

$$ET_a = (1 - CWSI) \times ET_p \tag{A.3.4.7}$$

where ET_p is the ET_c for no stress conditions.

4.8. Extrapolate the hourly ET_a to the daily ET_a (mm d^{-1}) using the Reference ET Fraction (ET_rF).

$$ET_rF = \frac{ET_{a_i}}{ET_r} \tag{A.3.4.8}$$

Where ET_r is the ASCE-EWRI reference ET.

$$ET_{a\_d} = ET_rF \times ET_{r\_d} \tag{A.3.4.9}$$

3.5. Reflectance-based Crop Coefficients (k_{cbrf}) ET_a Method

The following procedure is a description of the k_{cbrf} model and corresponding ERDAS Imagine Model (k_cbrf).

5.1. Calculate the NDVI.

$$NDVI = \frac{NIR - RED}{NIR + RED} \tag{A.3.5.1}$$

5.2. Calculate the NDVI based k_{cbrf_NDVI}. Range [-1:1]. Neale et al. (1989).

$$k_{cbrf\_NDVI} = 1.181 \times NDVI - 0.026 \tag{A.3.5.2}$$

5.3. Calculate OSAVI: Rondeaux et al. (1996). Range [-1:1].

$$OSAVI = \frac{(1+L)\times(NIR-RED)}{NIR+RED+L} \tag{A.3.5.3}$$

where L=0.16 for corn.

5.4. Calculate Leaf Area Index (LAI): Anderson et al. (2004). Range [0.5≤LAI≤5] "3 LAI_RS".

$$LAI = (4 \times OSAVI - 0.8) \times (1 + 4.73 \times 10^{-6} \times e^{15.64 \times OSAVI}) \tag{A.3.5.4}$$

5.5. Calculate Fraction Vegetation Cover (f_c). Normal et al. (1995). Range [0:1]. "4 f_c".

$$f_c = 1 - e^{-0.5 \times LAI} \tag{A.3.5.5}$$

5.6. Calculate the f_c base k_{cbrf_fc}. Johnson and Trout (2012).

$$k_{cbrf\_fc} = 1.13 \times f_c + 0.14 \tag{A.3.5.6}$$

5.7. Calculate the hourly ET_a (mm h^{-1}).

$$ET_a = [k_{cbrf\_NDVI} \text{ or } k_{cbrf\_fc}] \times ET_{ref} \tag{A.3.5.7}$$

5.8. Extrapolate the hourly ET_a to the daily ET_a (mm d^{-1}) using the Reference ET Fraction (ET_rF).

$$ET_rF = \frac{ET_a}{ET_r} \qquad \text{(A.3.5.8)}$$

Where ET_r is the ASCE-EWRI reference ET.

$$ET_{a\_d} = ET_rF \times ET_{r\_d} \qquad \text{(A.3.5.9)}$$

3.6. Hybrid Soil Water Balance Method.

3.6.1 FAO-56 Soil Water Balance

The FAO-56 SWB approach starts with a given soil profile at field capacity ($\theta_{FC,}$ mm m^{-1}). Field capacity is generally defined as the amount of water held in the soil after excess water has drained away and the rate of downward drainage has decreased. Once the SWB begins, the daily allowable depletion, and root zone SWC are tracked using the following equation [Hoffmann et al., 2007]:

$$D_i = D_{i-1} + ET_a - (P - S_{ro}) - I_n + DP - GW \qquad \text{(A.3.6.1)}$$

Where D_i (mm) is the soil water depletion at the end of day i, D_{i-1} is the soil water depletion at the end of day i-1 (mm), ET_a is the actual crop evapotranspiration (mm), P (mm) is the gross precipitation infiltrated, S_{ro} (mm) is the surface runoff, I_n (mm) is the net irrigation on day i, DP (mm) is the deep percolation on day i, and GW (mm) is the ground water capillary contribution from the water table on day i [Hoffmann et al., 2007].

The ET_a is calculated using the dual basal crop coefficient method:

$$ET_a = (k_{cb} \times k_s + k_e) \times ET_{ref} \qquad \text{(A.3.6.2)}$$

Where the dual K_c is estimated using the mean basal k_{cb}, the stress coefficient (k_s) and the soil evaporation coefficient (k_e) [Neale et al., 2012].

The mean basal crop coefficient can be obtained from published tabulated values in FAO-56. The mid-season k_{cb} values are adjusted for the appropriate climate conditions. The FAO-56 published K_{cb} values are for humid climates and therefore need to be adjusted to be used in arid and semi-arid regions with Eq. (A.3.6.3).

$$k_{cb} = k_{cb\_table} + [0.04 \times (u_2 - 2) - 0.004 \times (RH_{\min} - 45)](\frac{h}{3})^3 \qquad \text{(A.3.6.3)}$$

where k_{cb_table} can be found in Table 17 of FAO-56, u_2 (m s^{-1}) is the mean daily wind speed at 2 m height above grass during mid-season growth stage, RH_{min} (%) is the mean value for minimum relative humidity during mid-season growth stage, and h (m) is the mean value for plant height during mid-season.

The stress coefficient, k_s, according to Allen et al. (1995) is calculated as:

$$k_s = \frac{TAW - D_r}{TAW - RAW} \qquad \text{(A.3.6.4)}$$

where TAW is the total available water (mm), D_r is the root zone depletion (mm), and RAW is the readily available water (mm).

The shallow soil water evaporation coefficient, k_e, is calculated using the following equation:

$$k_e = k_r (k_{c\max} - k_{cb}) \leq f_{ew} \times k_{c\max} \qquad \text{(A.3.6.5)}$$

where, k_r, is the evaporation reduction coefficient, $k_{c\,max}$ is the maximum value of k_c following a wetting event, and f_{ew} is the fraction of soil that receives sunlight, and water during the wetting event [Allen et al., 1995].

$$k_{c\_\max} = \max[1.2 + [0.04 \times (u_2 - 2) - 0.004 \times (RH_{\min} - 45)](\frac{h}{3})^3, k_{cb} + 0.05] \qquad \text{(A.3.6.6)}$$

$$k_r = \begin{cases} 1 \; for \; D_{r\_s} \leq REW \\ \frac{TEW - D_{r\_s}}{TEW - REW} \; for \; D_{r\_s} > REW \end{cases} \tag{A.3.6.7}$$

where D_{r_s} is the depletion of the soil surface layer (mm).

$$f_{ew} = f_w(1 - \frac{2}{3} f_c) \tag{A.3.6.8}$$

where the fraction of the surface that is wetted by irrigation and rain (fw) depends on irrigation.

3.6.2. Remote Sensing Assimilation

The RS derived ET_a and k_{cbr} are assimilated into the FAO 56 SWB using the k_s. In order to update the SWD, the RS derived ET_a is used to calculate the updated stress coefficient, k_s:

$$k_s = \frac{\frac{ET_a}{ET_{ref}} - k_e}{k_{cbrf}} \tag{A.3.6.9}$$

The updated k_s is used to estimate the actual soil water deficit (D_i, mm) by using the linear relationship between the k_s, readily available water (RAW, mm) and total available water (TAW, mm) as shown in Figure A.3.1. If the hybrid model derived k_s=1, θ_i>RAW. If k_s<1, then the D_i is a function of the linear relationship between RAW (K_s=1) and TAW (k_s=0) [Allen et al.,1995]. In the terms of a PA irrigation system, if the D_i<RAW, irrigation is not required. If D_i>RAW, irrigation is required.

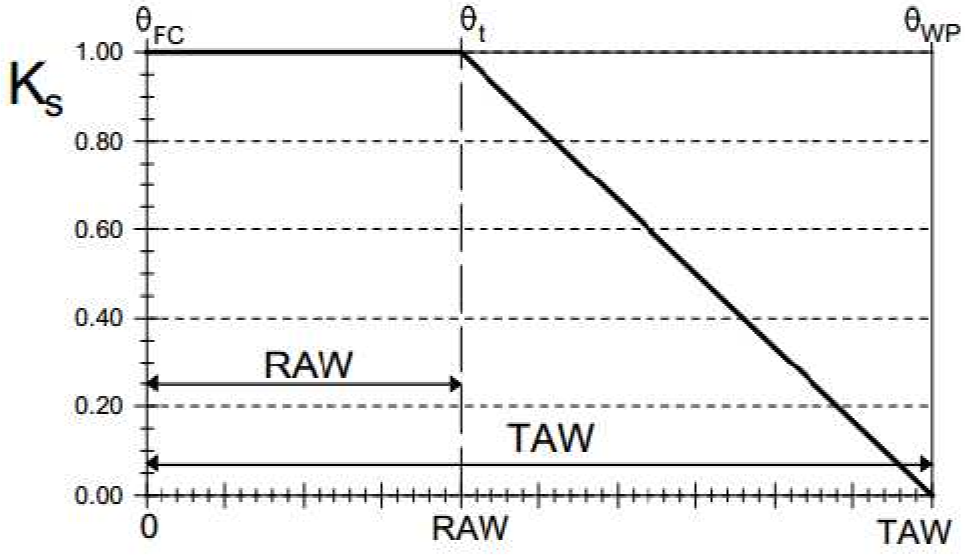

Figure A.3.1. Relationship between k_s, RAW and TAW [Allen et al., 1995]

The soil water content, is updated using the D_i, θ_{FC} and R_z:

$$\theta_i = (\theta_{FC} - D_i) \times R_z \tag{A.3.6.10}$$

The k_{cbrf} is then used to adjust the k_{cb} for use in the SWB between RS overpasses. By adjusting k_{cb} based on the actual crop characteristics, ET_{WB} will more accurately estimate ET_a. Figure A.3.2 depicts the use of the k_{cbrf} when compared to $k_{cb.}$ Under ideal condition, the k_{cbrf} will closely approximate k_{cb}, as with the LIRF fully irrigated crops. Crops that are under non-standard conditions, will generally fall below the k_{cb}.

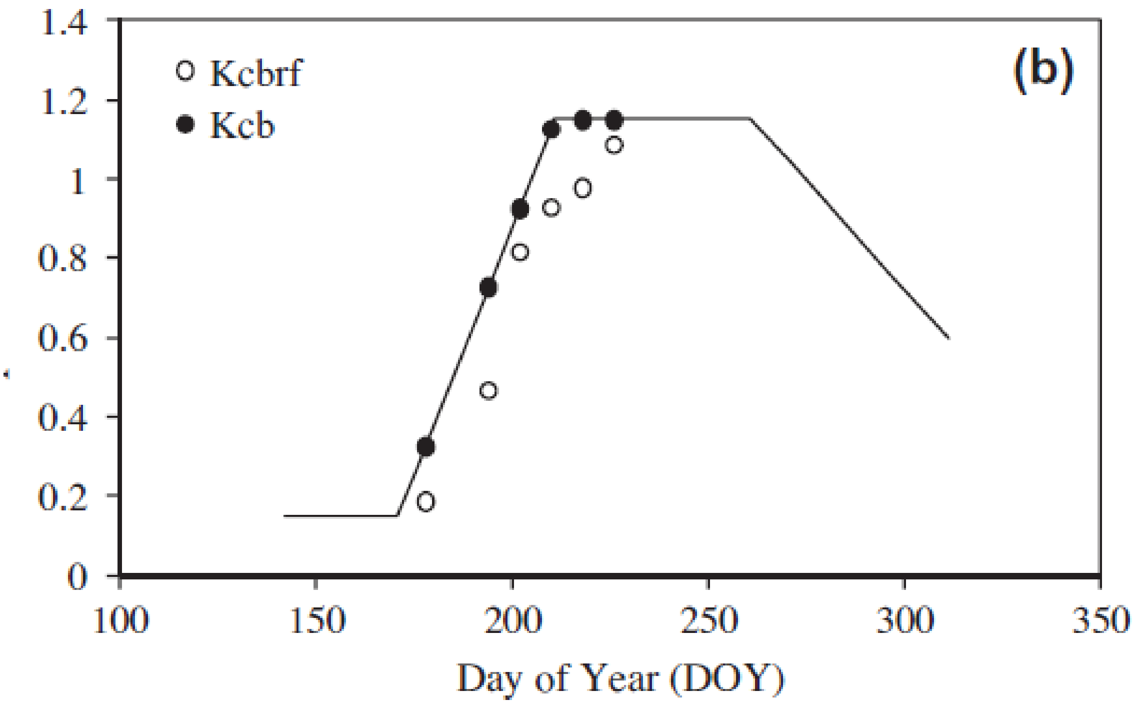

Figure A.3.2. k_{cbrf} vs. k_{cb} over the growing season [Neale et al., 2012]

APPENDIX 4: SUMMER 2015 ARDEC 1070 RS DATA

4.1. 22JUL15

Figure A.4.1. ARDEC 1070 Tempest UAS Multispectral Imagery (121 m AGL) – 22JUL15

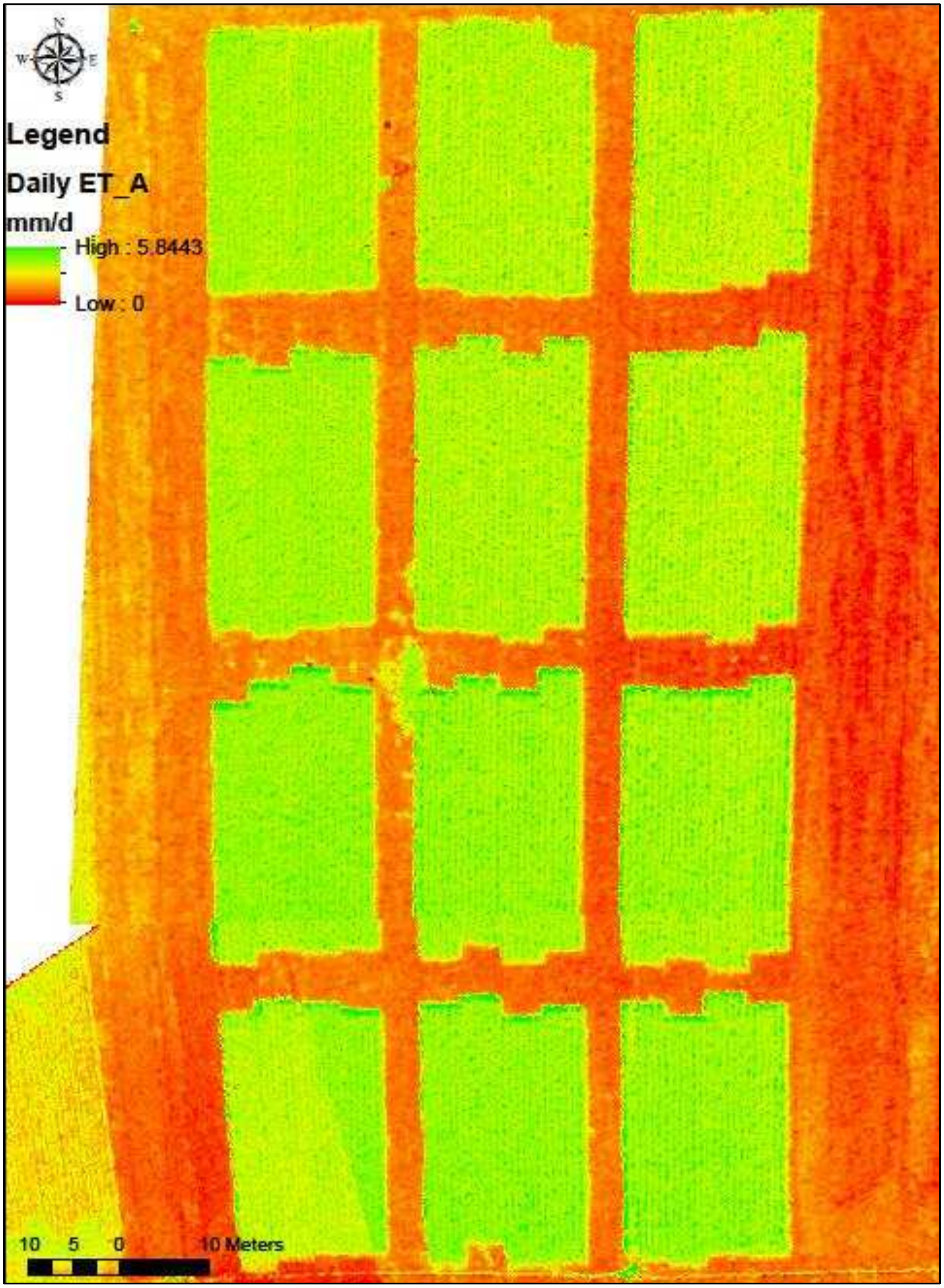

Figure A.4.2. ARDEC 1070 Tempest UAS Multispectral Imagery (121 m AGL) – 22JUL15

4.2. 30JUL15

Figure A.4.3. ARDEC 1070 Tempest UAS Multispectral Imagery (121 m AGL) – 30JUL15

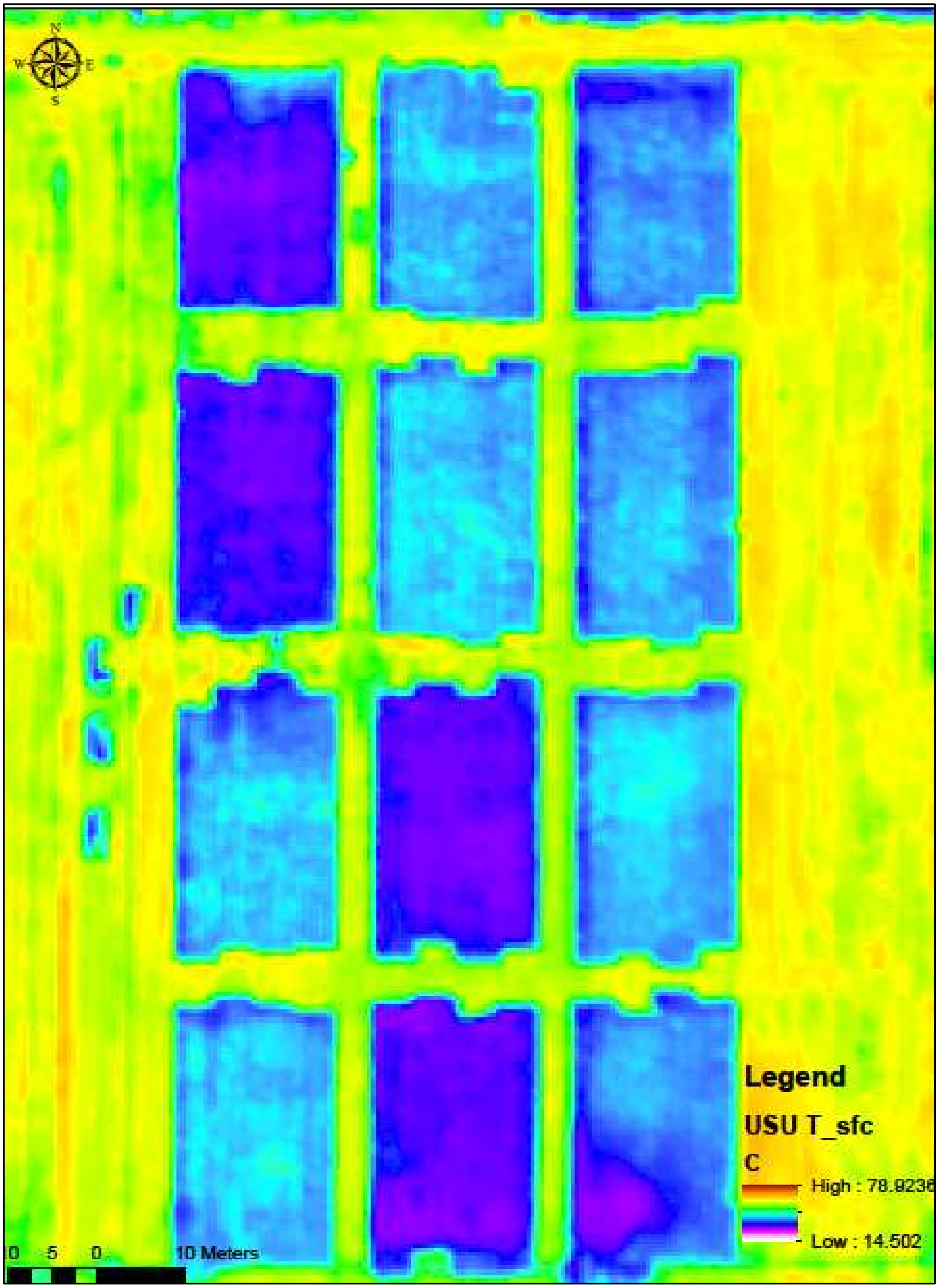

Figure A.4.4. ARDEC 1070 USU Thermal Imagery (121 m AGL) – 30JUL15

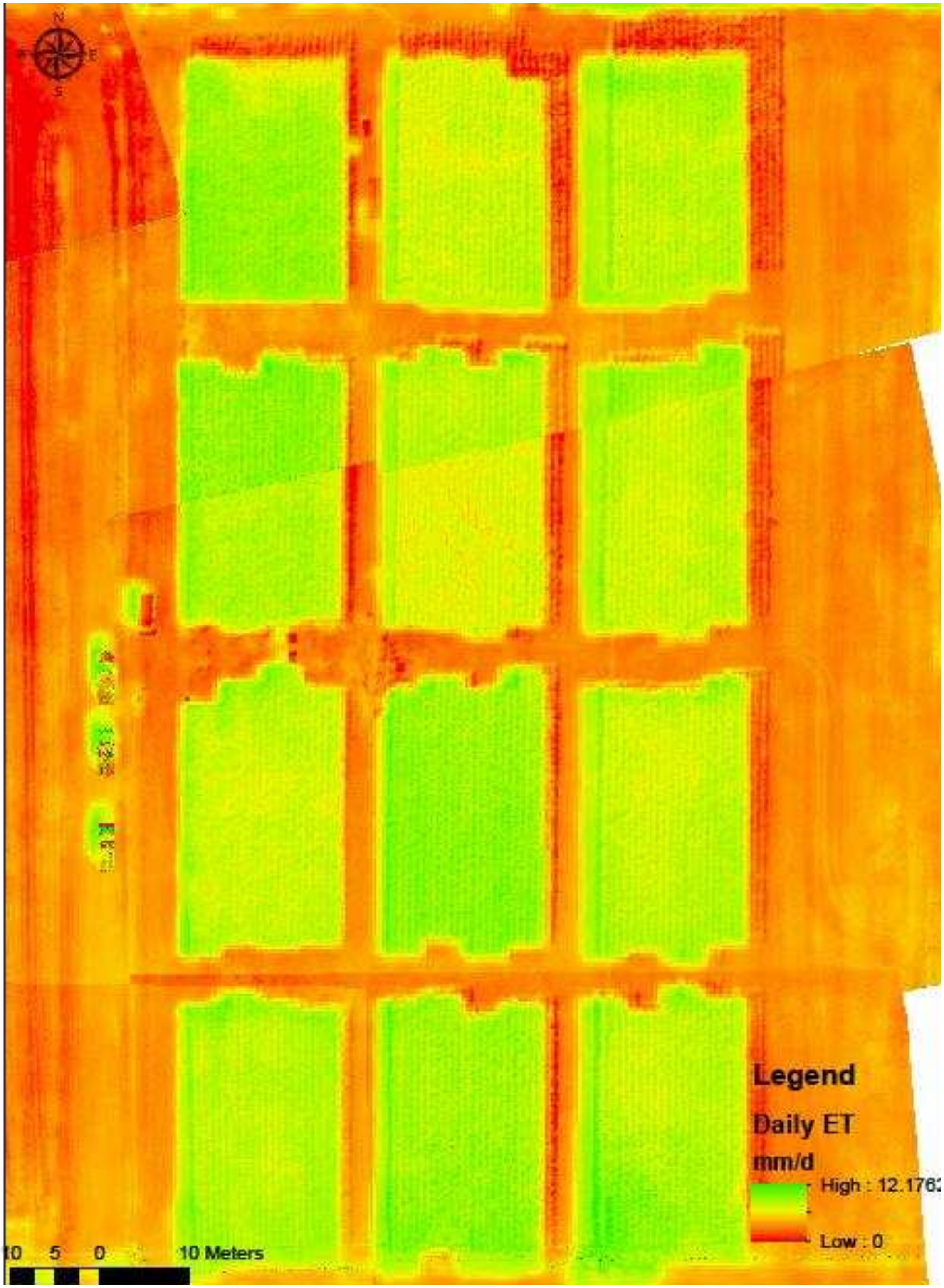

Figure A.4.5. ARDEC 1070 Tempest UAS Daily ET_a (121 m AGL) – 30JUL15

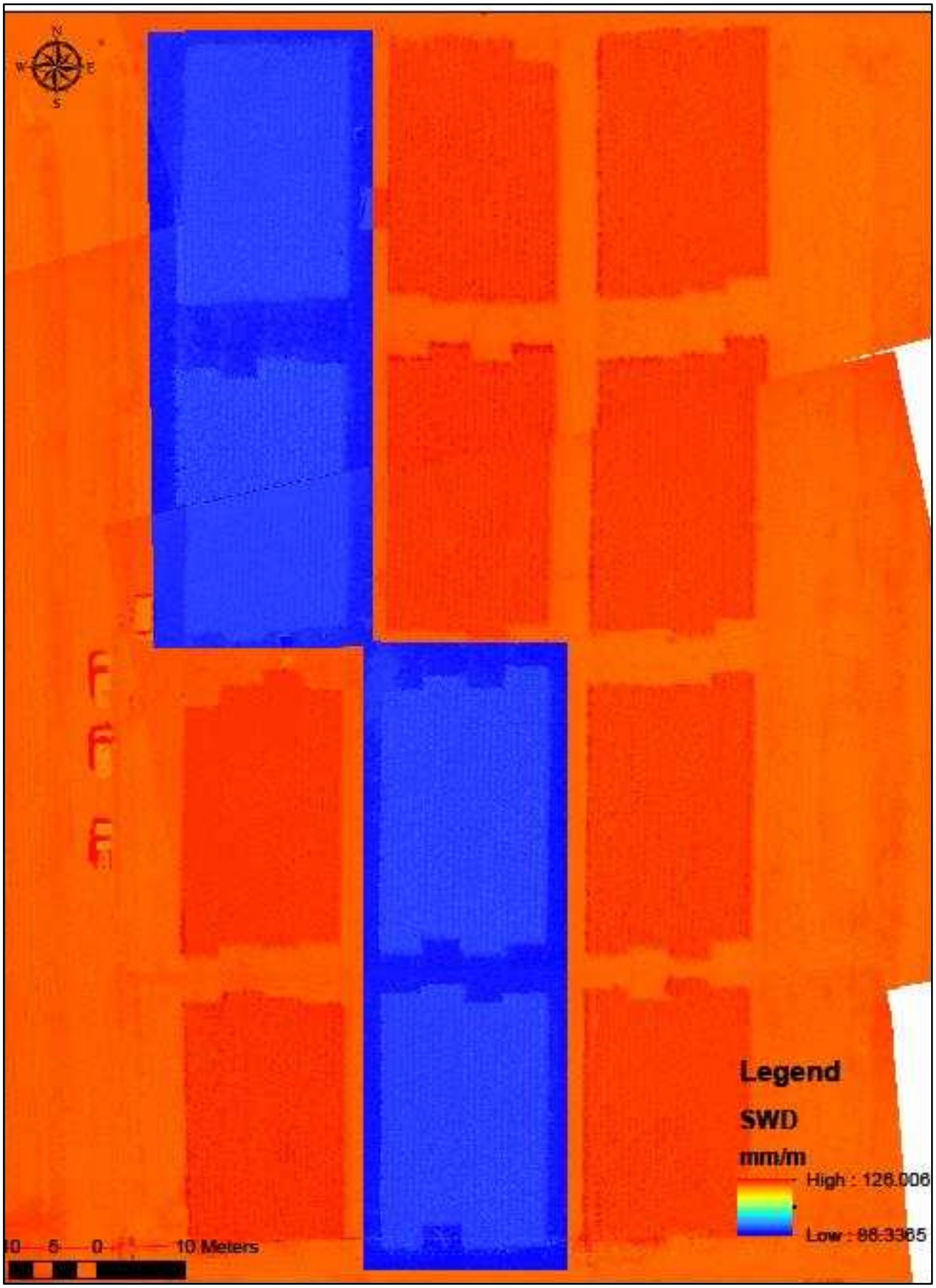

Figure A.4.6. ARDEC 1070 Tempest UAS SWD (121 m AGL) – 30JUL15

4.3. 13AUG15

Figure A.4.7. ARDEC 1070 Tempest UAS Multispectral Imagery (121 m AGL) – 13AUG5

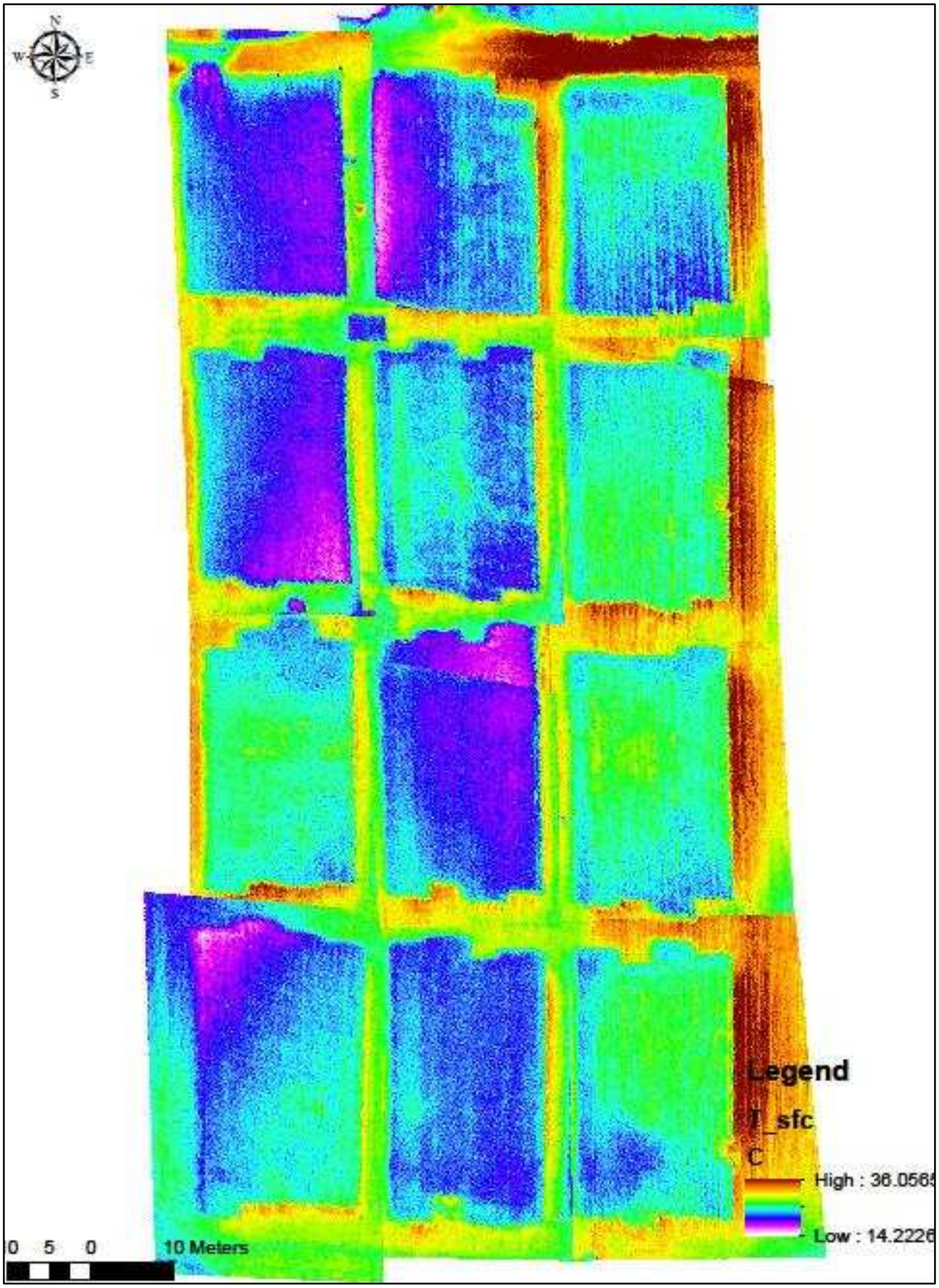

Figure A.4.8. ARDEC 1070 Tempest UAS Thermal Imagery (121 m AGL) – 13AUG15

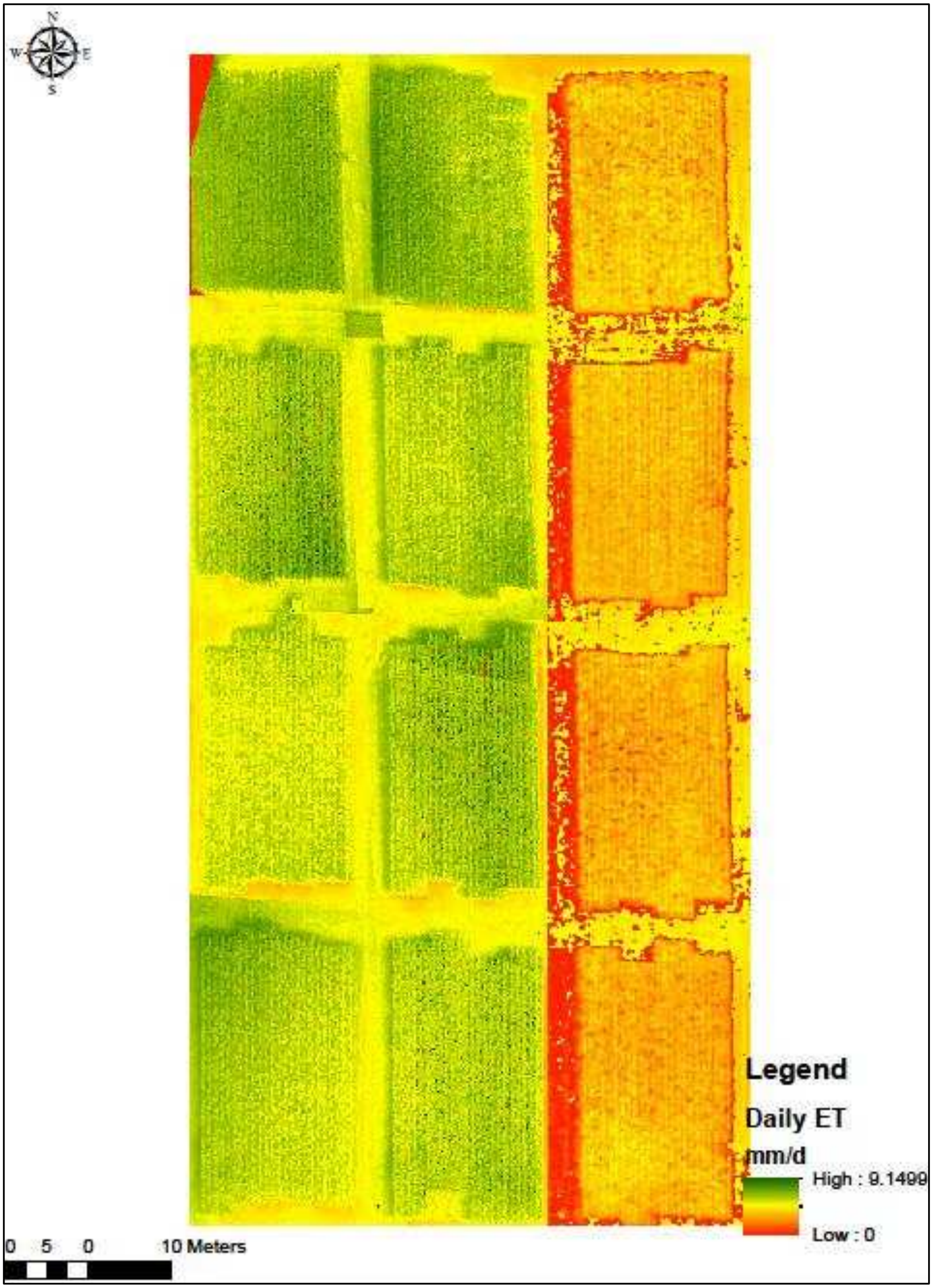

Figure A.4.9. ARDEC 1070 Tempest UAS Daily ET_a (121 m AGL) – 13AUG15

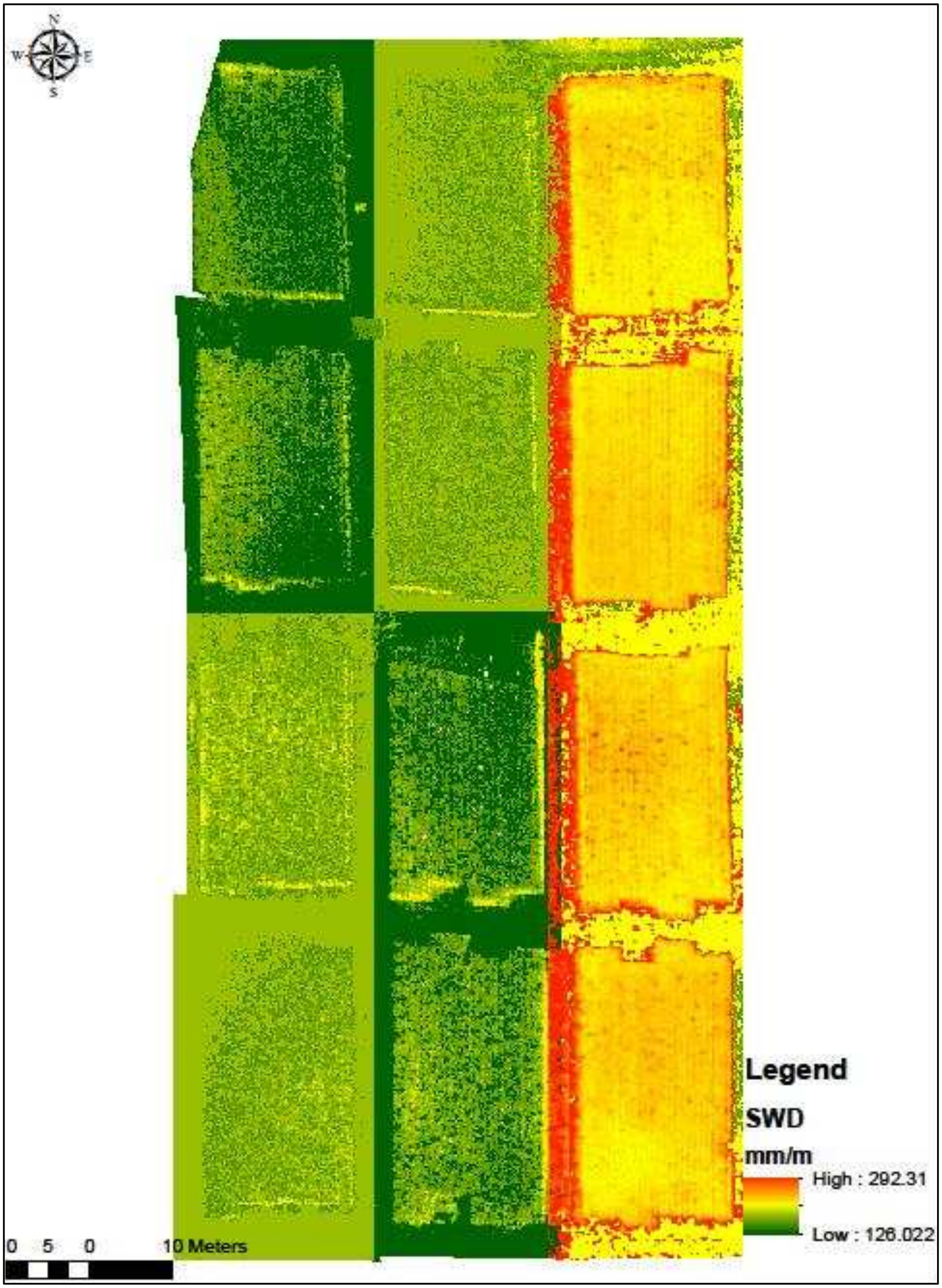

Figure A.4.10. ARDEC 1070 Tempest UAS SWD (121 m AGL) – 13AUG15

4.4. 19AUG15

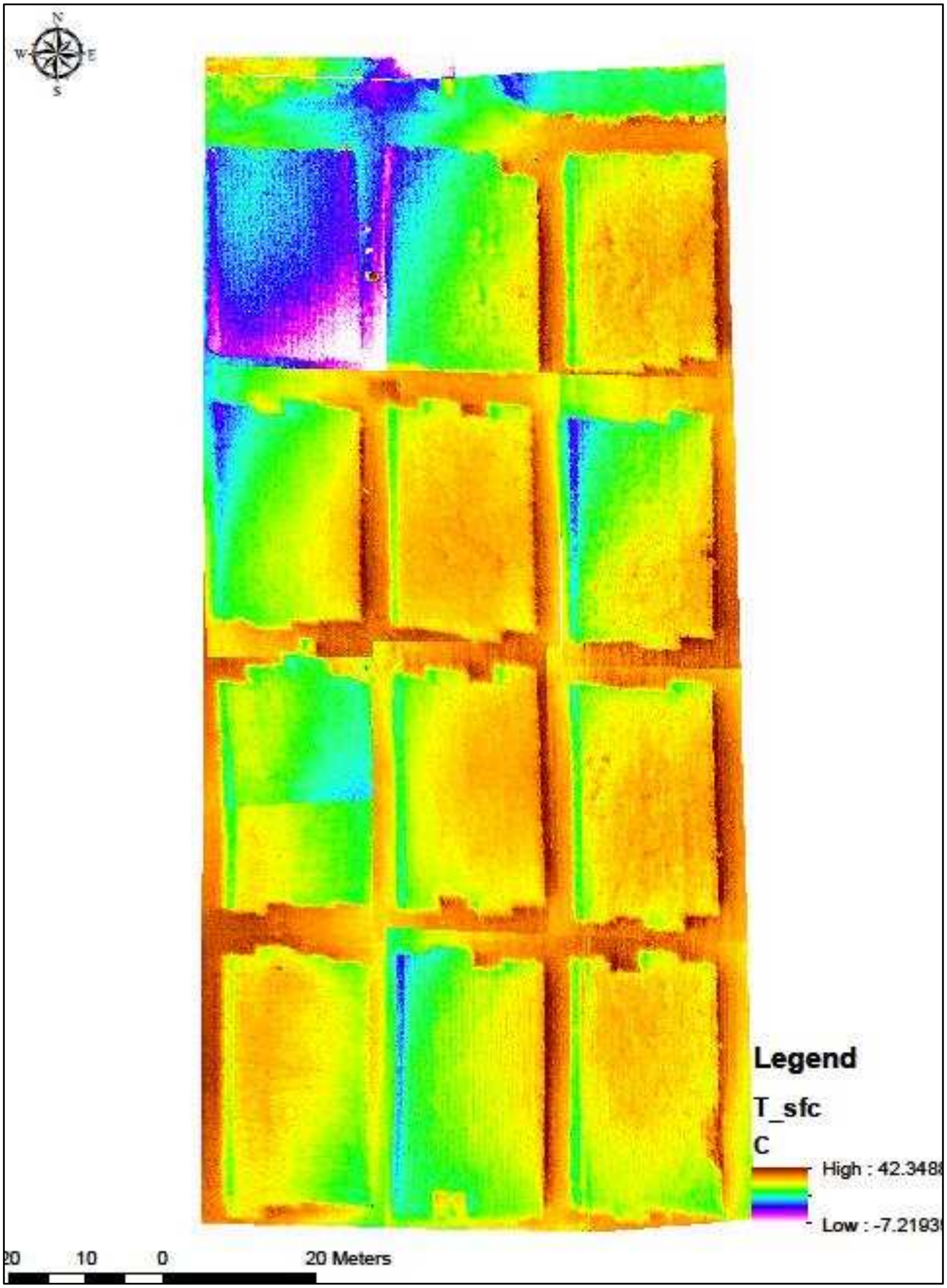

Figure A.4.11. ARDEC 1070 Tempest UAS Thermal Imagery (121 m AGL) – 19AUG15

4.5. 10SEP15

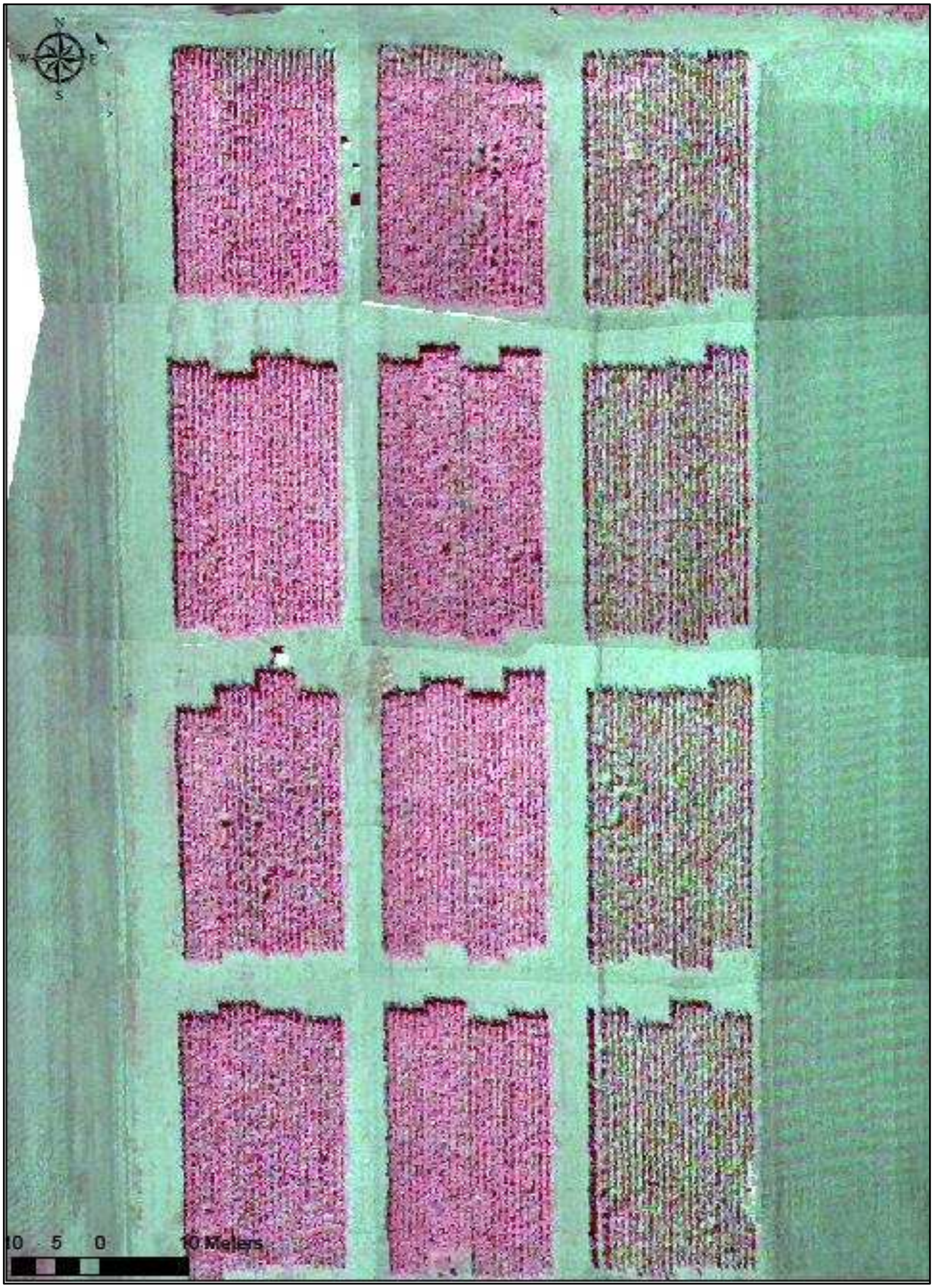

Figure A.4.12. ARDEC 1070 Tempest UAS Multispectral Imagery (121 m AGL) – 10SEP15

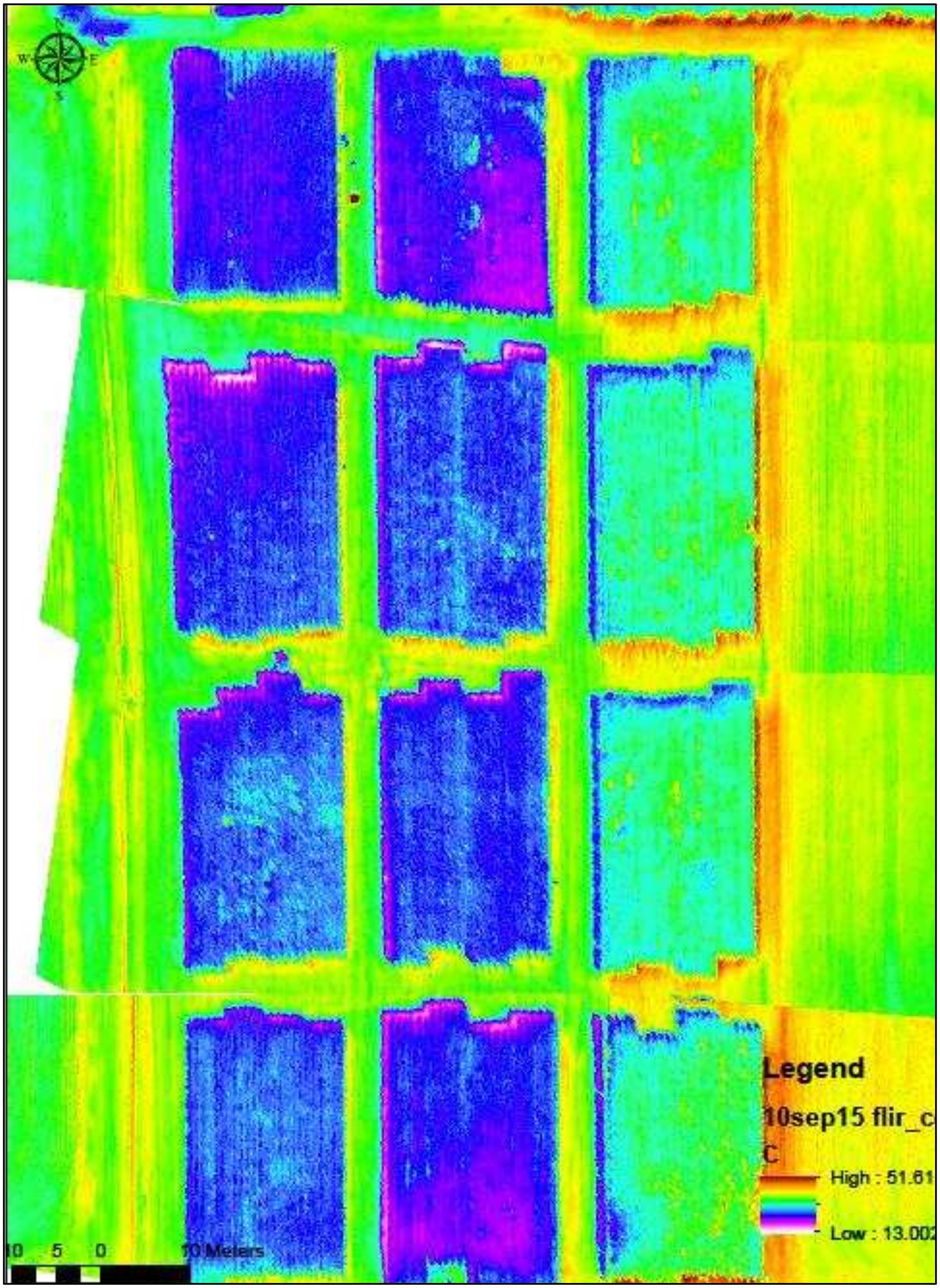

Figure A.4.13. ARDEC 1070 Tempest UAS Thermal Imagery (121 m AGL) – 10SEP15

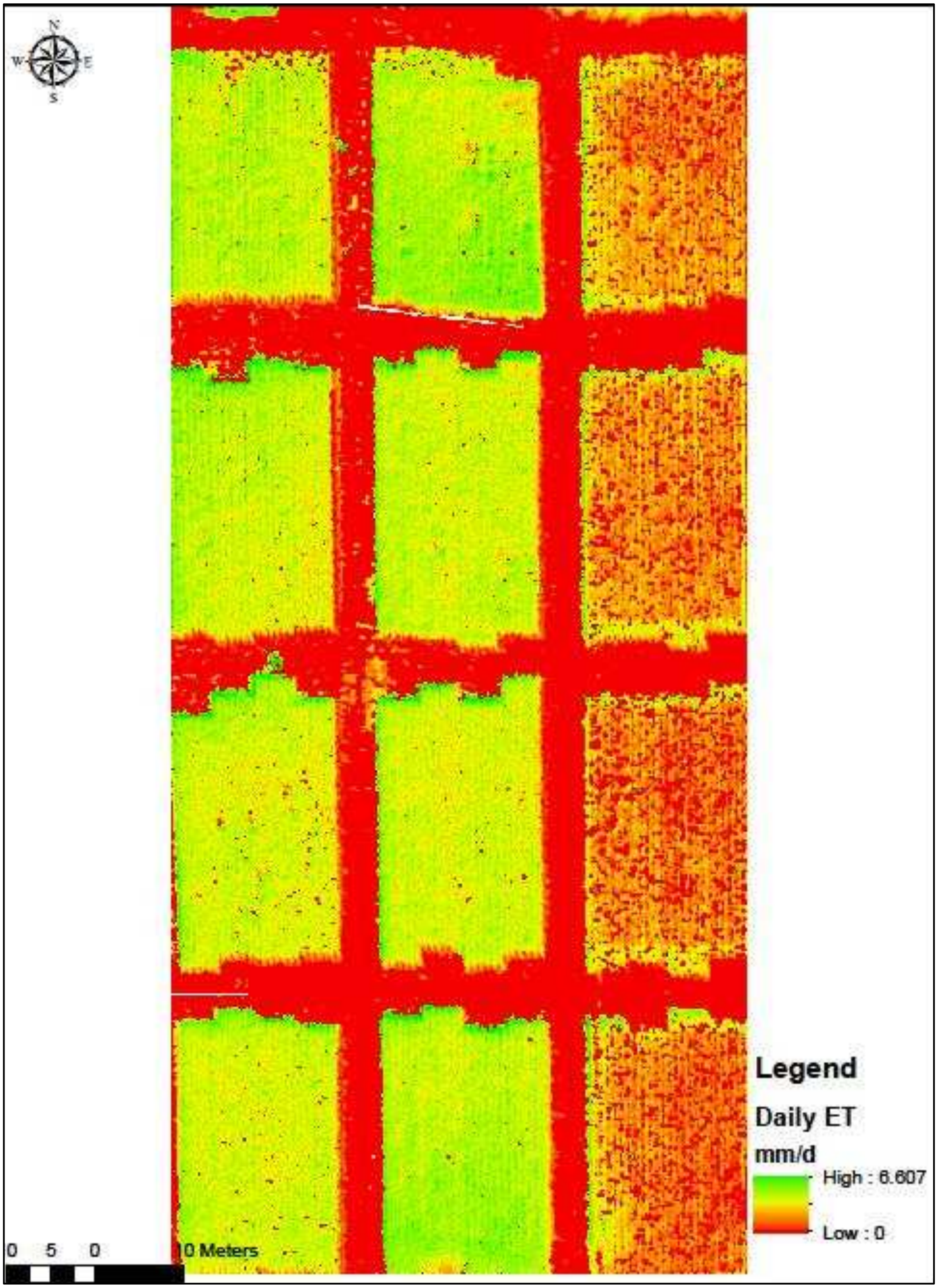

Figure A.4.14. ARDEC 1070 Tempest UAS Daily ET$_a$ (121 m AGL) – 10SEP15

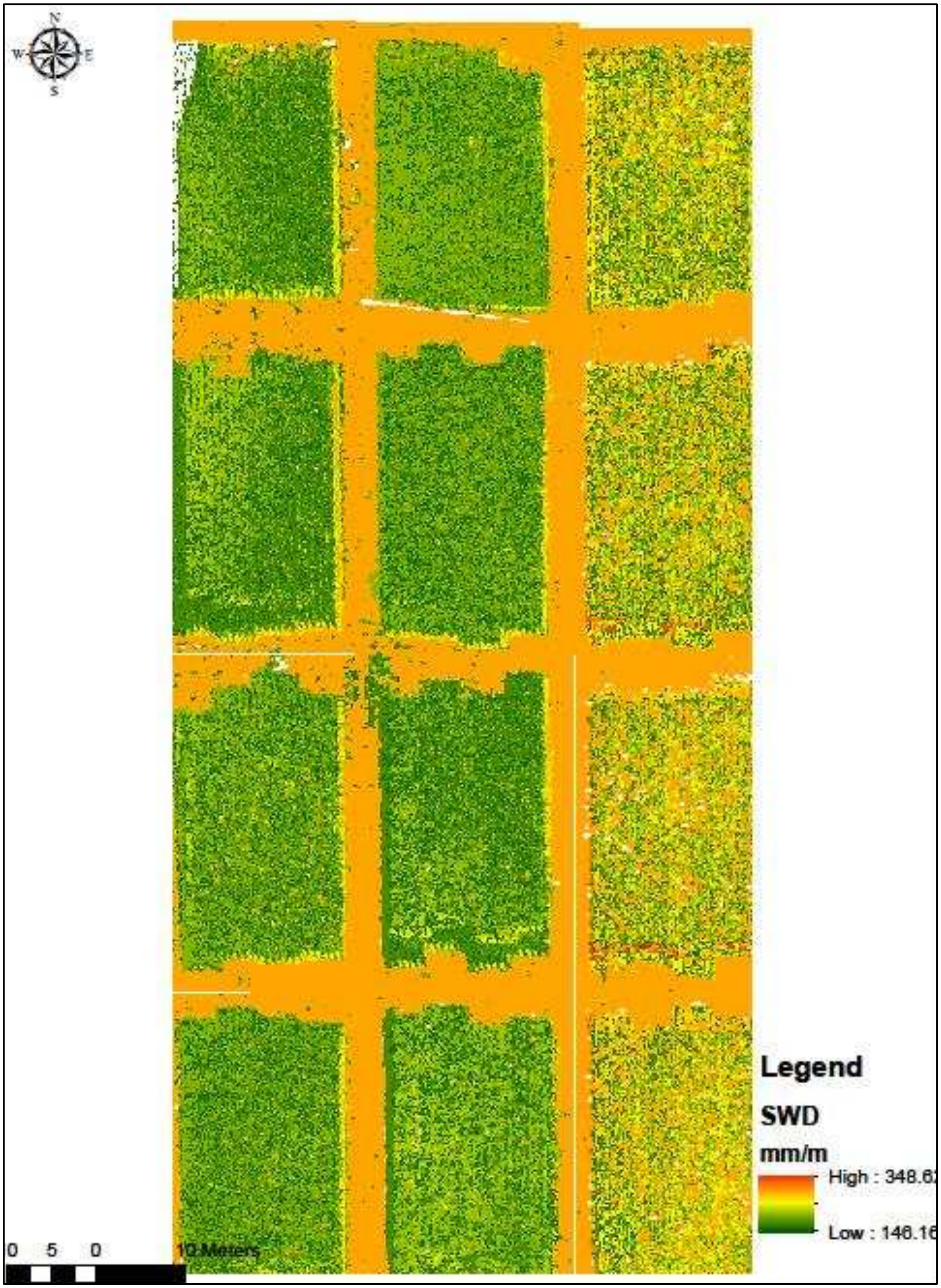

Figure A.4.15. ARDEC 1070 Tempest UAS SWD (121 m AGL) – 10SEP15

4.6. Summary of Results

4.6.1. Raw Data

Table A.4.1. MBE Summary of the 2015 ARDEC 1070 RS Campaign RS vs MSR5 data comparisons.

2015 Tempest UAS Raw Data vs MSR5 Data MBE Results				
Flight Date	**MBE**			
	Thermal (C)	**Green (% Reflection)**	**Red (% Reflection)**	**NIR (% Reflection)**
Season*	**-1.36**	**5.06**	**0.81**	**-1.17**
22-Jul-15		10.09	3.22	-0.88
30-Jul-15		0.08	0.05	0.14
13-Aug-15	-8.02	0.14	0.04	0.19
10-Sep-15	1.20	3.28	-0.55	-1.51
Data linearly corrected due to eqipment malfunction				
Uncorrected data				
No data due to equipment malfunction				

Table A.4.2. RMSE Summary of the 2015 ARDEC 1070 RS Campaign RS vs MSR5 data comparisons.

2015 Tempest UAS Raw Data vs MSR5 Data RMSE Results				
Flight Date	**RMSE**			
	Thermal (C)	**Green (% Reflection)**	**Red (% Reflection)**	**NIR (% Reflection)**
Season*	**5.68**	**7.31**	**3.51**	**5.26**
22-Jul-15		10.76	4.03	6.16
30-Jul-15		1.41	1.55	2.80
13-Aug-15	9.62	1.64	2.06	5.33
10-Sep-15	2.40	6.06	3.74	5.38
Data linearly corrected due to eqipment malfunction				
Uncorrected data				
No data due to equipment malfunction				

Table A.4.3. Student-T Test Summary of the 2015 ARDEC 1070 RS Campaign RS vs MSR5 data comparisons.

2015 Tempest UAS Raw Data vs MSR5 Data RMSE Results				
Flight Date	**T_Test**			
	Thermal	**Green**	**Red**	**NIR**
Season*	**0.12**	**0.00**	**0.05**	**0.06**
22-Jul-15	■	0.10	0.58	0.82
30-Jul-15	■	0.81	0.91	0.93
13-Aug-15	0.00	0.79	0.95	0.93
10-Sep-15	0.45	0.29	0.98	0.71
Data linearly corrected due to eqipment malfunction				
Uncorrected data				
No data due to equipment malfunction				

Table A.4.4. Linear Regression Summary of the 2015 ARDEC 1070 RS Campaign RS vs MSR5 data comparisons.

2015 Tempest UAS Raw Data Linear Regression Coefficients				
	Thermal	Green	Red	NIR
a	0.74	0.92	0.89	0.75
b	7.45	5.62	1.97	8.49
R^2	0.67	0.91	0.97	0.91

4.6.2. ET_d

Table A.4.5. Summary of the statistics from the daily ET_a derived from the 2015 Tempest UAS RS campaign.

Method	**Statistic**	**Season**	**22-Jul-15**	**30-Jul-15**	**13-Aug-15**	**10-Sep-15**
TSEB	MBE (mm/d)	**0.29**		0.23	0.06	0.58
	RMSE (mm/d)	**0.89**		1.10	0.54	0.93
	2*P[T<=t]	**0.00**		0.15	0.47	0.00
SAT	MBE (mm/d)	**0.49**		-0.89	0.03	0.96
	RMSE (mm/d)	**1.21**		1.56	0.95	1.47
	2*P[T<=t]	**0.00**		0.00	0.83	0.00
NDVI	MBE (mm/d)	**0.79**	0.14	1.27	0.49	1.28
	RMSE (mm/d)	**1.43**	0.91	1.83	1.00	1.74
	2*P[T<=t]	**0.00**	0.29	0.00	0.00	0.00
FAO-56 SWB Rz=1 m	MBE (mm/d)	**-0.94**	-1.17	-0.96	-1.27	-0.36
	RMSE (mm/d)	**1.22**	1.46	1.23	1.36	0.82
	2*P[T<=t]	**0.00**	0.39	0.00	0.14	0.83
FAO-56 SWB Rz=1.5 m	MBE (mm/d)	**1.44**	-0.73	0.52	1.97	1.20
	RMSE (mm/d)	**1.64**	1.11	0.86	2.17	1.49
	2*P[T<=t]	**0.00**	0.39	0.00	0.00	0.00
CWSI	MBE (mm/d)	**1.58**			-0.55	0.01
	RMSE (mm/d)	**1.86**			0.74	0.75
	2*P[T<=t]	**0.00**			0.01	0.00
FC	MBE (mm/d)	**1.88**	1.08	2.65	1.25	1.92
	RMSE (mm/d)	**2.30**	1.44	2.96	1.85	2.23
	2*P[T<=t]	**0.00**	0.00	0.00	0.00	0.00

Table A.4.6. Linear Regression Summary of the statistics from the daily ET_a derived from the 2015 Tempest UAS RS campaign.

2015 Tempest UAS ET_d Linear Regression Coefficients							
	TSEB	SAT	NDVI	FAO-56 (R_z=1 m)	FAO-56 (R_z=1.5m)	CWSI	F_c
a	0.60	0.10	0.29	0.61	0.67	0.88	0.38
b	1.55	2.85	3.16	0.36	0.92	1.90	3.78
R^2	0.71	0.12	0.29	0.77	0.63	0.62	0.27

Table A.4.7. Mean daily ET_a derived from the 2015 Tempest UAS RS campaign - Full.

2015 Mean Tempest UAS Mean ET_d (mm d^{-1}) Full Treatment

	TSEB	SAT	NDVI	FAO-56 (R_z=1 m)	FAO-56 (R_z=1.5m)	CWSI	F_c	NP
22-JUL	N/A	N/A	4.15	3.67	3.75	N/A	5.10	4.40
30-JUL	4.72	3.26	5.28	4.06	5.81	N/A	6.69	5.68
13-AUG	3.74	3.16	3.66	2.51	3.38	5.04	4.47	3.84
10-SEP	3.87	3.78	4.02	2.85	3.28	5.05	4.75	3.70

Table A.4.8. Mean daily ET_a derived from the 2015 Tempest UAS RS campaign - Limited.

2015 Mean Tempest UAS Mean ET_d (mm d^{-1}) Limited Treatment

	TSEB	SAT	NDVI	FAO-56 (R_z=1 m)	FAO-56 (R_z=1.5m)	CWSI	F_c	NP
22-JUL	N/A	N/A	3.95	2.25	2.78	N/A	4.82	3.82
30-JUL	3.90	3.26	5.26	2.58	3.83	N/A	6.65	3.19
13-AUG	3.58	3.07	3.57	2.11	2.62	5.07	4.32	3.41
10-SEP	3.74	3.79	4.03	2.78	2.78	4.60	4.73	3.21

Table A.4.9. Mean daily ET_a derived from the 2015 Tempest UAS RS campaign - Drought.

2015 Mean Tempest UAS Mean ET_d (mm d^{-1}) Drought Treatment

	TSEB	SAT	NDVI	FAO-56 (R_z=1 m)	FAO-56 (R_z=1.5m)	CWSI	F_c	NP
22-JUL	N/A	N/A	3.86	2.12	2.83	N/A	4.86	3.31
30-JUL	4.05	3.01	5.20	2.45	3.91	N/A	6.53	3.12
13-AUG	2.06	3.09	3.47	0.77	1.58	5.02	4.18	1.95
10-SEP	1.18	3.74	2.84	0.33	0.77	0.97	3.35	0.12

Table A.4.10. 22JUL15 ARDEC 1070 RS, FAO-56 SWB and NP derived daily ET_a.

	22-Jul-15				
	ET_d (mm/d)				
Plot	**NDVI**	**Fc**	**SWB 1 m**	**SWB 1.5 m**	**NP**
101	4.12	4.956	3.67	3.75	**1.99**
4	3.96	4.73	3.67	3.75	**3.81**
8	4.11	4.95	3.67	3.75	**3.77**
104	4.00	4.87	3.67	3.75	**4.39**
105	3.96	4.68	2.25	2.78	**4.36**
106	3.95	4.715	2.25	2.78	**3.82**
12	3.96	4.68	2.25	2.78	**3.61**
16	3.87	4.6	2.25	2.78	**2.36**
109	3.88	4.6	2.12	2.83	**4.77**
20	3.82	4.54	2.12	2.83	**3.29**
24	3.68	4.3	2.12	2.83	**3.17**
112	3.73	4.49	2.12	2.83	**4.56**
28	4.15	5.04	3.67	3.75	**4.1**
202	4.23	4.99	3.67	3.75	**3.62**
204	4.11	4.92	3.67	3.75	**5.08**
36	4.06	4.88	2.25	2.78	**2.34**
206	4.01	4.79	2.25	2.78	**3.96**
207	3.99	4.78	2.25	2.78	**3.67**
40	4.08	4.72	2.25	2.78	**4.39**
210	3.95	4.7	2.12	2.83	**3.68**
48	3.94	4.65	2.12	2.83	**3.33**
212	3.86	4.6	2.12	2.83	**3.1**
301	4.21	5.27	2.25	2.78	**3.82**
52	4.31	5.1	2.25	2.78	**3.98**
56	4.37	5.24	2.25	2.78	**3.82**
304	4.26	5.31	2.25	2.78	**3.98**
60	4.28	5.26	3.67	3.75	**3.93**
306	4.24	5.18	3.67	3.75	**5.03**
64	4.21	5.2	3.67	3.75	**6.26**
308	3.92	4.99	3.67	3.75	**5.13**
68	4.18	5.04	2.12	2.83	**3.33**
310	4.22	5.09	2.12	2.83	**3.43**
72	4.05	4.84	2.12	2.83	**3.78**
312	4.08	5.03	2.12	2.83	**2.95**
76	2.88	4.36	2.25	2.78	**4.42**
80	3.42	4.38	2.25	2.78	**4.56**
403	3.73	4.54	2.25	2.78	**4.58**
404	4.10	5.07	2.25	2.78	**3.37**
405	4.31	5.35	3.67	3.75	**5.76**
406	4.13	5.08	3.67	3.75	**4**
84	4.41	5.55	3.67	3.75	**5.39**
88	4.07	5.49	3.67	3.75	**3.77**
409	4.23	5.25	2.12	2.83	**2.74**
410	4.22	5.26	2.12	2.83	**3.04**
92	3.16	5.36	2.12	2.83	**2.69**
96	2.89	5.18	2.12	2.83	**1.8**
Full	**4.15**	**5.10**	**3.67**	**3.75**	**4.40**
Limited	**3.95**	**4.82**	**2.25**	**2.78**	**3.82**
Drought	**3.86**	**4.86**	**2.12**	**2.83**	**3.31**
MBE	0.14	1.08	-1.17	-0.73	
RMSE	0.91	1.44	1.46	1.11	
T-Test	0.29	0.00	0.00	0.00	

Table A.4.11. 30JUL15 ARDEC 1070 RS, FAO-56 SWB and NP derived daily ET$_a$

30-Jul-15						
ET_d (mm/d)						
TSEB*	**SAT**	**NDVI***	**Fc***	**SWB 1 m**	**SWB 1.5 m**	**NP**
4.61	3.48	5.36	6.88	4.06	5.81	**5.84**
4.79	2.27	5.37	6.9	4.06	5.81	**5.41**
4.85	3.74	5.39	6.93	4.06	5.81	**5.41**
4.29	3.94	5.27	6.71	4.06	5.81	**5.28**
3.79	3.24	5.23	6.58	2.58	3.83	**3.27**
3.74	2.87	5.17	6.48	2.58	3.83	**2.72**
4.1	3.01	5.26	6.6	2.58	3.83	**2.99**
3.9	3.49	5.2	6.5	2.58	3.83	**4.13**
4.23	2.89	5.14	6.43	2.45	3.91	**3.07**
4.1	3.04	5.2	6.48	2.45	3.91	**3.32**
4.12	3.02	5.19	6.55	2.45	3.91	**2.87**
4.07	2.93	5.13	6.44	2.45	3.91	**2.24**
4.5	3.54	5.33	6.88	4.06	5.81	**4.74**
4.48	3.24	5.3	6.72	4.06	5.81	**4.73**
4.28	3.21	5.3	6.75	4.06	5.81	**4.49**
3.53	2.79	5.15	6.45	2.58	3.83	**3.09**
3.67	2.88	5.3	6.72	2.58	3.83	**3.07**
3.75	2.88	5.27	6.66	2.58	3.83	**3.15**
3.39	2.65	5.19	6.53	2.58	3.83	**2.78**
3.86	2.77	5.14	6.73	2.45	3.91	**3.29**
4.09	3.02	5.29	6.53	2.45	3.91	**3.37**
3.04	2.45	5.27	6.71	2.45	3.91	**4.24**
4.04	3.01	5.29	6.79	2.58	3.83	**3.1**
4.01	3.04	5.32	6.84	2.58	3.83	**3.08**
3.98	3.01	5.27	6.74	2.58	3.83	**3.1**
3.89	2.94	5.28	6.58	2.58	3.83	**3.55**
5.01	3.5	5.38	6.62	4.06	5.81	**6.36**
4.79	3.15	5.3	6.68	4.06	5.81	**5.82**
5.06	3.5	5.36	6.79	4.06	5.81	**5.88**
5.58	2.28	5.28	6.63	4.06	5.81	**6.07**
4	3.15	5.25	6.62	2.45	3.91	**3.37**
3.84	3.26	5.21	6.56	2.45	3.91	**2.84**
4.29	3.12	5.28	6.7	2.45	3.91	**2.71**
3.92	2.89	5.18	6.35	2.45	3.91	**3.96**
4.32	3.29	5.45	6.9	2.58	3.83	**2.29**
4.17	3.15	5.27	6.67	2.58	3.83	**2.86**
4.22	3.08	5.32	6.74	2.58	3.83	**3.49**
3.96	2.89	5.26	6.62	2.58	3.83	**4.42**
4.65	3.29	5.18	6.53	4.06	5.81	**6.37**
4.61	3.26	5.11	6.43	4.06	5.81	**7.21**
5.1	3.5	5.2	6.54	4.06	5.81	**6.24**
4.16	3	5.14	6.42	4.06	5.81	**5.41**
4.66	3.29	5.19	6.48	2.45	3.91	**4.27**
4.21	3.1	5.22	6.56	2.45	3.91	**2.71**
4.48	3.25	5.11	6.41	2.45	3.91	**2.6**
3.78	2.95	5.15	6.46	2.45	3.91	**1.92**
4.72	**3.26**	**5.28**	**6.69**	**4.06**	**5.81**	**5.68**
3.90	**3.01**	**5.26**	**6.65**	**2.58**	**3.83**	**3.19**
4.05	**3.01**	**5.20**	**6.53**	**2.45**	**3.91**	**3.12**
0.23	-0.89	1.27	2.65	-0.96	0.52	
1.10	1.56	1.83	2.96	1.23	0.86	
0.15	0.00	0.00	0.00	0.00	0.03	

Table A.4.12. 13AUG15 ARDEC 1070 RS, FAO-56 SWB and NP derived daily ET$_a$

	13-Aug-15							
	ET_d (mm/d)							
Plot	TSEB*	SAT*	CWSI*	NDVI*	Fc*	SWB 1 m	SWB 1.5 m	NP
101	3.86	3.32	5.07	3.86	4.82	2.51	3.38	3.86
4	3.96	3.37	5.08	3.88	4.86	2.51	3.38	3.63
8	4.17	3.43	5.08	3.92	4.93	2.51	3.38	3.9
104	4.02	3.31	5.05	3.77	4.53	2.51	3.38	4.04
105	4.16	3.38	5.08	3.61	4.55	2.11	2.62	2.88
106	3.89	2.29	5.08	3.63	4.52	2.11	2.62	4.31
12	3.8	3.27	5.08	3.69	4.17	2.11	2.62	3.68
16	3.74	3.25	5.08	3.67	4.48	2.11	2.62	1.74
109	2.07	3.1	5.04	3.52	3.96	0.77	1.58	1.56
20	2.3	3.25	5.08	3.59	4.52	0.77	1.58	1.95
24	2.32	3.27	5.08	3.45	4.41	0.77	1.58	2.54
112	1.95	3.06	4.875	3.44	4	0.77	1.58	2.06
28	3.37	2.94	4.53	3.15	4.36	2.51	3.38	3.84
202	3.6	3.06	5.07	3.7	4.5	2.51	3.38	3.84
204	3.96	3.2	5.08	3.67	4.24	2.51	3.38	3.35
36	3.57	3.11	5.08	3.3	4.5	2.11	2.62	2.02
206	3.48	3.08	5.08	3.55	4.29	2.11	2.62	3.74
207	3.62	3.13	5.08	3.52	4.24	2.11	2.62	4.07
40	3.98	3.31	5.08	3.59	4.3	2.11	2.62	4.11
210	2.06	3.02	4.98	3.58	4.31	0.77	1.58	1.46
48	2.08	3.05	5.02	3.56	4.24	0.77	1.58	2.08
212	1.94	2.94	4.99	3.48	4.15	0.77	1.58	1.81
301	3.12	2.96	4.91	3.5	4.2	2.11	2.62	3.75
52	3.37	3.08	5.08	3.59	4.3	2.11	2.62	4.05
56	3.4	3.07	5.08	3.55	4.32	2.11	2.62	3.75
304	3.31	3	5.07	3.55	4.28	2.11	2.62	3.33
60	3.49	3.07	5.08	3.54	4.31	2.51	3.38	3.69
306	3.73	3.12	5.08	3.64	4.42	2.51	3.38	3.66
64	3.77	3.17	5.08	3.7	4.23	2.51	3.38	4.27
308	3.81	3.12	5.08	3.6	4.36	2.51	3.38	4.07
68	1.76	3.11	5.08	3.38	4.13	0.77	1.58	2.08
310	1.86	3.02	4.94	3.39	4.03	0.77	1.58	1.5
72	2.08	3.16	5.08	3.48	4.15	0.77	1.58	2
312	2.17	3.06	4.99	3.45	4.1	0.77	1.58	1.93
76	3.62	3.14	5.08	3.63	4.4	2.11	2.62	2.78
80	3.44	3.08	5.08	3.62	4.04	2.11	2.62	3.31
403	3.42	3.02	5.08	3.53	4.24	2.11	2.62	3.6
404	3.31	2.96	5.08	3.52	4.23	2.11	2.62	3.42
405	3.41	3	5.08	3.54	4.26	2.51	3.38	4.18
406	3.52	3.04	5.08	3.61	4.36	2.51	3.38	3.64
84	3.75	3.16	5.08	3.73	4.45	2.51	3.38	3.76
88	3.62	3.08	5.08	3.63	4.39	2.51	3.38	3.9
409	2.12	3.05	5.08	3.19	3.78	0.77	1.58	2.1
410	2.06	3.02	5	3.55	4.28	0.77	1.58	2.05
92	2.04	3.07	5.08	3.53	4.28	0.77	1.58	1.9
96	2.04	3.13	5.05	3.52	4.39	0.77	1.58	2.28
Full	3.74	3.16	5.04	3.66	4.47	2.51	3.38	3.84
Limited	3.58	3.07	5.07	3.57	4.32	2.11	2.62	3.41
Drought	2.06	3.09	5.02	3.47	4.18	0.77	1.58	1.95
MBE	0.06	0.03	1.97	0.49	1.25	-1.27	-0.55	
RMSE	0.54	0.95	2.17	1.00	1.85	1.36	0.74	
T-Test	0.47	0.83	0.00	0.00	0.00	0.00	0.00	

Table A.4.13. 10SEP1515 ARDEC 1070 RS, FAO-56 SWB and NP derived daily ET$_a$

	10-Sep-15							
	ET_d (mm/d)							
Plot	**TSEB**	**SAT***	**CWSI**	**NDVI**	**Fc**	**SWB 1 m**	**SWB 1.5 m**	**NP**
101	3.93	3.85	5.63	4.02	4.75	2.85	3.28	**3.89**
4	3.73	3.95	4.77	4.17	4.92	2.85	3.28	**3.7**
8	3.84	4.24	5.26	4.27	5.05	2.85	3.28	**4.27**
104	3.49	3.72	4.85	3.91	4.6	2.85	3.28	**3.28**
105	4.06	3.9	5.62	4.02	4.73	2.78	3.03	**3.3**
106	3.91	3.77	5.03	3.94	4.64	2.78	3.03	**1.77**
12	4.64	4.11	6.41	4.17	4.92	2.78	3.03	**3.61**
16	4.64	4.12	6.53	4.21	4.89	2.78	3.03	**4.34**
109	1.91	2.61	1.78	3	3.44	0.33	0.77	**0**
20	1.9	2.61	0.52	3.07	3.52	0.33	0.77	**0**
24	1.52	2.55	0.64	3.07	4.92	0.33	0.77	**0**
112	1.42	2.17	0.64	2.72	3.27	0.33	0.77	**0.32**
28	3.57	3.99	4.97	4.24	5.03	2.85	3.28	**3.05**
202	4.27	3.68	4.16	4.09	4.85	2.85	3.28	**4.95**
204	3.91	3.74	4.58	3.99	4.71	2.85	3.28	**4.12**
36	3.92	3.94	4.41	4.27	5.07	2.78	3.03	**2.68**
206	3.5	3.67	5.33	4.06	4.65	2.78	3.03	**3.62**
207	3.64	3.77	4.16	4.09	4.7	2.78	3.03	**3.12**
40	3.48	4.18	4.58	4.12	4.89	2.78	3.03	**3.54**
210	1.2	2.38	0.83	2.88	3.29	0.33	0.77	**0.31**
48	0.8	2.52	0.86	2.9	3.29	0.33	0.77	**0.05**
212	1.17	2.17	0.899	2.76	3.1	0.33	0.77	**0**
301	3.53	3.51	4.68	3.79	4.44	2.78	3.03	**3.7**
52	3.54	3.68	3.79	4	4.71	2.78	3.03	**2.91**
56	3.35	3.74	3.49	4.04	4.78	2.78	3.03	**3.7**
304	3.41	3.48	3.58	3.92	4.62	2.78	3.03	**4.33**
60	3.76	3.81	4.55	4.08	4.815	2.85	3.28	**3.29**
306	3.35	3.47	4.26	3.81	4.49	2.85	3.28	**2.89**
64	3.96	3.63	4.81	3.89	4.59	2.85	3.28	**3.57**
308	3.39	3.48	4.6	3.8	4.47	2.85	3.28	**3.21**
68	1.17	2.48	2.18	2.85	3.27	0.33	0.77	**0.05**
310	1.19	2.51	0.92	2.71	3.104	0.33	0.77	**0**
72	0.81	2.35	0.82	2.82	3.21	0.33	0.77	**0**
312	0.82	1.94	0.78	2.53	2.86	0.33	0.77	**0.24**
76	3.69	3.75	4.24	4.05	4.77	2.78	3.03	**2.51**
80	3.49	3.72	3.5	4	4.71	2.78	3.03	**1.23**
403	3.44	3.61	3.95	3.87	4.55	2.78	3.03	**3.38**
404	3.59	3.67	4.27	3.88	4.55	2.78	3.03	**3.66**
405	4.1	3.84	5.48	4.03	4.75	2.85	3.28	**4.53**
406	3.9	3.72	5.4	3.91	4.59	2.85	3.28	**3.03**
84	4.5	4.09	6.4	4.13	4.88	2.85	3.28	**3.52**
88	4.28	3.491	6.09	4.03	4.74	2.85	3.28	**4.27**
409	1.87	2.65	2.49	3.08	3.55	0.33	0.77	**0.41**
410	1.04	2.21	0.78	2.8	3.22	0.33	0.77	**0**
92	0.55	2.28	0.18	2.6	2.95	0.33	0.77	**0.37**
96	0.27	2.11	0.21	2.86	3.27	0.33	0.77	**0**
Full	**3.87**	**3.78**	**5.05**	**4.02**	**4.75**	**2.85**	**3.28**	**3.70**
Limited	**3.74**	**3.79**	**4.60**	**4.03**	**4.73**	**2.78**	**3.03**	**3.21**
Drought	**1.18**	**2.37**	**0.97**	**2.84**	**3.35**	**0.33**	**0.77**	**0.12**
MBE	0.58	0.96	1.20	1.28	1.92	-0.36	0.01	
RMSE	0.93	1.47	1.49	1.74	2.23	0.82	0.75	
T-Test	0.00	0.00	0.00	0.00	0.00	0.24	0.97	

4.6.3. Soil Water Deficit

Table A.4.14. Summary of the RS overpass soil water deficit statistics for the ARDED field 1070 summer 2015 RS campaign.

ARDEC 1070 RS Overpass Soil Water Deficit Summary				
	Date	**MBE (mm)**	**RMSE (mm)**	**T-Test**
Hybrid	30-Jul-15	6.32	19.74	0.03
	13-Aug-15	-9.92	21.94	0.00
	10-Sep-15	-3.76	18.78	0.25
Rz=1 m FAO-56	30-Jul-15	-29.55	59.09	0.00
	31-Jul-15	-14.16	23.83	0.00
	1-Aug-15	-25.16	31.90	0.00
Rz= 1.5 m FAO-56	30-Jul-15	46.69	53.16	0.00
	13-Aug-15	39.50	48.20	0.00
	10-Sep-15	46.57	54.94	0.00

Table A.4.15. Summary of the RS Campaign soil water deficit statistics for the ARDED field 1070 summer 2015 RS campaign.

ARDEC 1070 RS Campaign Soil Water Deficit Summary				
	MBE (mm/m)	**RMSE (mm/m)**	**T-Test**	
Hybrid	-2.45	20.20	0.24	Campaign
Rz=1 m FAO-56	-22.96	33.59	0.00	Campaign
Rz= 1.5 m FAO-56	29.68	42.60	0.00	Campaign

Table A.4.16. Mean SWD derived from the 2015 Tempest UAS RS campaign of the Full (F), Limited (L) and Drought (D) Irrigation Treatments.

2015 Mean Tempest UAS Mean SWD (mm m^{-1})									
	Hybrid			FAO-56			NP		
	F	L	D	F	L	D	F	L	D
30-JUL	167.3	188.38	178.90	147.15	164.44	159.43	159.77	180.15	175.82
13-AUG	152.32	163.93	194.88	154.86	161.08	182.26	165.83	185.11	188.88
10-SEP	184.11	185.51	194.88	153.96	154.89	190.07	179.82	187.79	206.31

Table A.4.17. Linear Regression Summary of the statistics from the SWD derived from the 2015 Tempest UAS RS campaign.

2015 Tempest UAS ET_d Linear Regression Coefficients			
	Hybrid	FAO-56 (R_z=1 m)	FAO-56 (R_z=1.5m)
a	0.46	0.29	0.41
b	87.20	106.35	117.59
R^2	0.25	0.04	0.31

Table A.4.18. Overpass SWD for the ARDED field 1070 summer 2015 RS campaign (100 and 200 Plots).

			🟩				🟨				🟥			
		NP Location	**101**	**102**	**103**	**104**	**105**	**106**	**107**	**108**	**109**	**110**	**111**	**112**
mm/m	NP-Deficit (mm)	30-Jul-15	138.22	135.43	N/A	140.08	176.79	164.69	172.61	180.97	179.95	181.89	184.61	182.35
	FAO56 SWB (mm)		147.15	147.15	N/A	147.15	164.44	164.44	164.44	164.44	165.92	165.92	165.92	165.92
	Hybrid Deficit (mm)		167.11	166.09	N/A	182.14	189.61	192.20	182.66	190.77	176.21	182.92	180.13	181.28
	NP-Deficit (mm)	13-Aug-15	146.20	140.62	N/A	142.19	186.76	171.36	176.23	190.60	192.33	197.22	200.77	198.89
	FAO56 SWB (mm)		154.86	154.86	N/A	154.86	161.08	161.08	161.08	161.08	182.26	182.26	182.26	182.26
	Hybrid Deficit (mm)		141.25	132.49	N/A	133.93	168.35	164.06	162.21	162.06	194.88	194.88	194.88	194.88
	NP-Deficit (mm)	10-Sep-15	158.70	153.17	N/A	154.24	191.69	176.56	173.89	186.30	209.72	212.24	217.00	219.52
	FAO56 SWB (mm)		153.96	153.96	N/A	153.96	154.89	154.89	154.89	154.89	190.07	190.07	190.07	190.07
	Hybrid Deficit (mm)		184.50	180.54	N/A	181.37	190.20	186.91	187.60	187.29	194.88	194.88	194.88	194.88
1.5 m	NP-Deficit (mm)	30-Jul-15	207.33	203.15	N/A	210.12	265.19	247.04	258.92	271.45	269.92	272.83	276.92	273.52
	FAO56 SWB (mm)		189.69	189.69	N/A	189.69	222.59	222.59	222.59	222.59	221.10	221.10	221.10	221.10
	Hybrid Deficit (mm)		250.67	249.14	N/A	273.21	284.41	288.30	273.98	286.15	264.31	274.38	270.20	271.92
	NP-Deficit (mm)	13-Aug-15	219.30	210.94	N/A	213.28	280.14	257.04	264.35	285.90	288.50	295.82	301.16	298.33
	FAO56 SWB (mm)		210.15	210.15	N/A	210.15	228.35	228.35	228.35	228.35	253.45	253.45	253.45	253.45
	Hybrid Deficit (mm)		211.87	198.74	N/A	200.90	252.52	246.09	243.32	243.09	292.32	292.32	292.32	292.32
	NP-Deficit (mm)	10-Sep-15	238.05	229.75	N/A	231.37	287.53	264.84	260.84	279.45	314.57	318.36	325.50	329.27
	FAO56 SWB (mm)		220.11	220.11	N/A	220.11	225.61	225.61	225.61	225.61	275.89	275.89	275.89	275.89
	Hybrid Deficit (mm)		276.75	270.81	N/A	272.06	285.30	280.37	281.40	280.94	292.31	292.31	292.31	292.31
		NP Location	**201**	**202**	**203**	**204**	**205**	**206**	**207**	**208**	**209**	**210**	**211**	**212**
mm/m	NP-Deficit (mm)	30-Jul-15	128.03	137.38	N/A	154.31	175.11	180.35	181.53	182.36	N/A	177.63	197.83	208.58
	FAO56 SWB (mm)		147.15	147.15	N/A	147.15	164.44	164.44	164.44	164.44	N/A	133.48	133.48	133.48
	Hybrid Deficit (mm)		174.40	173.24	N/A	182.09	197.57	195.32	192.15	203.70	N/A	189.03	180.21	185.26
	NP-Deficit (mm)	13-Aug-15	128.02	143.80	N/A	156.94	182.42	184.44	182.39	192.14	N/A	186.63	209.36	220.12
	FAO56 SWB (mm)		154.86	154.86	N/A	154.86	161.08	161.08	161.08	161.08	N/A	182.26	182.26	182.26
	Hybrid Deficit (mm)		153.46	146.10	N/A	152.00	162.32	162.85	162.21	166.42	N/A	194.88	194.88	194.88
	NP-Deficit (mm)	10-Sep-15	142.45	158.71	N/A	168.06	168.70	193.14	193.47	199.75	N/A	209.50	226.36	232.18
	FAO56 SWB (mm)		153.96	153.96	N/A	153.96	154.89	154.89	154.89	154.89	N/A	190.07	190.07	190.07
	Hybrid Deficit (mm)		177.43	186.40	N/A	177.92	184.31	182.18	182.76	183.57	N/A	194.88	194.88	194.88
1.5 m	NP-Deficit (mm)	30-Jul-15	192.05	206.08	N/A	231.46	262.66	270.52	272.29	273.55	N/A	266.44	296.75	312.87
	FAO56 SWB (mm)		189.69	189.69	N/A	189.69	222.59	222.59	222.59	222.59	N/A	221.10	221.10	221.10
	Hybrid Deficit (mm)		261.59	259.86	N/A	273.13	296.35	292.98	288.23	305.54	N/A	283.54	270.32	277.89
	NP-Deficit (mm)	13-Aug-15	192.04	215.70	N/A	235.40	273.62	276.66	273.59	288.22	N/A	279.95	314.05	330.18
	FAO56 SWB (mm)		210.15	210.15	N/A	210.15	228.35	228.35	228.35	228.35	N/A	253.45	253.45	253.45
	Hybrid Deficit (mm)		230.19	219.14	N/A	228.00	243.47	244.28	243.32	249.64	N/A	292.32	292.32	292.32
	NP-Deficit (mm)	10-Sep-15	213.68	238.07	N/A	252.09	253.06	289.71	290.21	299.62	N/A	314.25	339.54	348.27
	FAO56 SWB (mm)		220.11	220.11	N/A	220.11	225.61	225.61	225.61	225.61	N/A	275.89	275.89	275.89
	Hybrid Deficit (mm)		266.15	279.60	N/A	266.88	276.47	273.27	274.14	275.36	N/A	292.31	292.31	292.31

Table A.4.19. Overpass SWD for the ARDED field 1070 summer 2015 RS campaign (300 and 400 Plots).

			🟧				🟩				🟥			
		NP Location	**301**	**302**	**303**	**304**	**305**	**306**	**307**	**308**	**309**	**310**	**311**	**312**
mm/m	NP-Deficit (mm)	30-Jul-15	178.57	184.44	175.90	180.96	181.10	172.97	181.85	172.54	189.00	176.03	184.91	192.59
	FAO56 SWB (mm)		0.43	0.43	0.43	0.43	147.15	147.15	147.15	147.15	165.92	165.92	165.92	165.92
	Hybrid Deficit (mm)		188.50	187.47	187.77	187.81	161.09	165.00	159.95	159.38	179.76	187.37	177.60	179.59
	NP-Deficit (mm)	13-Aug-15	180.55	188.78	182.47	182.94	170.40	179.50	191.59	180.29	200.99	188.57	197.32	204.55
	FAO56 SWB (mm)		161.08	161.08	161.08	161.08	154.86	154.86	154.86	154.86	182.26	182.26	182.26	182.26
	Hybrid Deficit (mm)		170.09	164.07	162.07	165.97	162.20	152.60	165.40	167.38	194.88	194.88	194.88	194.88
	NP-Deficit (mm)	10-Sep-15	187.28	190.45	189.87	182.58	207.82	187.55	208.51	189.78	220.41	202.99	214.95	217.71
	FAO56 SWB (mm)		154.89	154.89	154.89	154.89	153.96	153.96	153.96	153.96	190.07	190.07	190.07	190.07
	Hybrid Deficit (mm)		189.36	185.61	185.72	187.09	186.11	186.40	178.16	180.14	194.88	194.88	194.88	194.88
1.5 m	NP-Deficit (mm)	30-Jul-15	267.86	276.65	263.85	271.45	271.66	259.45	272.78	258.81	283.50	264.05	277.37	288.88
	FAO56 SWB (mm)		222.59	222.59	222.59	222.59	189.69	189.69	189.69	189.69	221.10	221.10	221.10	221.10
	Hybrid Deficit (mm)		282.75	281.21	281.66	281.72	241.64	247.49	239.93	239.07	269.64	281.06	266.39	269.39
	NP-Deficit (mm)	13-Aug-15	270.83	283.17	273.71	274.40	255.60	269.25	287.38	270.43	301.48	282.86	295.97	306.82
	FAO56 SWB (mm)		228.35	228.35	228.35	228.35	210.15	210.15	210.15	210.15	253.45	253.45	253.45	253.45
	Hybrid Deficit (mm)		255.14	246.11	243.11	248.96	243.30	228.90	248.10	251.07	292.31	292.31	292.31	292.31
	NP-Deficit (mm)	10-Sep-15	280.91	285.67	284.81	273.86	311.73	281.33	312.76	284.66	330.61	304.49	322.42	326.57
	FAO56 SWB (mm)		225.61	225.61	225.61	225.61	220.11	220.11	220.11	220.11	275.89	275.89	275.89	275.89
	Hybrid Deficit (mm)		284.04	278.42	278.58	280.64	279.17	279.60	267.24	270.21	292.31	292.31	292.31	292.31
			401	**402**	**403**	**404**	**405**	**406**	**407**	**408**	**409**	**410**	**411**	**412**
mm/m	NP-Deficit (mm)	30-Jul-15	174.10	187.45	187.72	198.81	179.86	174.82	173.06	167.09	157.78	152.72	149.72	121.65
	FAO56 SWB (mm)		164.44	164.44	164.44	164.44	147.15	147.15	147.15	147.15	165.92	165.92	165.92	165.92
	Hybrid Deficit (mm)		180.66	182.27	177.81	177.82	165.36	164.36	161.44	161.44	169.42	173.47	170.67	170.66
	NP-Deficit (mm)	13-Aug-15	181.54	193.07	192.49	193.60	193.17	183.55	182.93	182.40	175.62	169.80	162.52	128.49
	FAO56 SWB (mm)		161.08	161.08	161.08	161.08	154.86	154.86	154.86	154.86	182.26	182.26	182.26	182.26
	Hybrid Deficit (mm)		159.62	162.42	163.22	165.00	156.03	152.70	153.48	163.52	194.88	194.88	194.88	194.88
	NP-Deficit (mm)	10-Sep-15	179.29	187.16	197.03	207.53	206.73	194.59	192.40	194.77	197.09	189.25	182.91	142.78
	FAO56 SWB (mm)		154.89	154.89	154.89	154.89	153.96	153.96	153.96	153.96	190.07	190.07	190.07	190.07
	Hybrid Deficit (mm)		180.09	184.18	184.82	186.50	190.85	191.24	190.05	186.48	194.88	194.88	194.88	194.88
1.5 m	NP-Deficit (mm)	30-Jul-15	261.15	281.17	281.58	298.21	269.79	262.24	259.60	250.63	236.67	229.08	224.58	182.48
	FAO56 SWB (mm)		222.59	222.59	222.59	222.59	189.69	189.69	189.69	189.69	221.10	221.10	221.10	221.10
	Hybrid Deficit (mm)		270.98	273.40	266.72	266.72	248.04	246.54	242.16	242.16	254.12	260.21	256.00	255.99
	NP-Deficit (mm)	13-Aug-15	272.31	289.61	288.73	290.40	289.76	275.32	274.40	273.59	263.43	254.70	243.79	192.73
	FAO56 SWB (mm)		228.35	228.35	228.35	228.35	210.15	210.15	210.15	210.15	253.45	253.45	253.45	253.45
	Hybrid Deficit (mm)		239.43	243.63	244.83	247.50	234.05	229.05	230.22	245.28	292.31	292.31	292.31	292.31
	NP-Deficit (mm)	10-Sep-15	268.93	280.74	295.55	311.30	310.09	291.88	288.60	292.16	295.63	283.88	274.36	214.16
	FAO56 SWB (mm)		225.61	225.61	225.61	225.61	220.11	220.11	220.11	220.11	275.89	275.89	275.89	275.89
	Hybrid Deficit (mm)		270.14	276.27	277.23	279.75	286.28	286.86	285.08	279.72	292.31	292.31	292.31	292.31